

**NUMERICAL STUDIES ON THE EFFECT OF SWIRL
AND TRANSIENT TEMPERATURE DATA ON FLAT
SURFACE FILM COOLING**

Thesis

Submitted in partial fulfillment of the requirements for the
Degree of

DOCTOR OF PHILOSOPHY

by

VASHISTA G A



DEPARTMENT OF MECHANICAL ENGINEERING
NATIONAL INSTITUTE OF TECHNOLOGY KARNATAKA,
SURATHKAL, MANGALORE-575025

SEPTEMBER, 2023

**NUMERICAL STUDIES ON THE EFFECT OF
SWIRL AND TRANSIENT TEMPERATURE DATA ON
FLAT SURFACE FILM COOLING**

Thesis

Submitted in partial fulfillment of the requirements for the

Degree of

DOCTOR OF PHILOSOPHY

by

VASHISTA G A

(Reg. No.165042ME16F21)

Under the Guidance of

Dr. RAVIKIRAN KADOLI

Professor



DEPARTMENT MECHANICAL ENGINEERING
NATIONAL INSTITUTE OF TECHNOLOGY KARNATAKA,
SURATHKAL, MANGALORE -575025

SEPTEMBER, 2023

DECLARATION

I hereby declare that the Research Thesis entitled "**NUMERICAL STUDIES ON THE EFFECT OF SWIRL AND TRANSIENT TEMPERATURE DATA ON FLAT SURFACE FILM COOLING,**" which is being submitted to the **National Institute of Technology Karnataka, Surathkal** in partial fulfilment of the requirements for the award of the Degree of **Doctor of Philosophy in Mechanical Engineering** is a *bonafide report of the research work carried out by me*. The material contained in this Research Thesis has not been submitted to any other Universities or Institutes for the award of any degree.

Register Number: 165042

Name of the Research Scholar: **VASHISTA G A**

Signature of the Research Scholar:



Department of Mechanical Engineering


Place: NITK, Surathkal

Date: 11/09/2023

CERTIFICATE

This is to certify that the Research Thesis entitled “**NUMERICAL STUDIES ON THE EFFECT OF SWIRL AND TRANSIENT TEMPERATURE DATA ON FLAT SURFACE FILM COOLING**” submitted by **Mr. Vashista G A (Register Number: 165042)** as the record of the research work carried out by him, *is accepted as the Research Thesis submission* in partial fulfilment of the requirements for the award of the degree of **Doctor of Philosophy**.

Research Guide

 11-9-2023

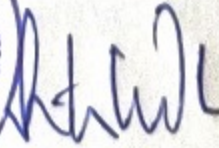
Dr. Ravikiran Kadoli

Professor

Department of Mechanical Engineering

NITK, Surathkal



 11-9-2023

Chairman-DRPC

Department of Mechanical Engineering

National Institute of Technology Karnataka, Surathkal

ACKNOWLEDGMENT

Firstly, I would like to express heartfelt gratitude to my supervisor **Professor Ravikiran Kadoli** for his immense support, acute guidance and encouragement throughout my research at NITK. His invaluable patience and continuous support held me upright during the time of difficulty and kept me going toward completing this work.

My thanks must also go to **Dr. Veershetty Gumtapure** and **Dr. Ramesh H** for serving on my graduate committee and for their valuable suggestions throughout my work. Additionally, I would like to thank the Department of Mechanical Engineering for providing the necessary facilities to carry out my research. I must remember to thank **Dr. Vijaykumar Hindasgeri**, who has been the foundational support for this work by giving keen technical insights from the inception. My special thanks to **Dr. Kumar G N**, **Dr. Anish S** and **Dr. Gnanashekharan N** for their valuable suggestions.

I also wish to thank wholeheartedly to my friends **Anil R Kadam**, **Shashikumar**, **Ritesh kumar Parida**, **Chetan Kumar**, **Mukund Patil**, **Subba Rao M**, **Rakesh Patil**, **Rudramurthy**, **Tabish Wahidi**, **Silambarasan**, **Om Kapoor**, **Manimaran**, **Ajinkya Budruk**, **Abhijeeth Boche**, **Hari Tej**, **Deepak Narayan**, **Kalinga Naik**, **Sathisha** and many more, without their extensive support and timely help this work would seem impossible.

I am extremely thankful to all the faculty members and non-teaching staff of the Department of Mechanical Engineering, NITK Surathkal, for their direct or indirect support during my time at NITK.

At last, sincere thanks to my parents, wife, sisters and family members for supporting me at every stage of my life, especially during the phase of hardships.

VASHISTA G A

ABSTRACT

Higher inlet temperatures to increase the efficiency of gas turbine engines require improved component cooling. In this regard, the shape of the film cooling hole proved to impact the cooling performance considerably. Plenty of research are being carried out to develop a novel film cooling hole concept. In film cooling flows, the counter-rotating vortex pair (CRVP) is of paramount significance due to its inherited characteristics in lifting the coolant away from the wall. Most of the advanced hole design concepts are aimed at weakening the strength of this vortex, there by reducing jet penetration and enhancing film cooling effectiveness.

The present thesis is intended to study the film cooling behavior in the presence of a twisted tape insert inside a film hole through computational fluid dynamics simulations. The twisted tape insert imparts a swirl to the coolant flow. The presence of serpentine passage channels and impingement angles are the sources of swirl generators on the coolant flow during internal cooling. The twisted tape insert can further be used to control such swirls systematically. This method allows controlling the coolant swirl intensity by varying the pitch of the twisted tape.

The present study investigates swirl numbers of 0.0289, 0.116 and 0.168 at the beginning. Area-averaged effectiveness and heat transfer coefficient are evaluated as the measure of performance parameters for blowing ratios of 0.5, 1.0, 1.5 and 2.0. Results revealed a significant improvement in the effectiveness in the presence of swirl. Coolant swirl predominantly modifies the jet trajectory resulting in a reduced jet penetration and increased lateral expansion. Further investigation on the effect of twisted tape thickness on the coolant distribution is found to be negligible. But inserting a twisted tape created higher pressure losses across the hole with a nearly 11% reduction in discharge coefficient, indicating additional pumping power requirements.

Further, the study is extended to higher swirl numbers of 0.2, 0.4, 0.6 and 0.7. For blowing ratios less than 1.0, peak effectiveness occurred at a swirl number of around 0.4, enhancing effectiveness up to 180%. While at higher blowing ratios, the effectiveness peaks at higher swirl numbers. The spatially averaged effectiveness for

the case of blowing ratio 2.0 and swirl number 0.6 has increased by almost 2500%. The case with swirl number of 0.7 resulted in high cooling efficiency in the immediate downstream of injection at high blowing ratios while completely ignoring the far downstream region. Mean while, the average net heat flux reduction due to swirl is achieved as high as 500% when blowing ratio and swirl numbers are at 1.5 and 0.6, respectively. The swirl effect on CRVP is apparent at high swirl numbers creating a highly asymmetrical structure. On the other hand, heat transfer coefficients are seen barely affected by the presence of swirl.

A parametric study by varying injection angle and hole length at a particular swirl number and blowing ratio revealed enhancement in the effectiveness with the angle, a contrary feature to the absence of swirl. However, the hole length effect was moderate on the swirled film cooling behavior. It also attempted to obtain an optimized geometrical combination of swirl number, injection angle and hole length, employing a Radial Basis Function Neural Network as a surrogate model and Genetic algorithm as an optimizing tool. At a blowing ratio of 1.0, the optimized parameters of geometry were obtained as a swirl number of 0.32, injection angle of 19.3° and hole length to diameter ratio of 4.

In the last part of this thesis, an inverse heat conduction based data reduction technique is proposed for the simultaneous estimation of film cooling effectiveness and heat transfer coefficient from transient temperature measurements. This method employs an optimization technique known as the Levenberg-Marquardt Algorithm to estimate the unknown thermal boundary parameters of film cooling. The objective function for the inverse algorithm is constructed using the analytical solution of a transient one-dimensional semi-infinite body. The transient surface temperature data required for the analysis is obtained through a conjugate numerical simulation. Laterally averaged effectiveness and heat transfer coefficient for blowing ratios of 0.5, 0.8, and 1.0 are analyzed using the present technique and compared against the steady-state simulation results to demonstrate the methodology. An average deviation of around 7% for the estimated effectiveness and 4% for the heat transfer coefficient values are observed. This method avoids the existing two-test strategy and yields unknown parameters with short duration measurements.

Keywords: *Swirled film cooling, Effectiveness, Net heat flux reduction, Counter-rotating vortex pair, Radial basis function neural network, Genetic algorithm, Levenberg-Marquardt algorithm.*

TABLE OF CONTENTS

ABSTRACT.....	i
TABLE OF CONTENTS.....	v
LIST OF FIGURES	ix
LIST OF TABLES.....	xv
NOMENCLATURE	xvii
1 INTRODUCTION	1
1.1 INTRODUCTION	1
1.1.1 Necessity of cooling.....	3
1.1.2 Types of turbine blade cooling	5
1.2 Film cooling.....	7
1.2.1 Flat-plate film cooling.....	10
1.3 MOTIVATION BEHIND THE STUDY.....	10
1.4 OVERVIEW OF THE RESEARCH	11
1.5 OUTLINE OF THE THESIS.....	12
2 LITERATURE REVIEW	15
2.1 INFLUENCE OF FLOW PARAMETERS	15
2.1.1 Blowing ratio	15
2.1.2 Density ratio (DR).....	17
2.1.3 Mainstream turbulence.....	19
2.2 INFLUENCE OF GEOMETRIC PARAMETERS	19
2.2.1 Hole length to diameter ratio	19
2.2.2 Pitch-to-diameter ratio	20
2.2.3 Injection angle.....	21

2.2.4 Surface roughness	22
2.2.5 Curvature.....	22
2.2.6 Effect of cooling hole geometry	23
2.3 FILM COOLING FLOW FEATURES	23
2.4 COMPUTATIONAL STUDIES ON FILM COOLING	25
2.5 FILM COOLING HOLE SHAPES	27
2.5.1 Swirled film cooling	32
2.6 OPTIMIZATION OF FILM COOLING HOLE GEOMETRY	37
2.7 TRANSIENT STUDIES ON FILM COOLING.....	39
2.8 SUMMARY OF THE LITERATURE SURVEY AND RESEARCH GAPS	43
2.9 OBJECTIVES OF THE PRESENT WORK.....	44
2.10 CLOSURE	45
3 NUMERICAL MODELING	47
3.1 GEOMETRY OF THE COMPUTATIONAL DOMAIN.....	47
3.2 NUMERICAL MESH.....	50
3.3 GOVERNING EQUATIONS	51
3.3.1 The SST $k - \omega$ turbulence model	52
3.4 BOUNDARY CONDITIONS	54
3.4.1 Numerical set-up.....	55
3.5 GRID INDEPENDENCE STUDY	55
3.6 EVALUATION OF TURBULENCE MODELS	56
3.7 VALIDATION.....	58
3.8 CLOSURE	59
4 EFFECT OF COOLANT SWIRL ON FILM COOLING BEHAVIOR	61
4.1 INTRODUCTION	61

4.2 EFFECTIVENESS.....	61
4.3 FLOW STRUCTURE.....	64
4.4 JET TRAJECTORY.....	67
4.5 EFFECT OF TWISTED TAPE THICKNESS	68
4.6 COEFFICIENT OF DISCHARGE	69
4.7 TWISTED TAPE ALIGNMENT INSIDE THE FILM HOLE	70
4.8 HEAT TRANSFER COEFFICIENT RATIO (h/h_0)	74
4.9 NET HEAT FLUX REDUCTION.....	76
4.10 EFFECT OF SWIRL NUMBER – COOLANT HAVING HIGH SWIRL INTENSITY	78
4.10.1 Effectiveness	78
4.10.2 Heat transfer coefficient.....	80
4.10.3 Net heat flux reduction ratio	81
4.10.4 Area averaged parameters.....	81
4.10.5 Flow features.....	82
4.11 EFFECT OF INJECTION ANGLE.....	91
4.12 EFFECT OF HOLE LENGTH-TO-DIAMETER RATIO	94
4.13 CLOSURE	97
5 OPTIMIZATION OF GEOMETRICAL PARAMETERS IN SWIRLED FILM COOLING	99
5.1 INTRODUCTION	99
5.2 LATIN HYPERCUBE SAMPLING	100
5.3 RADIAL BASIS FUNCTION NEURAL NETWORK.....	101
5.4 GENETIC ALGORITHM	103
5.5 RESULTS AND DISCUSSION	105
5.6 CLOSURE	110

6 SIMULTANEOUS ESTIMATION OF REFERENCE TEMPERATURE AND HEAT TRANSFER COEFFICIENT IN TRANSIENT FILM COOLING	113
6.1 INTRODUCTION	113
6.2 ONE-DIMENSIONAL SEMI-INFINITE ANALYSIS.....	114
6.3 LEVENBERG-MARQUARDT ALGORITHM.....	116
6.4 EVALUATION OF TRANSIENT TEMPERATURE DATA	119
6.5 RESULTS FROM THE TRANSIENT ANALYSIS	123
6.5.1 Validation of the numerical setup and the present IHCP method.	123
6.5.2 Linear fit method.....	125
6.5.3 Effectiveness	126
6.5.4 Sensitivity analysis.....	127
6.5.5 Heat transfer coefficient.....	130
6.6 CLOSURE	133
7 SUMMARY AND CONCLUSIONS	135
7.1 Contribution of the present work	137
7.2 Scope for future work	138
REFERENCES	139

LIST OF FIGURES

Figure 1.1. Cross-sectional view of GT13E2 gas turbine with 202.7 MW power output capacity (Schobeiri 2017).	2
Figure 1.2. Schematic of an operating cycle of a gas turbine.	2
Figure 1.3. P-V and T-S diagrams of an ideal Brayton cycle.	3
Figure 1.4. Relation between turbine inlet temperature, pressure ratio and thermal efficiency (Schobeiri 2017).	4
Figure 1.5. Development of turbine cooling concepts over the years allowing to achieve higher TIT (Han et al. 2012).	5
Figure 1.6. Cooling mechanisms used in gas turbine components (Lakshminarayana 1995).	6
Figure 1.7. Internal and external cooling mechanisms applied to a turbine blade (Han et al. 1984).	6
Figure 1.8. Film cooling arrangement over a turbine blade (a) Cross-sectional view (b) Three-dimensional view (c) Film cooling mechanism exaggerated over a single hole (Han et al. 2012).	7
Figure 2.1. Effect of blowing ratio on effectiveness (Goldstein et al. 1968a). 16	16
Figure 2.2. Variation of h with M (Hay et al. 1985).	17
Figure 2.3. Effect of density ratio on coolant distribution (Pietrzyk et al. 1989a).	18
Figure 2.4. variation of η at different density ratios (Sinha et al. 1991).	18
Figure 2.5. Lateral coolant distribution of coolant at different downstream locations (Goldstein et al. 1974).	20
Figure 2.6. Flow visualization of normal and inclined jets at a velocity ratio of 0.5 (Lee et al. 1994).	21
Figure 2.7. Effect of curvature on film cooling effectiveness (Schwarz et al. 1991).	22
Figure 2.8 Vortical structures generated from a normal jet-cross flow interaction (Fric and Roshko 1994).	24
Figure 2.9. Predicted temperature vs. measurement (Demuren et al. 1985).	25

Figure 2.10. Velocity vectors inside a film hole (Leylek and Zerkle 1993).	26
Figure 2.11. Film cooling hole geometries studied by Thole et al. (1996).	28
Figure 2.12. Geometrical profile of the variants of (a) Fan-shaped, (b) Laidback and (c) Laidback fan-shaped holes (Saumweber and Schulz 2012).	29
Figure 2.13 Coolant injection into a transverse trench (Bunker 2002).	29
Figure 2.14. Concept of antivortex hole shape (Dhungel et al. 2009).	30
Figure 2.15 Converging slot type of film cooling hole design (Sargison et al. 2002).	30
Figure 2.16. Recently investigated hole geometry configurations.	31
Figure 2.17. Few advanced concepts of film cooling hole designs.	32
Figure 2.18. Reduction in jet penetration height with swirl number as observed by Terzis et al. (2011).	34
Figure 2.19. Mechanism of swirl generation used in the study of Takeishi et al. (2010).	35
Figure 2.20. Swirl generation by modifying coolant entry into the film hole from the plenum chamber (Jiang et al. 2017).	36
Figure 3.1. Three-dimensional view of the computational domain used for the numerical simulation.	47
Figure 3.2. Geometrical aspects of a twisted tape insert inside a cylinder.	48
Figure 3.3. Computational mesh highlighting the film hole region with twisted tape insert.	51
Figure 3.4. Verification of grid independent solution for the numerical simulations.	56
Figure 3.5. Performance evaluation of turbulence models.	57
Figure 3.6. Comparison of the present numerical results with the experiments for (a) $M = 0.5$ and (b) $M = 1.0$.	59
Figure 4.1. Laterally averaged effectiveness for different blowing ratios and swirl numbers along the downstream direction of film hole.	62
Figure 4.2. Lateral effectiveness distribution at downstream locations of the film hole.	63
Figure 4.3. Streamlines on $x - y$ plane at $z/d = 0$ with y -velocity contour.	65

Figure 4.4. Streamlines on $x - z$ plane at $y/d = 0.05$ with z -velocity contour.	65
Figure 4.5. Three-dimensional iso-contours of temperature along with streamlines on $y - z$ plane at $xd = 2, 5$ and 10	66
Figure 4.6. Comparison of observed jet trajectory for different swirl numbers.	67
Figure 4.7. Twisted tape thickness effect on the laterally averaged effectiveness.....	68
Figure 4.8. Discharge coefficient for the case of with and without twisted tape insert.....	69
Figure 4.9. Arrangement of twisted tapes (a) In-line twist (b) 90° twist.....	70
Figure 4.10. Comparison of laterally averaged effectiveness for twisted tape insert being in-line and 90° out of phase with respect to mainstream for different M and S	72
Figure 4.11. Comparison of y and z velocity at the exit of film hole for twist insert being in-line and 90° out of phase cases.	73
Figure 4.12. Comparison of coolant distribution using temperature contour and streamlines for $M = 1.0$ and $S = 0.168$	74
Figure 4.13. Heat transfer coefficient in downstream of the film hole for different swirl numbers and blowing ratios.	75
Figure 4.14. Reduction of the laterally averaged net heat flux in downstream of the film hole for different swirl numbers and blowing ratios.....	76
Figure 4.15. Area averaged film cooling (a) effectiveness (b) heat transfer coefficient for different swirl numbers and blowing ratios.	77
Figure 4.16. Laterally averaged effectiveness with respect to different swirl numbers at (a) $M = 0.5$, (b) $M = 1.0$, (c) $M = 1.5$, and (d) $M = 2.0$	79
Figure 4.17. Heat transfer coefficient in the downstream of film hole.....	80
Figure 4.18. Reduction of the laterally averaged net heat flux in the downstream of film hole for high swirl numbers and blowing ratios.....	81
Figure 4.19. Area average quantities of effectiveness, heat transfer coefficient and NHFR for high swirl cases.....	82

Figure 4.20. Contours showing the distribution of η on different planes along with the streamlines representing the flow pattern for $S = 0, M = 1.0$	85
Figure 4.21. Contours showing the distribution of η on different planes along with the streamlines representing the flow pattern for $S = 0.4, M = 1.0$	86
Figure 4.22. Contours showing the distribution of η on different planes along with the streamlines representing the flow pattern for $S = 0.7, M = 1.0$	87
Figure 4.23. Contours showing the distribution of η on different planes along with the streamlines representing the flow pattern for $S = 0, M = 2.0$	88
Figure 4.24. Contours showing the distribution of η on different planes along with the streamlines representing the flow pattern for $S = 0.4, M = 2.0$	89
Figure 4.25. Contours showing the distribution of η on different planes along with the streamline representing the flow pattern for $S = 0.7, M = 2.0$	90
Figure 4.26. Effect of injection angle on laterally averaged effectiveness.....	91
Figure 4.27. Effect of injection angle on laterally averaged heat transfer coefficient.	91
Figure 4.28. Effect of injection angle on laterally averaged net heat flux reduction.	92
Figure 4.29. Comparison of area average quantities of (a) Effectiveness, (b) Heat transfer coefficient and (c) Net heat flux reduction for different injection angles.	92
Figure 4.30. Effect of L/d on laterally averaged effectiveness.	95
Figure 4.31. Effect of L/d on laterally averaged heat transfer coefficient.	95
Figure 4.32. Effect of L/d on laterally averaged net heat flux reduction.....	96
Figure 4.33. Comparison of area average quantities of (a) Effectiveness, (b) Heat transfer coefficient and (c) Net heat flux reduction for different L/d ratios.....	96
Figure 5.1. Sampling points distributed in latin hypercube space for training and testing the RBF neural network.....	101
Figure 5.2. A typical structure RBFNN consists of three input variables and a single output vector.....	102
Figure 5.3. Training and testing accuracies of RBFNN model of the present study.....	103

Figure 5.4. Procedure for optimization using GA tool in matlab.	105
Figure 5.5. Distributions of the objective function within the design space of film cooling parameters used for optimization.	106
Figure 5.6. Comparison of laterally averaged effectiveness for the base case, reference geometry and optimized geometry.....	107
Figure 5.7. Lateral distribution of effectiveness on the plane at $yd = 0$ (a) reference and (b) optimized geometry.	108
Figure 5.8. Effectiveness on the center plane (at $zd = 0$) for (a) reference and (b) optimized geometry.....	108
Figure 5.9 Coolant streamlines and velocity vectors along with temperature contour on $y - z$ plane at $xd = 5$	110
Figure 6.1. One-dimensional heat transfer across a film cooled semi-infinite flat plate.	114
Figure 6.2. Flow chart of the present inverse algorithm for the estimation of film cooling parameters.	118
Figure 6.3. 3D Computational domain highlighting the solid-fluid interface to obtain transient surface temperature data using conjugate heat transfer solution.	119
Figure 6.4. A 2D representation of the computational domain used for transient analysis film cooling over a flat surface. (a) Front sectional view at $z/d = 0$, (b) Top view, and (c) Side view.....	119
Figure 6.5. Effect of mesh refinements on computed effectiveness by numerical simulation for $M = 0.5$	121
Figure 6.6. Validation of the present numerical results with the literature....	123
Figure 6.7. (a) Transient temperature data generated from the forward solution with additional random noise of $\pm 1K$, comparison of estimated parameters using noisy data, (b) effectiveness, (c) heat transfer coefficient.	124
Figure 6.8. Linearity between wall temperature and heat flux.	125
Figure 6.9. Comparison of laterally averaged effectiveness obtained using different techniques for (a) $M = 0.5$, (b) $M = 0.8$ and (c) $M = 1.0$	127
Figure 6.10. Sensitivity coefficients for T_{ref} and h with time at $x/d = 10$ for $M = 1.0$	128

Figure 6.11. Determinant of sensitivity coefficients with time at $x/d = 10$ for $M = 1.0$	129
Figure 6.12. Three-dimensional distribution of objective function.	130
Figure 6.13. Heat transfer coefficient for a flat surface with no coolant injection.....	131
Figure 6.14. Comparison of normalized laterally averaged heat transfer coefficient obtained using different techniques for (a) $M = 0.5$, (b) $M = 0.8$ and (c) $M = 1.0$	132

LIST OF TABLES

Table 3.1 Swirl numbers and corresponding pitch for the twisted tape insert during the initial study.	50
Table 3.2. Various geometrical parameters examined in the present study.....	50
Table 3.3. Film cooling parameters used in the present study.....	54
Table 5.1. Design variables and corresponding lower and upper limits used to evaluate the optimum design point.	100
Table 5.2. Comparison of η_s obtained from CFD and RBFNN model for reference and optimized geometries.	107
Table 6.1. Input conditions used in the present simulation.	120
Table 6.2. Coefficients of the curve fit equation for the variation of fluid properties with respect to temperature.	122

NOMENCLATURE

e	Bias value
b	Thickness of twisted tape insert, mm
C_d	Coefficient of discharge
d	Diameter of film cooling hole, mm
F_1, F_2	Blending functions
G_θ	Axial flux of angular momentum, Ns/m^2
G_x	Axial flux of axial momentum. Ns/m^2
g	Input variable
h	Heat transfer coefficient, $\text{W/m}^2\text{K}$
J	Jacobian
k	Turbulent kinetic energy, m^2/s^2
L	Length of the film hole, mm
l	Thickness of the plate, mm
M	Blowing ratio
\dot{m}_c	Actual mass flow rate through film hole, kg/s
Nu	Nusselt number
o	Output function of nequral network
P_f	Pitch of film cooling holes, mm
PR	Pressure ratio
Pr	Prandtl number
Pr_t	Turbulent Prandtl number
p	Parameter
p_t	Pitch of the twisted tape, mm
p_c	Pressure at the inlet of film hole, N/m^2
p_∞	Pressure at the exit of film hole, N/m^2
q''	Heat flux, W/m^2
R	Regression coefficient
Re	Reynolds number

r	Radial distance from the center of the film hole, mm
S	Swirl number
S	Modulus of mean strain rate
S_{ij}	Mean rate of strain tensor
T	Temperature, K
TR	Twist ratio
t	Time, s
U	Velocity, m/s
u'	Instantaneous velocity component
w	Width of the twisted tape, mm
w	Weights in the output layer of neural network
x, y, z	Coordinates
Y	Measured data
Z	Objective function

Greek symbols

α	Injection angle
γ	Specific heat ratio
δ	Thermal conductivity of solid, W/mK
δ_a	Thermal conductivity of air, W/mK
δ_{ij}	Kronecker delta
ε	Turbulence dissipation rate, m^2/s^3
ς	Variance of Gaussian distribution
η	Effectiveness
$\bar{\eta}$	Laterally averaged effectiveness
$\bar{\bar{\eta}}$	Area averaged effectiveness
η_s	Spatially averaged effectiveness
η_{th}	Thermal efficiency
θ'	Instantaneous temperature
κ	Iteration number
λ	Damping parameter

μ	Dynamic viscosity, Ns/m ²
μ_t	Eddy viscosity, Ns/m ²
π	Pressure ratio
ρ	Density, kg/m ³
σ	Thermal diffusivity of solid, m ² /s
σ_k	Turbulent Prandtl number for k
σ_ω	Turbulent Prandtl number for ω
τ_{ij}	Reynolds stress tensor
φ	Gaussian transfer function
ω	Turbulence specific dissipation rate, 1/s

Subscripts

c	Coolant
f	Film cooling
i	Initial
i, j, k	Unit vectors in x, y, z directions
m	Mainstream
ref	Reference temperature
s	Spatially averaged
w	Wall
0	Without film cooling

Abbreviations

ANN	Artificial neural network
CRVP	Counter-rotating vortex pair
GA	Genetic algorithm
HTC	Heat transfer coefficient
IHCP	Inverse heat conduction problem
LMA	Levenberg-Marquardt algorithm
LHS	Latin hypercube sampling

NHFR	Net heat flux reduction
RBNN	Radial basis function neural network
RANS	Reynolds averaged Navier-Stokes
TIT	Turbine inlet temperature

CHAPTER 1

INTRODUCTION

1.1 INTRODUCTION

Today the per capita energy consumption of the world is around 3200kWh, according to world bank International Energy Agency (IEA) statistics. It is expected that by 2040, the energy requirement in the aviation sector itself will reach around 19% of the total energy consumption. A gas turbine engine is the primary operating cycle for producing energy in the aviation sector. Not only in aviation industry, but gas turbines are one of the most reliable devices in ground based power plants for generating electricity.

A gas turbine is an internal combustion engine based on the Brayton cycle using ambient air as a primary working fluid. These engines are versatile due to their applicability in various power consuming operations. One of the largest power plants in Russia, which produce around 5600 MW had installed eight gas turbines with 800 MW capacity each. Gas turbines can also be used in smaller units of around 20-30 kW, such as auxiliary power units, jet engines, marine applications and locomotives. It has a high power-to-weight ratio compared to other types of internal combustion engines, such as SI and CI engines. Since there are fewer mechanical parts in a gas turbine, the operating cost is less and requires less maintenance. A major advantage of a gas turbine is its efficiency which can reach as high as about 60% when used in combined cycles.

A typical gas turbine engine is shown in Figure 1.1, highlighting the essential parts inside the engine. Majorly it consists of an inlet nozzle followed by a compressor section, a combustion chamber, a turbine section and a nozzle to exhaust the gases. The gas turbine operating cycle can be schematically represented as shown in Figure 1.2 and corresponding P-V and T-S diagrams are shown in Figure 1.3. In the operating cycle, the ambient air is sucked and supplied to a compressor, which is compressed to achieve the desired pressure ratio. This process occurs as an isentropic

compression utilizing a work of W_{12} in an ideal cycle. As the compressed air enters the combustion chamber, fuel is added to it, releasing the chemical potential of the fuel into thermal energy, which is a constant pressure heat addition (Q_{23}). This process leads to the generation of very high temperature combustion gas with high pressure, which is expanded through multiple stages of the turbine section. This process yields useful work output of W_{34} which is again an isentropic expansion. The hot gases are then released into the atmosphere by normalizing their pressure through a diffuser. The work input required by the compressor is driven from the shaft output and the remaining energy is utilized for the required power generation.

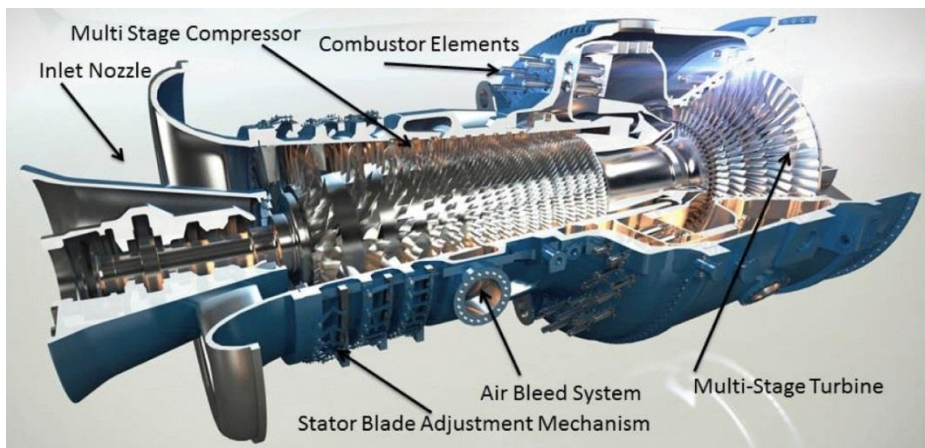


Figure 1.1. Cross-sectional view of GT13E2 gas turbine with 202.7 MW power output capacity (Schobeiri 2017).

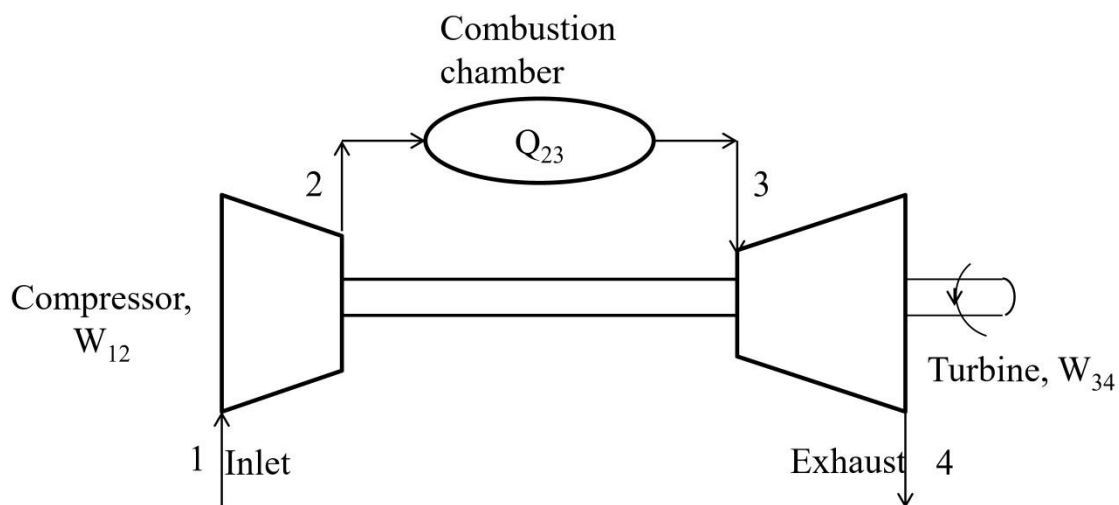


Figure 1.2. Schematic of an operating cycle of a gas turbine.

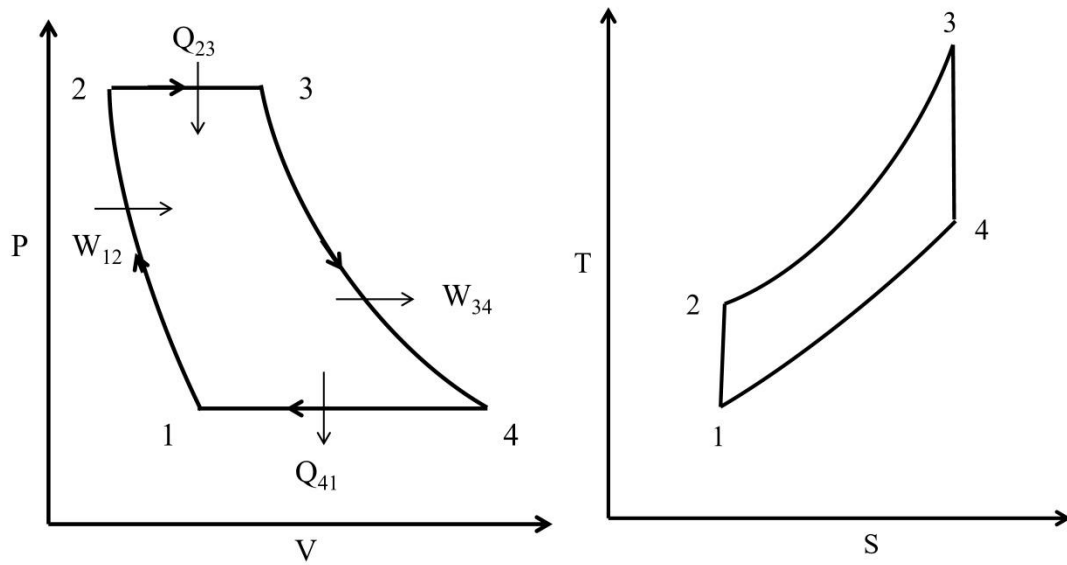


Figure 1.3. P-V and T-S diagrams of an ideal Brayton cycle.

1.1.1 Necessity of cooling

As the demand for gas turbine engines has increased, it is crucial to develop engines to consume less fuel due to the limited resources available. The engine's specific fuel consumption can be reduced by increasing its efficiency. The pressure ratio and the turbine inlet temperature (TIT) are the two significant parameters contributing to higher thermal efficiency. The thermal efficiency of an ideal Brayton cycle is calculated as,

$$\eta_{th} = 1 - \frac{1}{PR^{(\gamma-1)/\gamma}} \quad (1.1)$$

where PR is the pressure ratio and γ is the specific heat ratio. Hence increasing PR can lead to higher η_{th} . However, increasing PR beyond a certain value would start decreasing the efficiency. Figure 1.4 shows the relation between TIT and PR with the thermal efficiency. It can be seen that, at a particular TIT, the η_{th} will peak at a particular π and decreases beyond. If the TIT is increased, the gas turbine engine can operate at higher pressure ratios resulting in higher thermal efficiency.

Even though increasing TIT enhances efficiency, there are a few consequences that need to be rectified. As the components are constantly exposed to very high temperature gases, which might exceed the material limits and lead to the development of creep. When a component is exposed to high temperatures, the

material may permanently lose its inherited properties, such as material strength. The term creep refers to such permanent deformation of the engine components under thermal stress. When the engine operates for a prolonged time, the development of creep can lead to a complete breakdown of its components. Modern gas turbine engines operate at a TIT as high as about 1900K, especially the stator's nozzle vane and the rotor blades first few stages. This temperature is far above the permissible limit of the blade materials. For example, a Nickel based super alloy exhibits the development of melting at around 1204°C. These alloys are coated with zirconia or aluminum oxides known as thermal barrier coatings (TBC) as insulation against hot gasses. TBCs can only reduce the heat flux experienced by the blades to some extent. However, locations such as leading edges get exposed to severe thermal loadings.

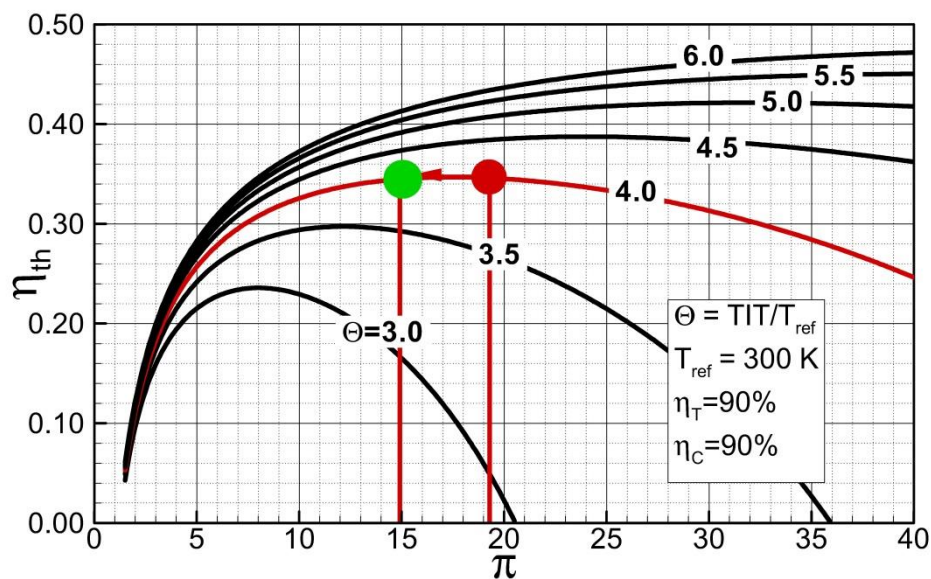


Figure 1.4. Relation between turbine inlet temperature, pressure ratio and thermal efficiency (Schobeiri 2017).

One obvious and most straightforward solution to attain high TIT while keeping the creep to its lowest is applying different cooling mechanisms locally over the components wherever the thermal stresses are high. Hence design and development of the turbine cooling process have emerged as a paramount objective for engineers.

1.1.2 Types of turbine blade cooling

As turbine cooling became inevitable, various cooling mechanisms were proposed. Most of these cooling techniques are based on air cooling since it is readily available when gas turbines operate above the ground. The air required for cooling is derived from the compressor output. Though extracting air from the compressor and supplying it to the engine would induce aerodynamic losses due to the mixing of coolant with hot gasses, the reduction in fuel consumption through an increase in TIT will be significant over the losses.

Figure 1.5 shows the improvements in TIT over the years with respect to different cooling mechanisms employed. In the early days, the uncooled blades allowed the turbines to operate up to 1200°C. The introduction of simple internal cooling enhanced the allowable range by another 300°C additionally. Figure 1.6 shows the types of cooling mechanisms applied inside gas turbine engine components. A simple internal cooling is achieved by circulating cold air through the serpentine passages made inside the blades, which removes the heat through convection. At a few critical locations, the air is made to impinge on inner surfaces, known as impingement cooling, to improve the heat removal rate. It can be seen from Figure 1.7 how the coolant air is passed inside a turbine blade through serpentine passages to maximize the rate of heat absorption.

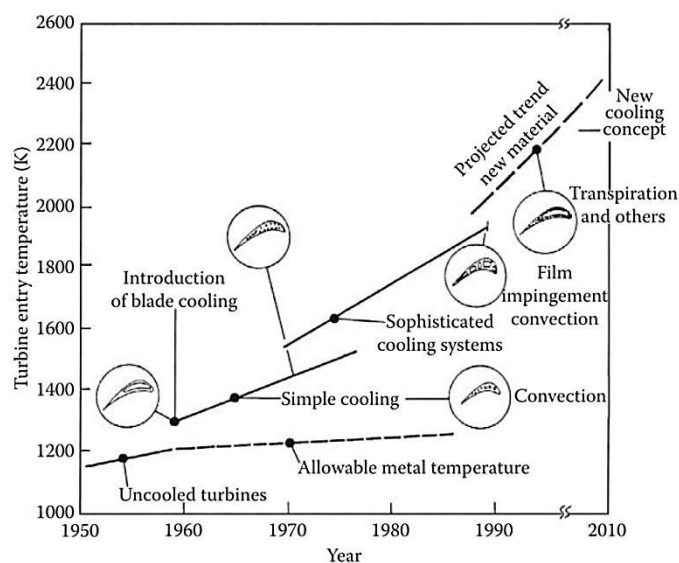


Figure 1.5. Development of turbine cooling concepts over the years allowing to achieve higher TIT (Han et al. 2012).

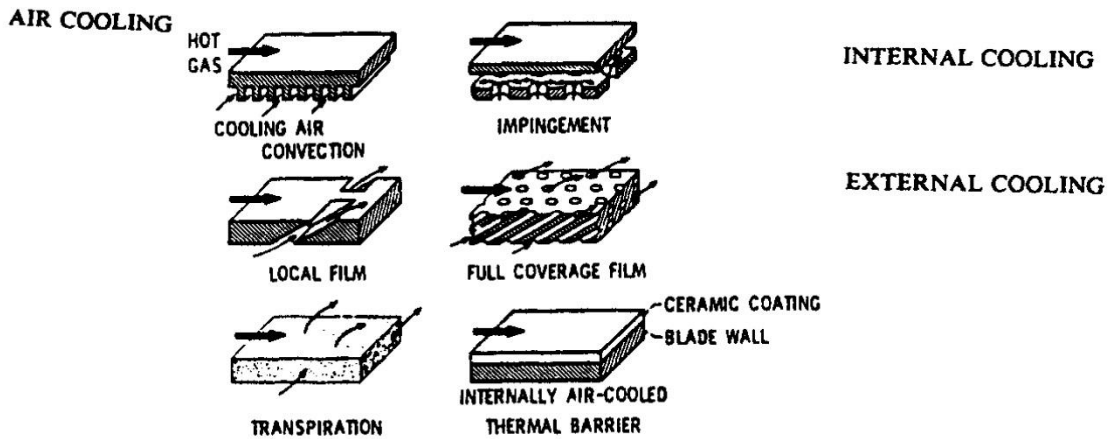


Figure 1.6. Cooling mechanisms used in gas turbine components (Lakshminarayana 1995).

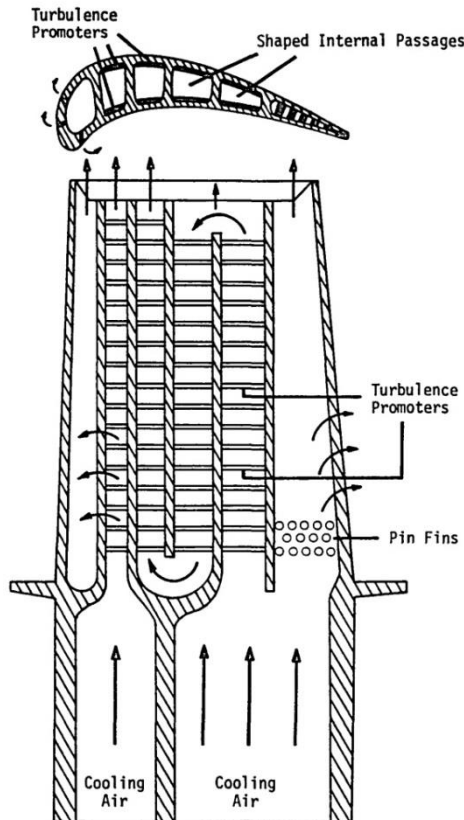


Figure 1.7. Internal and external cooling mechanisms applied to a turbine blade (Han et al. 1984).

In a further development, sophisticated cooling mechanisms were developed, which involved ejecting the coolant air through slots or holes. When external cooling is applied locally over the surface, it is described as film cooling. This method of external when combined with internal cooling allowed TIT to reach nearly 1900°C.

Researches are still being carried out in the area of external film cooling to achieve full coverage cooling mechanisms. One such type is transpiration cooling, as shown in Figure 1.6, where the blade is made up of porous materials. These techniques offer a great deal of challenges in terms of material strength and blockages. Also, the development of new alloy materials and the application of thermal barrier coatings in recent years further enhanced the component's ability to reach higher and higher inlet temperatures.

1.2 Film cooling

External cooling is achieved by creating slots or drilling holes over the blade surface. The cooling air is made to eject out of these holes, which can create an insulation layer of air over the surface and protect it from the high temperature gases. Figure 1.8 shows a conventional turbine blade with a film cooling arrangement, highlighting the mechanism of film cooling through a single hole.

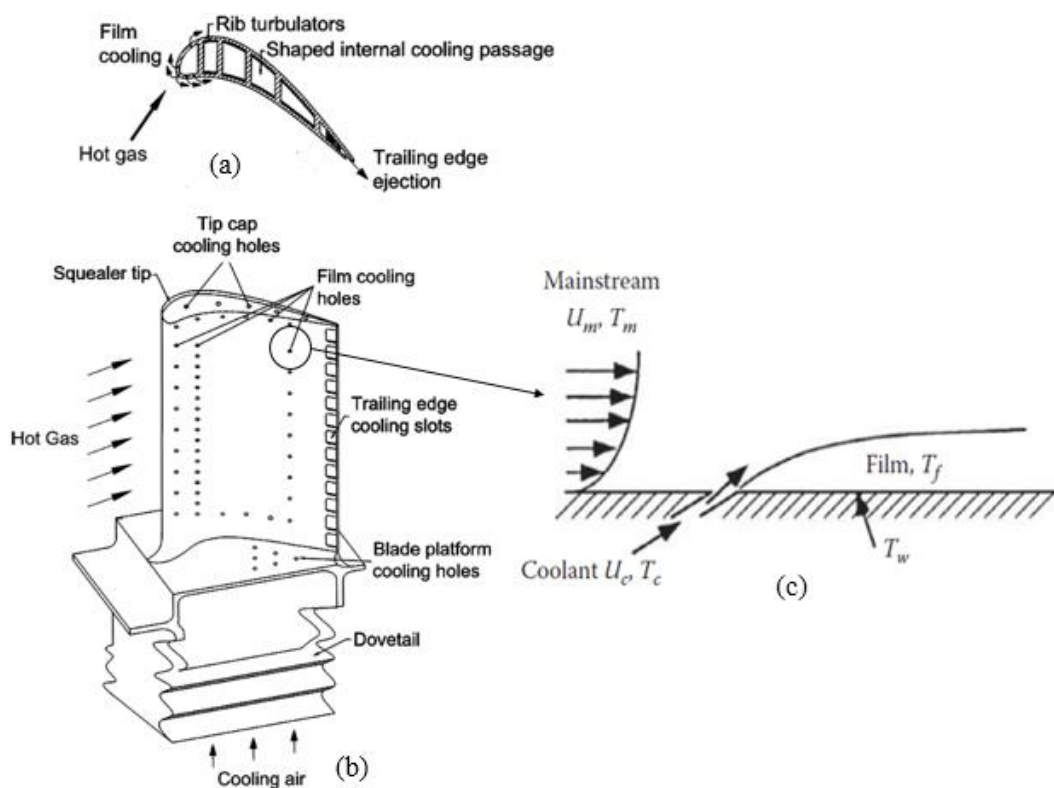


Figure 1.8. Film cooling arrangement over a turbine blade (a) Cross-sectional view (b) Three-dimensional view (c) Film cooling mechanism exaggerated over a single hole (Han et al. 2012).

Once the coolant air enters inside a turbine blade, it is used to absorb excess heat through the internal cooling technique and then discharged from the holes to create film cooling. The film cooling holes are drilled at a certain inclination so that the coolant coming out of the hole gets deflected by hot gases towards the wall creating a protective layer of film over the surface. A new way of external cooling technique is being attempted recently, known as transpiration cooling. In this type of cooling, the blade is made of porous materials to allow the coolant to flow through it. However, this offers structural challenges, and the pores are prone to frequent blockages leading to a loss in performance.

The film cooling creates a highly complicated three-dimensional flow while interacting with the hot gases inside the turbine. A small error in the prediction of the hot gas flow path can lead to a significant reduction in the life of the components. Hence it is certainly challenging for the design engineer to calculate the exact metal temperature and local heat transfer coefficient to identify the hotspots developing over the components.

The film cooling performance is evaluated by calculating the amount of heat flux reduced over the actual heat flux received by the surface when there is no film cooling. The total reduction in heat flux due to film cooling is expressed in terms of Net Heat Flux Reduction Ratio (NHFR) as,

$$NHFR = \frac{q_0'' - q_f''}{q_0''} = 1 - \frac{q_f''}{q_0''} \quad (1.2)$$

where q_f'' is the heat flux received by the surface in the presence of film cooling and q_0'' is the heat flux in the absence of film cooling.

The heat flux over any surface can be calculated according to Newton's law of cooling as,

$$q'' = h(T_w - T_m) \quad (1.3)$$

where h is the local heat transfer coefficient, T_w is the wall temperature and T_m is the temperature of the mainstream. When the flow of mainstream is added with an additional fluid stream having dissimilar temperatures, as in the case of film cooling, the fluid temperature becomes a mixture of two streams. Hence, to calculate the heat flux for a film-cooled surface, Equation (1.3) can be written as,

$$q_f'' = h(T_w - T_{ref}) \quad (1.4)$$

The term T_{ref} is known as reference temperature and h is the heat transfer coefficient over a film cooled surface. Therefore it is essential to evaluate these two parameters to determine the performance of a film cooling design. The reference temperature, T_{ref} , in Equation (1.4) is non-dimensionalized using the mainstream temperature, T_m , and the coolant temperature, T_c , known as film cooling effectiveness (η) which is expressed as,

$$\eta = \frac{T_{ref} - T_m}{T_c - T_m} \quad (1.5)$$

There will be multiple film cooling holes located in a row at the surface of turbine blade. Hence, the lateral variation of effectiveness depends on the pitch of the hole. Typically, in most of the cases the local effectiveness is averaged over the lateral direction over the film cooled surface while analyzing the film cooling performance known as laterally averaged effectiveness ($\bar{\eta}$), which is defined as,

$$\bar{\eta} = \frac{1}{P_f} \int_{z/d = -P_f/2}^{z/d = +P_f/2} \eta(x/d, z/d) d(z/d) \quad (1.6)$$

The film cooling effectiveness and heat transfer coefficients are the two major parameters that decide the performance of a film cooling configuration. However, these two parameters intern depends on geometrical aspects as well as flow features such as cooling hole shape, injection angle, hole length, the distance between the holes, surface curvature and roughness, velocities and densities of the fluid streams, Reynolds number and turbulence intensity.

These two parameters of film cooling are evaluated independently by conducting separate experiments for each of the parameters. The reference temperature is calculated by insulating the wall and measuring the adiabatic wall temperature at a steady state. In this case, the free-stream and the coolant will be at different temperatures. While evaluating the heat transfer coefficient, a constant heat flux will be applied over the test surface using thin foil heaters and the corresponding wall temperature is measured. Subsequently, the heat transfer coefficient is evaluated

by applying Newton's law of cooling as given in Equation 1.4. This is carried out by keeping the mainstream and the coolant at the same or at different temperatures.

1.2.1 Flat-plate film cooling

Film cooling holes are made in various locations on an aerofoil. The areas such as the leading edge, blade tip, trailing edge and end walls that are prone to extreme temperature are protected by film cooling with a single row or multiple rows of holes. Each parameter of film cooling can have different effects on the performance depending on the location of the hole. The real engine condition involves many factors, and such boundary conditions are extremely difficult to reproduce during experiments. Hence, most film cooling studies relied on flat plate models to establish a basic understanding of flow physics and its mixing behavior. A vast number of previous researches were carried out using the flat plate model to develop novel concepts of film cooling configurations.

1.3 MOTIVATION BEHIND THE STUDY

Present film cooling technique employs generally cylindrical holes which are drilled at certain angles so that the coolant exit occurs parallel to the mainstream. One of the major challenges in film cooling is to keep this coolant flow as close as possible to the surface at any possible mass flow rates. Apart from cylindrical holes researchers have studied varieties of hole shapes and studied their effect on film cooling. With this intuition the present study was started so as to develop a novel film cooling hole concept and to study its effect on film cooling behavior.

To study the effect of a new hole shape, an experimental approach can provide a quantitative measure of film cooling behavior. But, it can become very tedious to arrive at a suitable design when there are multiple parameters are being involved. Hence, one can go for numerical simulation at the initial stage to understand the effect of those parameters. Again, when it comes to numerical techniques it is important to look for the accuracy of the solution and the computational resource requirement. One of the most widely used numerical method is to use RANS (Reynolds Averaged Navier-Stokes) based turbulence models to evaluate the turbulent flow characteristics.

There are other numerical techniques such as Large Eddy Simulation (LES) or Direct Numerical Simulation (DNS), which can predict the film cooling behavior with utmost accuracy. But the major drawback of these methods are that they need significant computational resources.

Recently, a distinct feature for coolant flow was explored by considering the swirl effect. Also, swirled flows are one of the effective techniques in enhancing heat transfer rate in case of flame jet impingement studies. In such applications a simple twisted tapes were used inside the impinging nozzles to obtain the desired swirl. This lead to the idea of using twisted tapes for coolant swirl generation in film cooling applications. Hence, in the present study, a RANS based numerical simulation is chosen to obtain an overall idea of film cooling behavior in the presence of twisted tape insert. This study can provide a qualitative measure of film cooling behavior and its feasibility in enhancing heat transfer characteristics when compared with a simple cylindrical hole film cooling.

1.4 OVERVIEW OF THE RESEARCH

This thesis is intended to study and understand the film cooling behavior over a flat surface through steady state and transient data analysis. The work was initially started with an experimental approach to obtain the desired data. During the experiment, a thin-foil technique was applied over the film cooled surface to measure the temperature using an infrared camera. Though the experimental work produced a moderate film cooling behavior, the accuracy of the benchmark study was unacceptable. This might have occurred due to inherent noise in the wind tunnel apparatus. The efforts taken to inhibit the noise were just futile. Hence, the experimental attempt was halted and the study further continued with the aid of numerical simulations.

Initially, as part of the validation, a simple inclined cylindrical hole film cooling case is simulated and compared against measured results in the literature. In this case, the numerical results suffer due to approximate turbulence closure quantities and near-wall mesh resolution dependencies. Hence it was challenging to obtain precise validation even though most of the physical boundary conditions are respected

while developing the computational model. Ample efforts have been put into analyzing the accuracies of various turbulence models.

Once the computational model was set up, the geometrical aspect of film cooling hole was investigated by modifying the cylindrical shape. The effect of such modifications on the flow features was also explored. Further, concepts such as neural network models and global optimization strategies are utilized to arrive at the most favorable geometric combination. Similarly, the temporal wall temperature data was collected from the numerical simulations for the transient analysis. An inverse heat transfer approach was employed to develop a data reduction technique using transient data to evaluate film cooling performance parameters.

1.5 OUTLINE OF THE THESIS

In the present thesis, a novel concept of film cooling is proposed based on generating a swirl on the coolant flow using a twisted tape insert. The film cooling performance in the presence of a twisted tape insert is evaluated through numerical simulations and compared with conventional design. The geometrical parameters influencing the performance is optimized with the help of advanced techniques such as artificial intelligence and evolutionary-based optimization algorithm. Also, a novel data reduction technique for solving the problem in transient film cooling situations using inverse heat transfer theory is proposed.

Chapter 2 presents a brief review of the literature to understand the current status of existing film cooling hole designs and the methods involved in optimizing the parameters. The advantages and disadvantages of various methods proposed in the earlier works regarding the transient film cooling techniques are also reviewed.

Chapter 3 explains the solution methodology applied in the present numerical work. The critical variables involved in developing swirled film cooling are described.

A detailed discussion of numerical results from swirled film cooling with respect to base design is given in chapter 4, along with the performance evaluation of film cooling at geometrical variables such as the hole length and the coolant injection angle in the presence of various swirl intensities.

The chapter 5 is dedicated to evaluating an optimum geometrical configuration by applying the concept of artificial neural network and genetic algorithm.

The last chapter presents a method to simultaneously calculate film cooling effectiveness and heat transfer coefficient in case of transient film cooling problems for a conventional flat plate film cooling case. [Equation Chapter \(Next\) Section 1](#)

CHAPTER 2

LITERATURE REVIEW

Since the inception of film cooling technique in gas turbine engines, enormous studies have taken place to improve its performance. This chapter provides a comprehensive review of the previous studies and the present status of the current topic.

The initial work on film cooling was started around 1930s, while the coolant injection was studied through continuous inclined slots that can be assumed as a two-dimensional film cooling flow. The works prior to 1970 were reviewed by Goldstein (1971) and subsequently, the application of round inclined jets through discrete orifices was developed (Goldstein et al. 1968a). This led to the formation of three-dimensional flow structures for the coolant flow due to higher interaction between the two fluid streams than the slots. Later, tremendous developments happened in the field of film cooling through discrete holes. Most of these studies are confined to evaluating film cooling performance parameters such as effectiveness and heat transfer coefficient with various aspects of geometrical and flow related parameters.

2.1 INFLUENCE OF FLOW PARAMETERS

2.1.1 Blowing ratio

One of the most influential parameters in film cooling is the blowing ratio. It is defined as the ratio of the mass flux of coolant to the mass flux of mainstream which is represented by the term M and is given as,

$$M = \frac{\rho_c U_c}{\rho_m U_m} \quad (2.1)$$

where ρ and U represent the density and velocity. The subscripts c and m denote the coolant and mainstream, respectively. The blowing ratio is the product of the density and velocity ratios. The density ratio has a minor effect on film cooling performance, whereas the velocity ratio affects it significantly. In film cooling, the aim is to keep

the coolant fluid adhered over the surface to obtain a maximum cooling effect. Film cooling should be able to cover the surface not only in the vicinity of the hole, but it should cover the downstream region also. Unfortunately, with increased TIT, more coolant mass flux is required to keep the surface temperature below its operating limit. This creates the ejection of coolant with higher velocity. As the coolant velocity is increased, the jet momentum tends to increase and the coolant will try to penetrate the mainstream resulting in a detached jet. As a result, the jet separates from the wall and the cooling efficiency drops significantly, leading to the deterioration of film cooling performance.

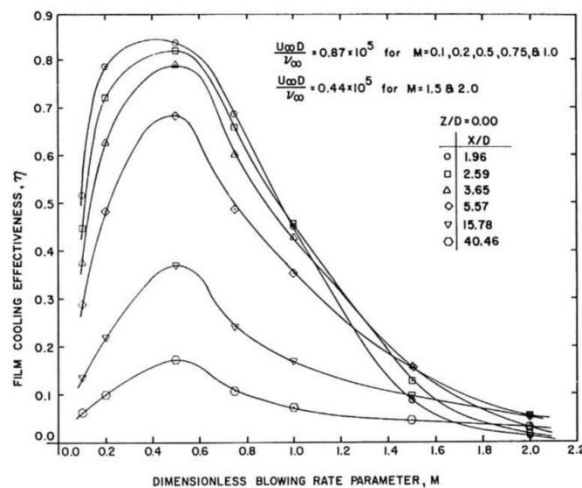


Figure 2.1. Effect of blowing ratio on effectiveness (Goldstein et al. 1968a).

A typical gas turbine operates at a blowing ratio of 0.1 – 2; hence, most of the film cooling studies were conducted in the same range. Goldstein et al. (1968a) experimentally investigated the effect of blowing ratio on effectiveness for an inclined circular hole at 35° with a diameter of 25mm, as shown in Figure 2.1. It was observed that M is helpful only up to 0.6 and a further increase is counterproductive. However, Jabbari and Goldstein (1977) observed that if two staggered rows of holes are made, then coolant can be supplied at a higher blowing rate.

The effect of blowing ratio on heat transfer coefficient is studied by Hay et al. (1985) is presented in Figure 2.2 for 35° and 90° coolant injection through a circular hole. They observed a continuous increase in h with M at any downstream location after injection but at a particular M the values are decreasing along x/d . They concluded that, though the effect of h on M seems minimal as compared η , but

neglecting this effect could over estimate the life span by 20%. Eriksen and Goldstein (1974) reported that at $M = 2.0$, there could be an increase in h up to 27% when compared with the case of no film cooling when a row of holes is present. It is pointed out that the peak values of h occurred at the outer edges of the jets located in between the two adjacent jets. Their results were further justified by Mayle and Camarata (1974) and Metzger et al. (1973).

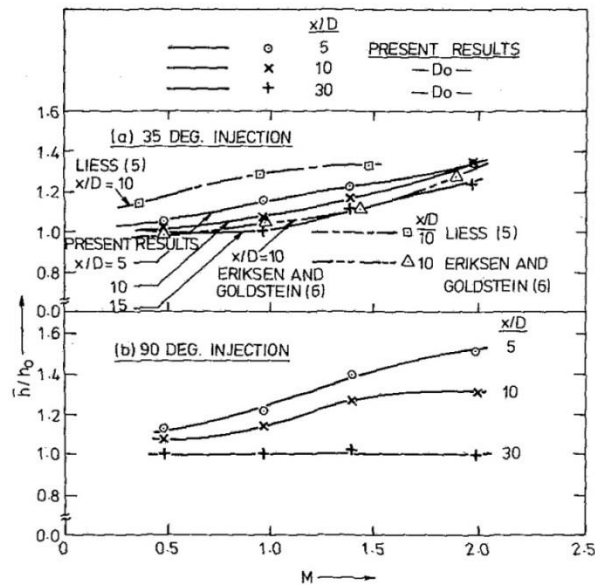


Figure 2.2. Variation of h with M (Hay et al. 1985).

2.1.2 Density ratio (DR)

The actual operating conditions of film cooling will have significant temperature differences between the mainstream and the coolant. The ratio of absolute temperatures of two streams T_c/T_m is directly related to the density variation. Hence the ratio of temperature is represented in the form of a quantity known as the density ratio ρ_c/ρ_m .

Pedersen et al. (1977) studied the effect of density ratio on film cooling effectiveness through a mass transfer analogy. They used refrigerant Freon-12 as the coolant to obtain a density ratio in the range of 0.75 to 4.17. They observed a strong influence of density ratio on effectiveness. Pietrzyk et al. (1989) conducted a detailed experiment on the hydrodynamics of film cooling flow having a density ratio of 2 while keeping $M = 2$ and compared their results with unit density ratio cases.

Figure 2.3 shows the distribution of velocity vectors for the case of $DR = 1$ and 2 as obtained by Pietrzyk et al. (1989). They noticed the vectors are more tilted away from the wall for unit density ratio than for a high density ratio case. This indicated that the jet possesses a lower penetration tendency at high density ratios. Later Sinha et al. (1991) studied the effectiveness distribution at $DR = 1.2, 1.6$ and 2.0 and their observation is shown in Figure 2.4. They found that the laterally averaged effectiveness improves significantly with increase in density ratio.

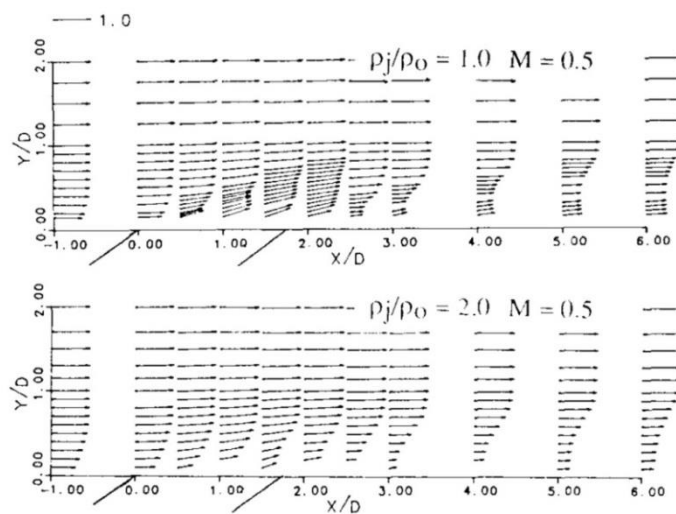


Figure 2.3. Effect of density ratio on coolant distribution (Pietrzyk et al. 1989a).

Similarly, the effect on heat transfer coefficient is found to be around 10% higher for a jet with a unit density ratio than $DR = 1.52$ (Ammari et al. 1989). This effect could be due to lower turbulence levels in the dense jets than unit density jets (Pietrzyk et al. 1989b).

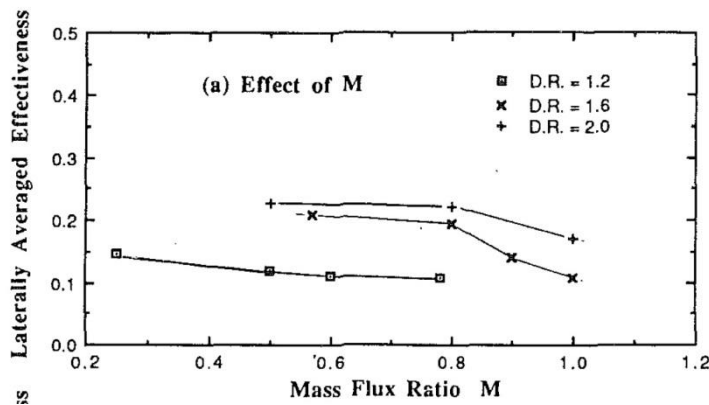


Figure 2.4. variation of $\bar{\eta}$ at different density ratios (Sinha et al. 1991).

2.1.3 Mainstream turbulence

Film cooling takes place under the turbulence level having a turbulent mixing coefficient of 0.15 inside a combustor, but the wind tunnel experiments are generally conducted with a value of around 0.01 (Marek and Tacina, 1975). Hence it is essential to study the effect of free-stream turbulence on film cooling. It was observed that turbulence intensity decreases the film cooling effectiveness. The turbulence intensity was observed to increase with the blowing ratio (Kamotani and Greber 1972). Later, a study conducted by Bons et al. (1994) and also by Schmidt et al. (1996) observed that the statement of Marek and Tacina (1975) holds true only for low to moderate blowing ratios. However, at high blowing ratios, turbulence intensity increased the diffusion of coolant and reduced the jet lift-off resulting in increased effectiveness. Blair (1983) studied the influence of different freestream turbulence intensities ranging from 0.25% to 7% and reported an increase in heat transfer rate with turbulence levels. Also, in a study, the effect of boundary layer thickness was observed to be dominant only in the vicinity of the hole (Kadotani and Goldstein 1979). In terms of jet characteristics, it was noted that a turbulent jet shows less penetration than a laminar jet (Yoshida and Goldstein 1984).

2.2 INFLUENCE OF GEOMETRIC PARAMETERS

2.2.1 Hole length to diameter ratio

While studying film cooling characteristics, Goldstein et al. (1974) experimented on a short hole which is the thickness of the plate and a long hole. They did not observe any considerable effect of hole length on film cooling. Most of the studies on film cooling have adopted different L/d ratios and hence a direct comparison of their results would be imprecise. Lutum and Johnson (1998) systematically studied the effect of L/d ratio varying from 1.75 to 18. It was observed that short holes having $L/d < 5$ showed significant decrease in η than long holes whereas for $L/d > 7$ had mild to moderate effect. Burd et al. (1998) investigated a combined effect of L/d and turbulence intensity. They concluded that the effect of

L/d can be noticeable only at low turbulence intensity. On the other hand, as L/d ratio increased, htc was observed to decrease (Li et al. 2018).

2.2.2 Pitch-to-diameter ratio

Pitch-to-diameter (P_f/d) ratio gives the center-to-center distance between the two adjacent holes. Closely spaced holes might create a more uniform coolant distribution laterally. Meanwhile, the heat transfer coefficient may be enhanced due to increased interaction between the jets. When P_f/d is increased, nonuniform effectiveness develops, which could lead to local hotspots. Hence P/d need to be kept at an optimum value. Most of the film cooling research was conducted at a P_f/d ratio of 3. Figure 2.5 shows the distribution of coolant in the lateral direction given by Goldstein et al. (1974) for a cylindrical hole with $P_f/d = 3$. It can be observed that the outer edge of coolant jet spreads upto $1.5d$ from the center. In the far downstream, all the jets coalesces and produces more or less uniform spreading. Brown and Saluja (1979) investigated P_f/d ratio of 8.0, 5.33 and 2.67 and observed that η at P_f/d 8 was much lower than 2.67. Similarly with increased number of holes by reducing the pitch will increases the heat transfer coefficient (Andrews et al. 1988).

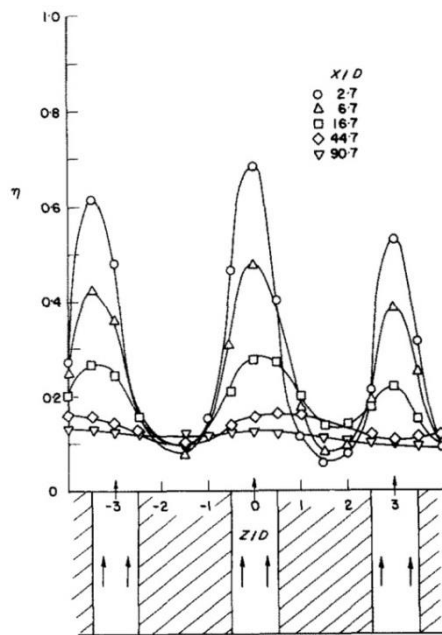


Figure 2.5. Lateral coolant distribution of coolant at different downstream locations (Goldstein et al. 1974).

2.2.3 Injection angle

Out of different geometrical factors, the angle of coolant injection is one of the parameters that significantly controls the film cooling behavior. If the film cooling hole inclination is given in the direction of the mainstream, it is referred to as the inclination angle and represented by α . Along with the inclination angle, if the hole is tilted to an angle normal to the mainstream, then there will be a compound angle (β). The compound angle is generally provided to enhance the lateral distribution of the coolant (Schmidt et al. 1994; Sen et al. 1996). An ideal injection angle should be able to inject the jet parallel to the surface. However, creating holes with very low inclination angles is extremely difficult. Hence, most film cooling studies have adopted an injection angle ranging from 30° - 50° .

Bergeles et al. (1975, 1977) studied flow characteristics for a jet injected normally and at 30° to the mainstream. In a similar study carried out by Lee et al. (1994) in terms of flow visualization showed that (Figure 2.6) normal injection abruptly mixes with mainstream, whereas a 35° inclined jet gradually diffuses. An investigation on film cooling effectiveness and heat transfer coefficient was conducted experimentally for a cylindrical hole at inclination angles of 30° , 60° and 90° (Yuen and Martinez-Botas 2003, 2005). They observed nearly 20% higher η for 30° injection than 60° and 90° . Meanwhile, the heat transfer coefficient for 30° was found to be higher than 60° and 90° . A possible explanation for such behavior was that a shallow jet interacts closely with the wall, creating more disturbance in the boundary layer. A comparison of slant and normal jet in terms of Stanton number (St) was made by Crawford et al. (1980) and observed a significant difference in St between the two variants at low blowing ratios. When M increases, both jets tends to behave in a similar way producing close values of St .

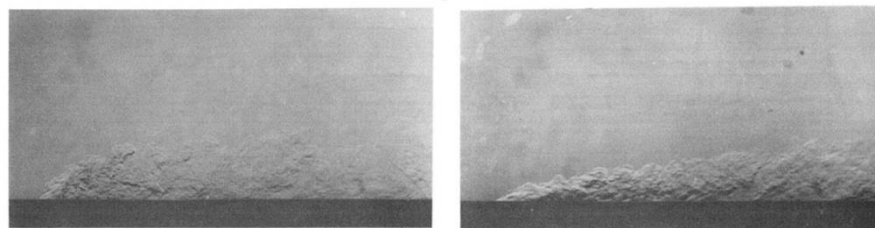


Figure 2.6. Flow visualization of normal and inclined jets at a velocity ratio of 0.5 (Lee et al. 1994).

2.2.4 Surface roughness

Goldstein et al. (1985) experimentally investigated the effect of surface roughness on a flat plate with six roughness patterns. The effectiveness was found to increase with the blowing ratio for all the cases of roughness compared to a plate with no roughness. However, the effect was observed to be small, where the roughness affected the effectiveness to decrease (Schmidt et al. 1996). Further, it was examined by combining rough surfaces with high freestream turbulence resulted in improved effectiveness. Meanwhile, there is an increase in heat transfer rate by around 100% (Schmidt and Bogard 1996). But, Barlow and Kim (1995) observed an increase in heat transfer of 3% to 21% for a rough surface with an increasing blowing ratio, while a smooth surface showed nearly 20% to 30% for the same conditions.

2.2.5 Curvature

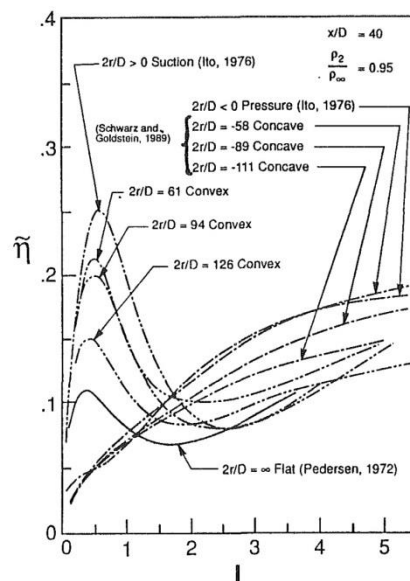


Figure 2.7. Effect of curvature on film cooling effectiveness (Schwarz et al. 1991).

Most film cooling studies were conducted on flat surfaces with zero pressure gradient conditions. When a film cooling configuration is applied to actual turbine blades, the effect of surface curvature gives rise to the development of pressure gradients over film cooled surfaces. In an initial study, a flat plate with a favorable pressure gradient was examined, which resulted in an increase in the Nusselt number with increased turbulence level in the presence of a laminar boundary layer (Junkhan

and Serovy 1967). A comparison of film cooling over convex and concave surfaces resulted in an improved lateral coolant distribution on a concave surface. In contrast, a convex surface produces peak effectiveness near the hole (Ko et al. 1986).

Figure 2.7 shows the result obtained by Schwarz et al. (1990) at various radius of curvature of the surface as compared with a flat surface. It was found that laterally averaged effectiveness obtained over a convex wall is higher than a flat plate, especially when the blowing ratio is low. Concave surfaces tend to reduce η at low blowing ratios, but it significantly improves effectiveness at high blowing ratios.

2.2.6 Effect of cooling hole geometry

The geometry of the film cooling hole is one of the significant parameters which can control the coolant distribution. A hole exit shape can considerably reduce the coolant penetration at high blowing ratios leading to an increase in η . In an early work, Goldstein et al. (1974) compared a cylindrical hole with a shaped hole having expanded at the exit. They observed a substantial increment in effectiveness over a simple hole. Later on, in an attempt to improve the film cooling performance, numerous studies were carried out in terms of hole shape. The studies pertaining to various hole shapes will be discussed in detail in a later section.

2.3 FILM COOLING FLOW FEATURES

When a coolant jet issues out of the hole, a complicated three-dimensional flow field exists downstream of injection. In order to predict such flows, it is essential to understand the nature of the interaction of the two streams. Jet in a cross-flow situation has many applications, including film cooling technique. Earlier studies on a jet in cross-flow cases examined flow features through normal injection across a mainstream (Andreopoulos and Rodi 1984; Broadwell and Breidenthal 1984; Crabb et al. 1980; Fric and Roshko 1994; Peterson and Plesniak 2004; Smith and Mungal 1998). They observed the following flow characteristics,

1. Jet bending at low velocity ratios and penetration at high velocity ratios.
2. Reverse flow occurs in the wake, behind the jet and filled with cross flow.
3. Interaction of the jet with the cross-flow generates vorticity.

4. There are jet shear-layer vortices, horseshoe vortices, wake vortices and counter-rotating vortex pair (CRVP), as shown in Figure 2.8.

5. The wake region can be categorized into a near-field region where CRVP develops, a far-field region where fully developed CRVP occurs and a vortex interaction region which exists below the jet.

6. The CRVP originates from the supply channel of the jet. Hence its strength depends on the in-hole vortex characteristics.

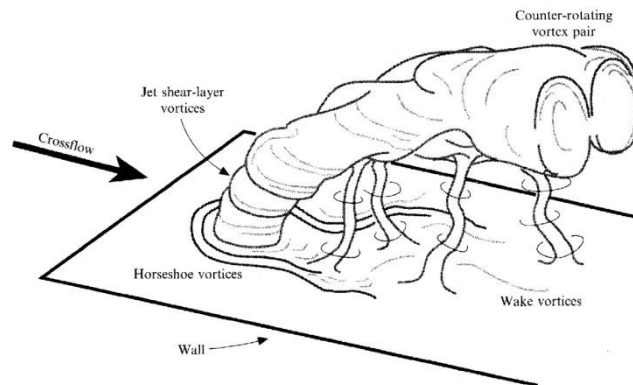


Figure 2.8 Vortical structures generated from a normal jet-cross flow interaction (Fric and Roshko 1994).

These studies were implied to an inclined jet in cross-flow situations such as film cooling flows where similar flow features were observed. For a short length hole, the direction of coolant entry into the plenum was observed to affect the CRVP strength and it was able to reduce the jet penetration by around 35% (Peterson and Plesniak 2002). Meanwhile, the skin friction along the downstream location was increased with the blowing ratio (Peterson and Plesniak 2007). It was noted that the CRVP is the main reason which brings the mainstream flow near the wall (Coletti et al. 2013). When the velocity ratio is less, the dominating flow characteristic is a hairpin vortex, whereas CRVP replaces the hairpin vortices as the velocity ratio is increased (Dai et al. 2016). Thole et al. (1997) studied the effect of crossflow at the entrance of the hole in modifying the coolant exit profile, which occurs in turbine blades when the coolant enters the film hole after the internal convection cooling. They observed a separation region at the hole entrance when the internal cross-flow has a high velocity, leading to skewed jet exit profiles and a higher mixing rate.

2.4 COMPUTATIONAL STUDIES ON FILM COOLING

With the development of computational capabilities, efforts were made to predict the film cooling behavior using numerical models. Numerous works exist on film cooling evaluation through computational fluid dynamics (CFD). Kercher (1998) presented a list of all the works reported during 1972-1996 related to CFD analysis on film cooling.

Crawford et al. (1980b) developed a two-dimensional boundary layer program to predict the Stanton number over a flat plate injected with a coolant. A turbulence augmentation model handles the coolant injection into the boundary layer. Later this program was modified to include the heat flux and adiabatic wall boundary conditions to obtain film cooling effectiveness and heat transfer coefficient (Miller and Crawford 1984). Demuren et al. (1985) applied a three-dimensional partial differential equation solver combined with a nonisotropic $k - \varepsilon$ turbulence model to compute film cooling effectiveness for varieties of cases. Coolant injection was studied for $\alpha = 10^\circ, 45^\circ$ and 90° whereas the hole spacing was varied from 1.5 to 5 times diameter with blowing ratios of 0.5, 1 and 2.

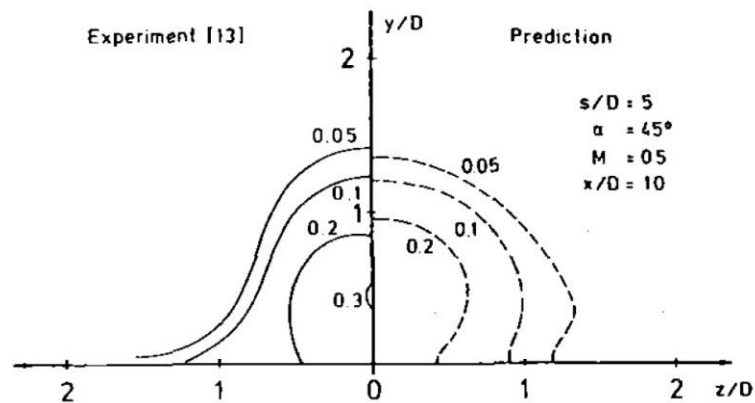


Figure 2.9. Predicted temperature vs. measurement (Demuren et al. 1985).

Figure 2.9 shows a comparison of the predicted temperature field with the measurements. It was observed that the inner edge of the coolant jet was overpredicted while the outer edge was slightly underpredicted. This behavior was more predominant as the blowing ratio is increased. A numerical study on slot film

cooling identified the main source of the turbulence generator, which exists in the shear layer of the jet and crossflow region (Sarkar and Bose 1995).

Leylek and Zerkle (1993) carried out a comparative study of the CFD results with the experiment. They used an orthogonal mesh configuration and employed standard $k - \varepsilon$ turbulence model in their study. They emphasized modeling the flow through the plenum in order to generate actual inlet conditions at the entrance of the film hole. When the coolant is made to enter through a plenum, it creates the flow inside the film hole to undergo a jetting effect when a short hole is used, as shown in Figure 2.10. However, their prediction of centerline effectiveness was relatively higher than the experiments.

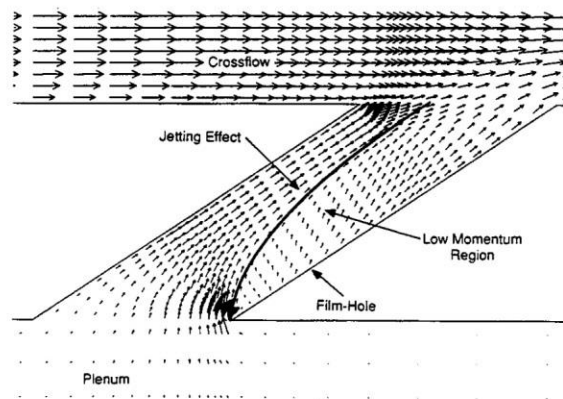


Figure 2.10. Velocity vectors inside a film hole (Leylek and Zerkle 1993).

Walters and Leylek (1996) attempted an improvement over the previous study, using a triangular mesh. They obtained a better prediction of η at a low blowing ratio but overpredicted results at higher blowing ratios. They suggested a correction over the computational results for possible jet skewness errors during experiments. In a further study, it was attempted to improve the film cooling prediction with a two-layer zonal model by resolving near-wall flow using fine meshes (Walters and Leylek 1997). Later, Ferguson et al. (1998) explored the capability of various turbulence models, such as standard $k - \varepsilon$, RNG $k - \varepsilon$ and Reynolds stress models having generalized and non-equilibrium wall functions in estimating film cooling behaviour. They concluded that standard $k - \varepsilon$ model with two-layer zonal model as wall function predicted better than other variants. But the jet separation behavior at high blowing ratio was not resolved by any of the models. Hoda and Acharya (1999)

tested seven different turbulence models and obtained velocity and turbulence statistics at various locations. They suggested a requirement for a non-linear model to precisely predict the anisotropic nature of the flow. This study was further investigated by employing advanced models such as Large Eddy Simulation (LES) and Direct Numerical Simulations (DNS) (Acharya et al. 2001). It was observed that the LES and DNS demonstrated significant improvements over Reynolds Averaged Navier-Stokes (RANS) calculations. They also emphasized the importance of the coolant supply tube and the plenum in film cooling calculations.

Guo et al. (2006) conducted an LES study for a normal and inclined jet at 30° to the mainstream and observed a recirculation region in the immediate downstream where coolant and mainstream both were entrained. Additionally, it was discovered that the LES was able to get flow characteristics, including the horseshoe vortex and DSSN (Downstream Spiral Separation Node) vortex, in addition to the CRVP (Peet and Lele 2008). In another study by Harrison and Bogard (2008a), both effectiveness and heat transfer coefficients were predicted using different turbulence models. It was observed that the laterally averaged η and h predicted by $k - \omega$ model was closely complying with the experimental results. Mazzei et al. (2017) ascertained that the accuracy of a numerical film cooling model entirely depends on the ability of the turbulence model to precisely predict the coolant-mainstream interaction. An investigation into the origin of CRVP and the reattachment phenomena was conducted by Li et al. (2016). In this study, the jet separation and reattachment were successfully captured. They identified that in-tube vortices do not contribute to the formation of CRVP instead, it is formed in the shear layer due to Kelvin-Helmholtz instability. The strength of CRVP majorly influenced the jet lift-off and reattachment phenomena. Lately, CFD simulations are widely being used to develop novel hole shapes and geometrical configurations to enhance the film cooling capability of existing configurations.

2.5 FILM COOLING HOLE SHAPES

The geometry of the film cooling hole is one of the most influential parameters in improving performance. Hence, extensive attempts were made to

develop film cooling holes with various geometrical configurations through experiments as well as numerical simulations. Followed by the work of Goldstein et al. (1974), Makki and Jakubowski (1986) proposed a diffused trapezoidal hole shape. Thole et al. (1996) experimentally investigated three different hole geometries, as shown in Figure 2.11. Due to a reduction in jet penetration, these geometries produced higher effectiveness than the cylindrical holes.

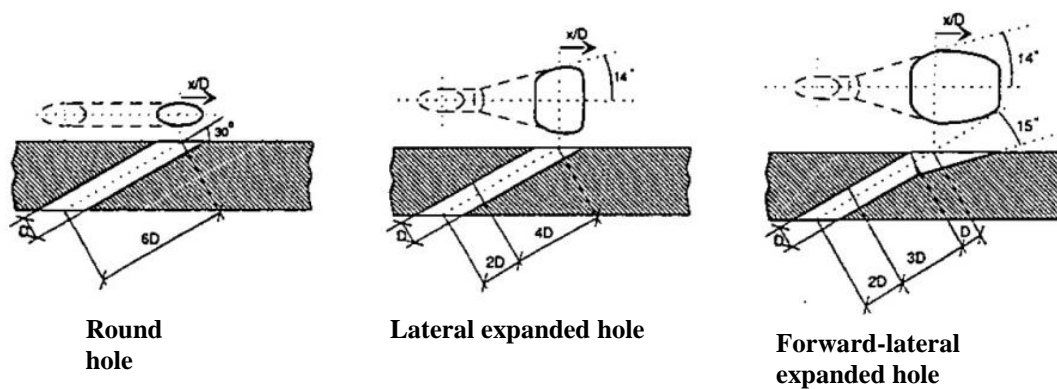


Figure 2.11. Film cooling hole geometries studied by Thole et al. (1996).

Since CRVP significantly affected coolant jet separation from the wall, Haven and Kurosaka (1996) experimented by artificially inducing vortices in a direction opposite to CRVP. This will counteract the effect of CRVP and reduces jet lift-off. It was explored that by increasing the lateral dimension of the hole, the distance between the CRVP increases and hinders the jet separation (Haven et al. 1997).

Bunker (2005) presented a comprehensive review of various hole shapes studied prior to 2005 and concluded that the shaped hole improves effectiveness while not affecting heat transfer considerably compared to conventional circular-shaped holes. Meanwhile, higher aerodynamic losses were reported due to the enhanced mixing of the two streams. Since then, many researchers have proposed numerous shapes, of which a few are provided below.

Ekkad and Han (2015) reviewed a few recently proposed hole shapes. The most widely studied configurations of different shapes are fan-shaped and laidback fan-shaped holes, as shown in Figure 2.12 (Bohn et al. 2003; Gritsch et al. 2000; Kang et al. 1999; McClintic et al. 2019; Saumweber and Schulz 2012; Thole et al. 1998). This configuration was investigated by varying its geometrical parameters such as forward and lateral expansion angles (Zamiri et al. 2020).

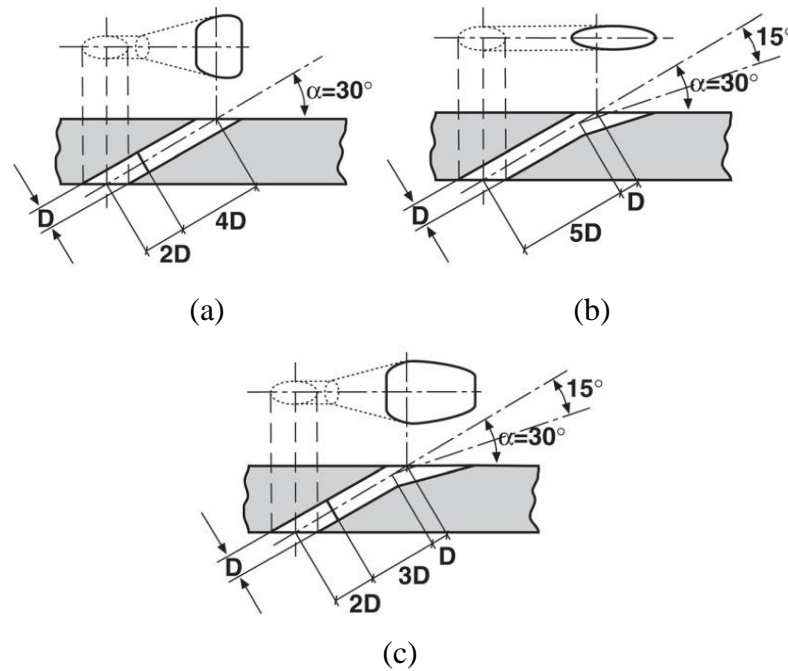


Figure 2.12. Geometrical profile of the variants of (a) Fan-shaped, (b) Laidback and (c) Laidback fan-shaped holes (Saumweber and Schulz 2012).

Bunker (2002) proposed the concept of coolant injection from a transverse trench, as shown in Figure 2.13. It was assumed that this configuration would produce similar effects to slot injection and make the coolant lateral distribution uniform. This configuration was further explored by Harrison and Bogard (2007), Lu et al. (2009), Waye and Bogard (2007) and Zuniga and Kapat (2009).

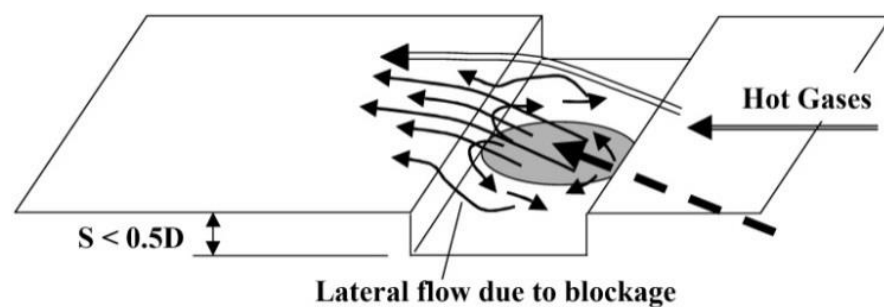


Figure 2.13 Coolant injection into a transverse trench (Bunker 2002).

A novel concept of antivortex design was proposed by Heidmann and Ekkad (2008), in which two holes were made in the direction of the main hole. These sister holes were connected to the main hole by providing a spanwise angle, as shown in Figure 2.14. The idea was to counteract the effect of CRVP by these sister holes. This

hole shape was further studied by Dhungel et al.(2009), LeBlanc et al. (2013), Narzary et al. (2011), Schulz et al. (2012), Yao et al. (2013).

In an attempt to create a coolant distribution similar to a slot cooling mechanism, Sargison et al. (2002) proposed the concept of a converging slot hole, also known as a console hole. Figure 2.15 shows the concept of console film cooling hole design. This concept resulted in an increased lateral distribution than the other existing configurations (Azzi and Jubran 2007; Liu et al. 2010; Sargison et al. 2005; Yao and Zhang 2011). Figure 2.16 and Figure 2.17 shows the different concepts of film cooling hole geometry proposed or investigated in recent literature.

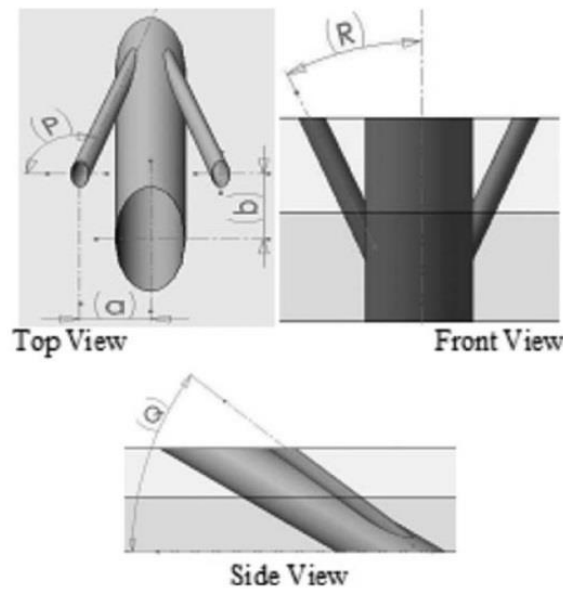


Figure 2.14. Concept of antivortex hole shape (Dhungel et al. 2009).

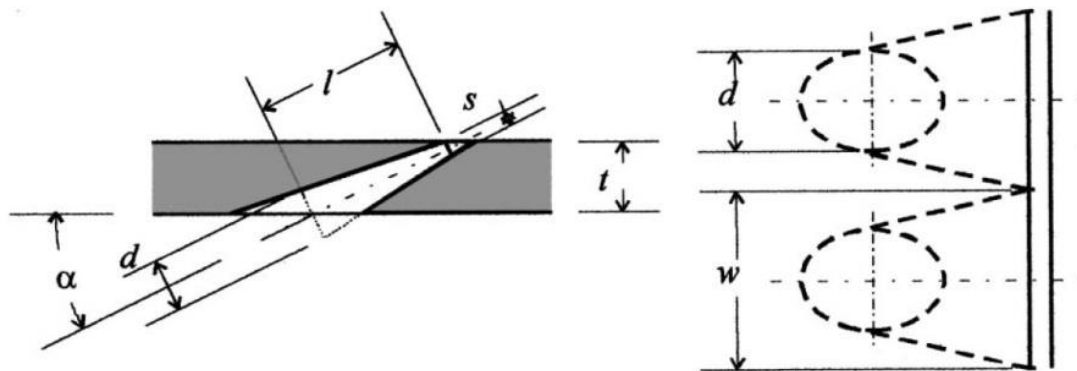
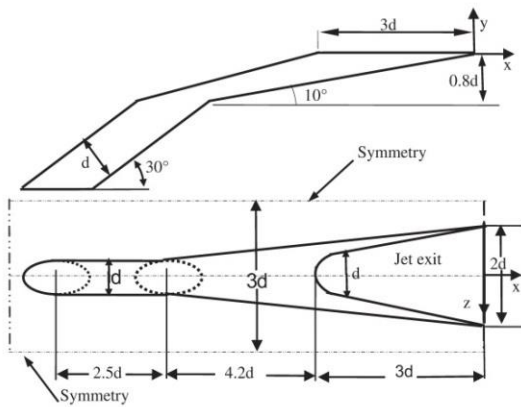
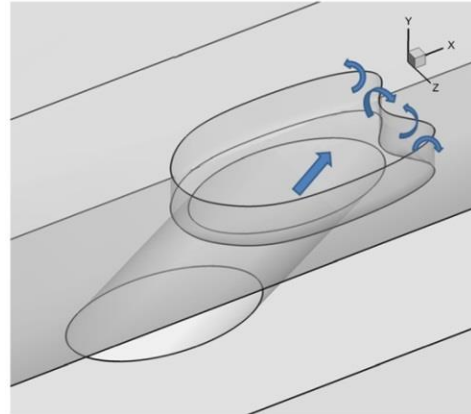


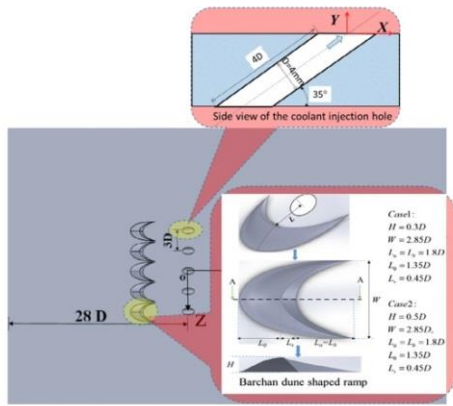
Figure 2.15 Converging slot type of film cooling hole design (Sargison et al. 2002).



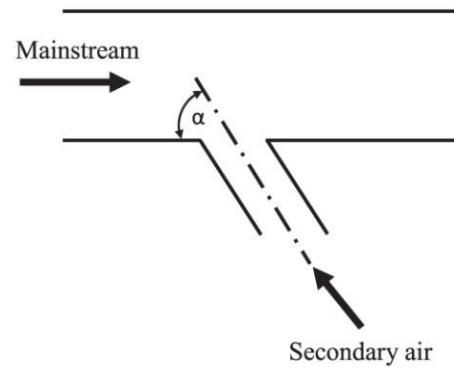
(a) Hybrid hole concept (Ghorab 2011).



(b) Film hole in a contoured crater (Kalghatgi and Acharya 2015).

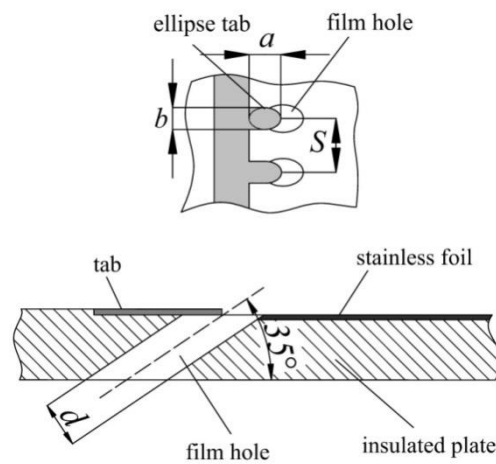


(c) Barchan dune shaped ramps (Zhou and Hu 2016).

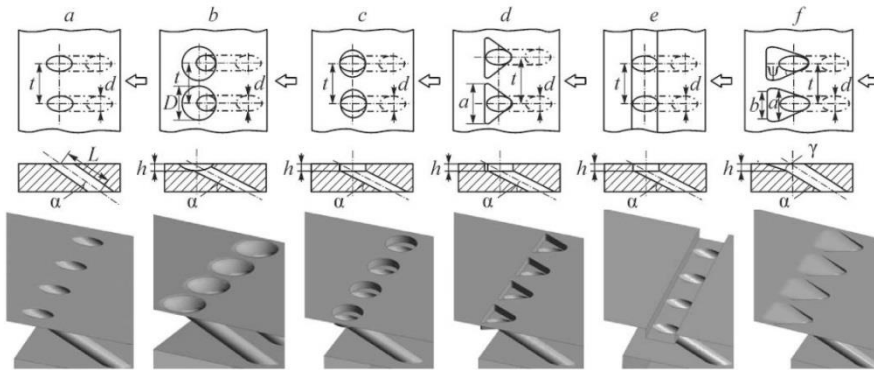


(d) Backward injection (Park et al. 2016).

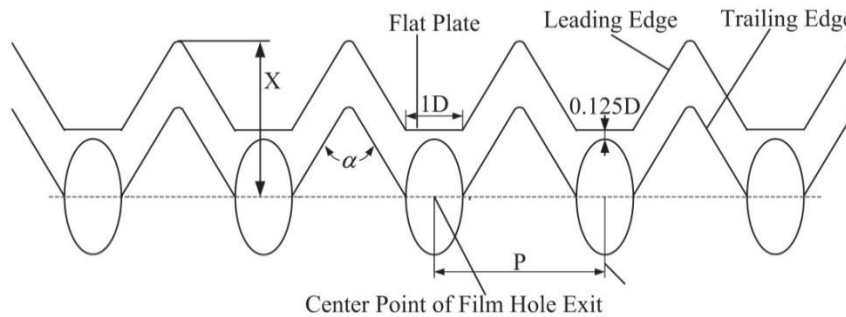
Figure 2.16. Recently investigated hole geometry configurations.



(a) Ellipse-shaped tab near the upstream exit of film hole (Yang et al. 2017).



(b) Indentations having different shapes (Khalatov et al. 2017).



(c) Coolant injection through a saw-toothed slots over the surface (Li et al. 2019).

Figure 2.17. Few advanced concepts of film cooling hole designs.

2.5.1 Swirled film cooling

In the case of a jet in cross-flow situations such as film cooling, the attachment of coolant over the film cooled surface mainly depends on the strength of the CRVP. Hence, in most of the recently investigated geometrical configurations, the emphasis was given to alleviating the effect of CRVP.

Out of the different parameters influencing the film cooling mechanism, the coolant swirl has been found to affect the structure of CRVP significantly. Kavsaoglu and Schetz (1989) experimentally studied the effect of a normal circular swirling jet with two different swirling ratios of 40 % and 58%. They defined the swirl ratio as the ratio of maximum angular velocity to the mean axial velocity. A Major observation from their study was that the swirl caused asymmetries in the surface pressure distributions and reduced the jet penetration. Later, Denev et al. (2005) conducted an LES study for a normal jet by varying the swirl numbers from 0 to 0.6 with an interval of 0.2.

The introduction of the swirl did not generate a higher rate of mixing, but the concentration profiles were affected by the swirl. In this case, the asymmetry of the jet existed till $x/d = 8$. In a measurement of scalar concentration profile showed that there could be possibility of around 20% reduction in penetration height (Niederhaus et al. 1997). This study was limited to low swirl numbers of up to 0.17. They reported that the swirl had modified the symmetrical kidney shape of the mean concentration profile into a comma shape. However, this effect was prevalent at low velocity ratios. As the velocity ratio increased, it appeared to suppress the effect of the swirl.

Bunyajitradulya and Sathapornnanon (2005) conducted experiments on swirling and non-swirling jets having a tab at the exit of the hole. Their jet was injected at an angle of 90° to the mainstream. In this case, the method of swirl generation was different from others as they used a rotating pipe to supply the coolant. The rotation of the supply tube imparted a peripheral velocity component to induce the swirl. The position of the tab was also varied by keeping the tab at certain lateral angles with respect to the mainstream direction. It was observed that the tab placed on the leeward side of the jet did not produce any noticeable changes in the flow structure.

To understand the mixing behavior of the swirling jet Yingjaroen et al. (2006) used an imaging technique for flow visualization. Denev et al. (2009) continued their previous work to explore the characteristics of the swirling jet through vorticity distribution and concentration field. They attempted to quantify the asymmetry induced by the jet flow due to the swirl.

In an experimental and numerical study conducted by Terzis et al. (2011) on a normal swirled jet, around a 58% reduction in penetration height was observed for a swirl number of 0.4. Figure 2.18 shows the jet trajectory along the downstream locations for different swirl numbers. The penetration height was obtained from a streamline emanating from the center of the jet.

While preceding investigations are restricted to coolant injection normal to the cross-stream, the concept of introducing a swirl has been extended to the case of slant angle injection, such as film cooling.

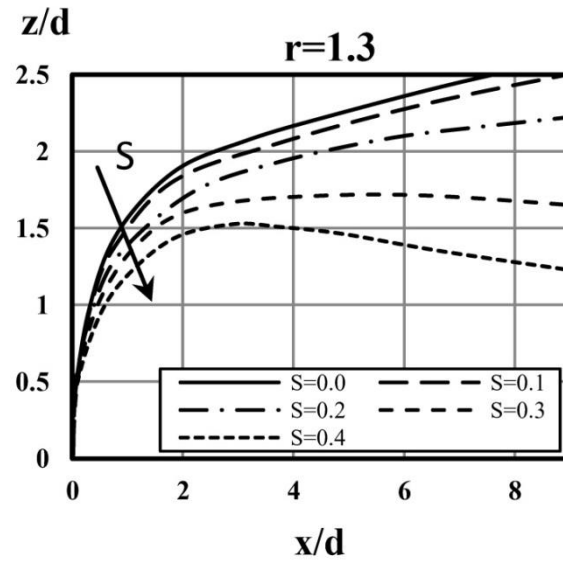


Figure 2.18. Reduction in jet penetration height with swirl number as observed by Terzis et al. (2011).

Modern turbine blades are cooled by employing different cooling mechanisms. The coolant for film cooling arrives from internal convection cooling and impingement cooling. The internal cavities inside a turbine blade are made in such a way as to produce a swirl so that internal cooling can be enhanced (Hedlund et al. 1999). The internal swirls are inevitably created while using special inserts, ribs, and turbulators to enhance heat transfer. In a few locations, such as leading edges, inducing swirl proved beneficial, which is obtained by providing tangential entry of coolant for the internal impinging jets (Liu et al. 2015). Even a rotating blade may induce some amount of swirl to the coolant flow through the Coriolis forces (Glezer et al. 1998). These swirled flows can be of continuous types, or they may decay along the path (Galeana and Beyene 2021). Recently Luo et al. (2014) studied the effect of internal rib structures on film cooling characteristics. They observed helical coolant motion inside the hole when the ribs were arranged at 45° . The induction of coolant swirl from the internal flow improved coolant attachment over the surface at high blowing ratios. An added advantage of swirled coolant flow is that it can remove additional heat from the internal surface of the film hole. Hence, it is important to explore the effect of coolant swirl on the film cooling performance.

Takeishi et al. (2010) proposed a novel concept of film cooling in which they artificially generated a swirl to the coolant flow and injected it through an inclined

circular hole at 30° to the mainstream and a shaped hole with an expanded exit. A modification is made inside the plenum chamber, as shown in Figure 2.19, to generate a coolant swirl before entering into the film hole. Two staggered impinging jets are positioned within the plenum chamber having slant angles of 0, 10, 20 and 30 to produce coolant swirl intensity of 0, 0.0289, 0.116 and 0.168. They observed a drastic improvement in the laterally averaged effectiveness of around 50% and 100% than a non-swirled case at $x/d = 10$ and 20, respectively.

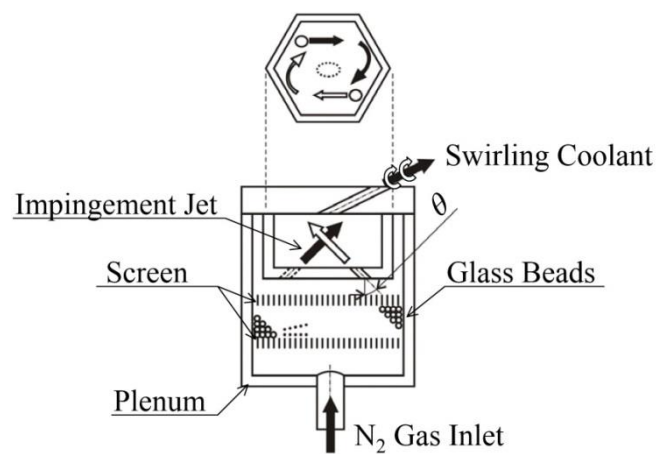


Figure 2.19. Mechanism of swirl generation used in the study of Takeishi et al. (2010).

To further explore a detailed mechanism of coolant interaction with the cross-flow, an LES study has also been performed (Oda et al. 2011). The reduction in heat transfer rate with the swirled flow was about 12%. The main feature behind the contribution towards obtaining higher effectiveness values for swirled film cooling was because of the degradation of CRVP. On the other hand, when the swirled cooling was implemented to a shaped hole resulted in lower effectiveness when the swirl number was 0.168. However, the swirl number of 0.0289 produced better results than the zero swirl case (Takeishi et al. 2013). Further, this study was extended to investigate the effect of swirl on an end wall of a turbine nozzle (Takeishi et al. 2014). In this case, maximum effectiveness was observed at an impingement jet slant angle of 20° for a cylindrical hole.

Yang et al. (2015) performed a numerical analysis for the same arrangement as described in (Takeishi et al. 2010) for a cylindrical hole, a clover-shaped hole and a

compound angled hole and evaluated both effectiveness and heat transfer coefficient. They observed a slight enhancement in heat transfer rate with the swirl. However, a lower heat transfer rate was observed when the swirl was introduced through a compound angle injection. Later, the same swirl generation method was combined with an upstream ramp and the effects were examined experimentally (Yang et al. 2016). This combination proved to be beneficial over the previously studied configurations of swirled film cooling. They obtained improvement in coolant attachment at a ramp angle of 20° and a swirl angle of 30° . A novel method for generating coolant swirl was investigated numerically by modifying the coolant entry into the film hole through the plenum chamber (Jiang et al. 2017). Figure 2.20 shows the modifications of the plenum chamber to induce the coolant swirl. Out of three different chamber configurations studied, the third arrangement was found to increase the effectiveness by 550% for a blowing ratio of 1.5. However, using this configuration, they did not evaluate the swirl intensity of the coolant jet.

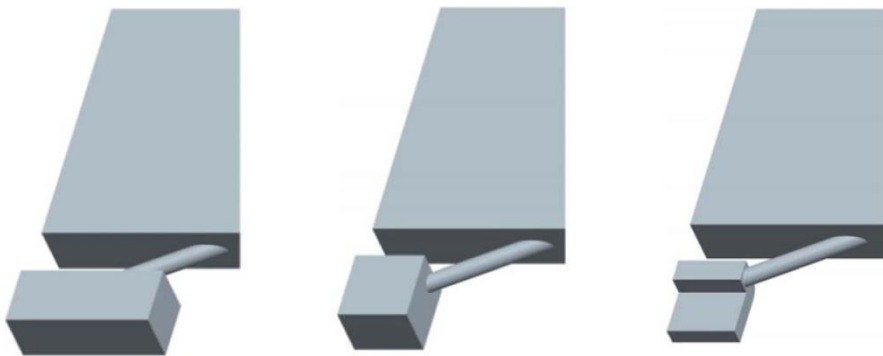


Figure 2.20. Swirl generation by modifying coolant entry into the film hole from the plenum chamber (Jiang et al. 2017).

A recent study conducted an experimental and numerical analysis on a swirled film cooling (Zhu et al. 2022b; a). The swirl was generated from a helical thread made on the internal surface of the coolant supply tube. A thread pitch of two hole diameters was maintained. The swirl effect was studied with a clockwise jet, two jets with opposing directions and multiple holes with a staggered arrangement. They observed nearly 50% higher effectiveness than the conventional holes when the blowing ratio was kept at 1.5. Despite the advantage of swirl, the staggered arrangement showed a detrimental effect.

Each of the above geometrical configurations was analyzed with respect to the conventional cylindrical hole as a base case for comparison. It is observed that the existing geometrical variations provided better cooling performance than the base case. However, some geometries have to face challenges of manufacturability, especially while applying to actual turbine blades. But with the advancement in the manufacturing process, it would be possible to implement such shapes so that the existing cooling capability might enhance. If two different individual configurations prove beneficial, both advantages can be combined for further improvement. Hence attempts were still being made to develop novel concepts of film cooling hole shapes.

2.6 OPTIMIZATION OF FILM COOLING HOLE GEOMETRY

The effect of various parameters on film cooling performance is discussed in previous sections. The effect of an individual parameter can be easily obtained by varying the parameter and observing the film cooling behavior. For example, one can study the effect of blowing ratio on a particular hole shape by measuring or computing η and h at different blowing ratio conditions. On the contrary, it becomes tedious when the effect of different parameters needs to be investigated, such as turbulence intensity, injection angle, hole pitch, and so on. Especially it may require hundreds of cases of data while evaluating optimum parameter values so that the performance of a film cooling configuration can be maximized. It is possible to conduct such an extensive study using computational models, but the computational time requirement would be enormous.

The developments in optimization techniques are being extended to solve various classes of problems. Recently such methods have been utilized to evaluate the optimum film cooling configuration through which the existing blade cooling capability will be enhanced. But the optimization tool needs a mathematical model so that it can evaluate the quantity being maximized at any point in the input parameter space. Again solving a complete three-dimensional RANS model is not feasible. In such situations, surrogate models will be constructed to correlate the input parameters and output variables. Queipo et al. (2005) presented a discussion on the application of

surrogate models in optimizing the variables by taking an example of a liquid rocket injector.

The technique of geometric parameter optimization using surrogate models in film cooling situations was first conducted by Lee and Kim (2009). This method was applied to optimize the coolant injection angle and length of the hole for the cylindrical hole film cooling case. Initially, they conducted three-dimensional numerical simulations for the design space variables, which were generated through a sampling method known as Latin hypercube sampling. A weighted average model is constructed from three different surrogate models: the surface response approximation method, Radial Basis Function Neural Network (RBF) and Kriging model. They used sequential quadratic programming as the search algorithm to obtain the optimized geometry condition. Later this method was extended to a fan-shaped film cooling case where the geometric variables were the inclination angle, hole length and lateral expansion angle (Lee and Kim 2010). They obtained the optimal values as 40.34° , 7.45 times the hole diameter and 21.83° for these variables at a blowing ratio of 0.5. When the same technique was applied to a laidback fan-shaped hole, the additional geometry parameter was the forward expansion angle along with the previous three variables (Lee and Kim 2011). In this study, only the Kriging model was selected as the surrogate model, which is constructed with the spatially averaged effectiveness obtained from RANS simulations for about 35 design variable combinations. Further, by considering aerodynamic loss along with effectiveness as an additional optimizing parameter, Lee et al. (2010) conducted a multi-objective optimization using an evolutionary algorithm.

Choi et al. (2013) followed the previous works and applied them to optimize the parameters of a double jet film cooling case. The geometric parameter optimization for a fan-shaped hole was again conducted by Wang et al. (2016) but using an RBF Neural Network combined with a genetic algorithm. The neural network was trained with 24 testing samples and tested against 15 samples. Lee et al. (2018) attempted to optimize the profile of a Nekomimi-shaped hole by considering the diameter, injection angle of the main and auxiliary holes and the branching angle of the auxiliary holes through the Kriging model with Genetic Algorithm as an optimization method. Moeini and Rajabi Zargarabadi (2018) used a curve fitting

method combined with a genetic algorithm to optimize the fan-shaped hole parameters over a rotating turbine blade profile rotating at 0, 300 and 500 rpm. Though the rotation effect was insignificant, the optimized shape improved the effectiveness by 40% to 50%. Zhang et al. (2019) proposed a multi-fidelity surrogate model for the optimization of the laidback fan-shaped holes. The surrogate model consisted of low-fidelity correlations and high-fidelity RANS simulation results. Similarly, the parameters of a backward injection cylindrical hole were optimized using Taguchi method (Wang et al. 2020).

The application of various surrogate modeling methods and optimization techniques to optimize the existing film cooling parameters has proven to be reliable in enhancing film cooling ability. These methods can be easily implemented to any configuration of film hole and one can obtain the optimized shapes.

2.7 TRANSIENT STUDIES ON FILM COOLING

To evaluate the surface heat flux over a film cooled turbine blade, there is a requirement for two fundamental parameters: the reference temperature of the fluid, T_{ref} , and surface heat transfer coefficient, h . Most of the film cooling studies discussed in the previous sections evaluated these parameters individually through a steady-state analysis. T_{ref} is obtained by measuring the adiabatic surface temperature, while h is calculated from the temperature distribution of the surface having constant heat flux boundary condition. This method of evaluating the heat transfer coefficient has certain limitations, such as maintaining constant heat flux over complex geometries and lateral conduction errors due to longer duration to achieve a steady state. Also, this method of evaluation can provide only one parameter per experiment.

To avoid such difficulties, Vedula and Metzger (1991) proposed a transient technique to estimate h and T_{ref} in case of three temperature convection problems such as film cooling situations. This method is based on solving transient one-dimensional semi-infinite solutions. The transient temperature data of the test surface was obtained for flows with two different coolant temperatures. Hence there will be two equations to evaluate two unknown parameters. Drost et al. (1997) conducted a transient analysis for a flat plate model and turbine aerofoil to determine h and T_{ref} .

They obtained two test data at two different time intervals and applied a regression technique to evaluate the parameters and observed an uncertainty of nearly 10% in estimated heat transfer coefficient values. Later Ekkad et al. (1995) used transient liquid crystal thermography to evaluate film cooling effectiveness and heat transfer coefficient (Ekkad et al. 1997). They conducted two transient tests to determine two parameters. In the first test, both mainstream and coolant were heated; in the second test, only mainstream was heated while the coolant was kept at room temperature. The transient wall temperatures were recorded for up to 80 seconds. They used air and CO₂ as coolant fluids and observed that CO₂ resulted in a lower heat flux than air at a high momentum flux ratio. Ekkad and Han (2000) presented two different methods to evaluate film cooling h and T_{ref} wherein the transient test can be conducted either with heated mainstream or with heated surface technique. The heated mainstream technique is similar to the previous techniques (Ekkad et al. 1995b). In the heated surface technique, only the surface was heated and suddenly exposed to the mainstream, while the transient surface response was recorded. This technique was investigated on internal cooling channels, impingement heat transfer, a flat plate model, turbine blade surfaces and leading edges. However, this method also required two transient tests at varying coolant temperatures. To verify the effect of freestream turbulence intensity on leading-edge film cooling characteristics, Ou and Rivir (2001) used a transient technique. They observed that the turbulence intensity inversely affected the effectiveness but mildly in terms of heat transfer. The heat transfer coefficient in this work was reported in terms of Frossling number, a ratio of Nusselt number to the square root of Reynolds number. Yu et al. (2002) followed previous works and applied those techniques for shaped holes having diffused exits.

A new transient technique by applying non-homogeneous heat flux through heater foil was developed by Vogel et al. (2002). They used nonlinear regression to obtain unknown parameters by conducting multiple tests with different heat flux ratios (Vogel et al. 2003). A major disadvantage of this method is that the applied heat flux influences the thermal boundary layer, which could affect the heat transfer coefficient. To avoid the complexities arising in the measurement of transient temperature through a liquid crystal technique, Ekkad et al. (2004) conducted

experiments using an infrared thermography technique on a single hole leading edge model. The IR technique allowed the authors to estimate both of the parameters from a single transient test by measuring wall temperature at two different instances. In an attempt to find the recovery temperature along with h and T_{ref} in the case of transonic turbine cascade, Xue et al. (2015) proposed a dual linear regression technique. However, this work followed the two-test strategy similar to the method used in the case of liquid crystal experiments. A novel method of estimating adiabatic temperature and heat transfer coefficient was proposed by Cho et al. (2016) based on the maximum likelihood estimation technique. They used a one-dimensional Fourier equation and stated that the method could be used in situations similar to film cooling and for surfaces satisfying the semi-infinite assumption. Recently, Ekkad and Singh (2021) presented a comprehensive review of the methodologies adopted in various literature to evaluate the unknown film cooling parameters.

It has been observed that the previous studies followed two or multiple test methods to obtain film cooling parameters. One major drawback of such techniques is the difficulty in maintaining the same aerodynamic conditions when different boundary conditions are applied. Hence, it is essential to develop a method that can determine both h and T_{ref} from a single transient test. A few works have discussed this aspect and proposed approaches for simultaneous estimation. However, in these works, the data reduction technique is either complicated or not discussed thoroughly. It was observed that solutions to such problems could also be obtained using the inverse heat transfer approach.

The inverse heat conduction problems (IHCP) in heat transfer are related to estimating the unknown parameters such as boundary conditions, initial conditions, or the thermophysical properties using transient temperature measurements (Ozisik et al. 2002). When the boundary conditions at a surface are known, it is possible to find the temperature distribution on a surface. This technique is known as the direct problem. On the other hand, in the case of inverse problems, the boundary conditions are estimated by measuring the temperature-time history (Beck et al. 1985). The difficulty in the case of IHCPs is that the solution is ill-posed. Hence the solution to IHCPs is very sensitive to the errors in the measurements. Different methods have been

proposed for the solution of IHCPs, such as Tikhonov's regularization technique, Beck's function estimation, optimization technique, Genetic algorithm, etc. Inverse solutions are majorly classified as stochastic and gradient-based methods (Beck and Arnold 1977). Stochastic methods can find the global minimum but are complicated to implement and require too many iterations to converge, which increases the computational time required for the parameter estimation. Contrarily, the gradient-based methods are faster in convergence and simple to implement, but they are likely to end up at a local minimum (Ozisik 2018). Another difficulty associated with the gradient-based method is calculating the sensitivity coefficients accurately when the inverse problem is nonlinear. But these methods are computationally inexpensive and their implementation to a different class of problems is much easier.

The solution to inverse problems can be obtained by initially defining an objective function that is constructed by the squared difference between the measured temperature values and the values obtained by solving the forward solution. The unknown parameters existing in the objective function are then estimated iteratively through a minimization process. Out of various minimization algorithms, the most widely used methods are Newton's method, the steepest descent method, the Levenberg-Marquardt algorithm and the conjugate gradient method (Colaço et al. 2006).

Levenberg-Marquardt Algorithm (LMA) is one of the most straightforward yet robust method used for solving inverse heat conduction problems based on the minimization of the objective function (Pujol 2007). It is a gradient-based method that combines the steepest descent method in the neighborhood of the initial guess and uses the Gauss-Newton method near the minimum of the ordinary least squares norm. This method was initially proposed by Levenberg (1944) and further developed by Marquardt (1963). LMA was successfully applied to a variety of situations related to inverse heat conduction problems to estimate thermophysical properties and boundary conditions (Duda and Konieczny 2022; Montazeri et al. 2021; Tahmasbi and Noori 2020). Even the most modern technologies, such as neural networks, use LMA as a training algorithm (Deveci et al. 2018).

2.8 SUMMARY OF THE LITERATURE SURVEY AND RESEARCH GAPS

By going through the literature is observed that, out of various flow parameters, blowing ratio plays a significant role in deciding the coolant adherence over the surface. Beyond a specific limit, coolant jet lift-off becomes a major issue of concern. But, change in geometric parameters such as hole shape and injection angle may allow additional coolant mass flow rate at higher blowing ratios. When various parameters are involved in deciding the film cooling behavior, conducting experiments for each and every combination of these parameters could become extremely tedious. A computational study can replace the experimental efforts and helps in understanding flow behavior in such a complicated phenomena.

A significant amount of computational studies were carried out in the literature. Majorly it can be categorized into two groups. One group belong to the exploration on film cooling flow behavior in terms of coolant-mainstream interaction and the root causes for flow detachment from the surface. In the second group, the film cooling studies were concentrated on developing non-conventional hole shapes using numerical simulations which can reduce coolant jet lift-off and enhance the cooling efficiency.

From the literature review, it has been observed that coolant swirl can also impact on the film cooling behavior and the studies pertaining to this parameter is limited. The existing methods for swirl generation have used more or less complex mechanisms and the swirl was generated before the coolant entry into the film hole. Though the internal cooling mechanisms used in modern turbine blades induce a swirl into the coolant flow, a systematic control of the swirl strength would provide a desired coolant swirl at the hole exit. Past studies have proven that the application of a swirl to a coolant flow can substantially enhance film cooling performance. The coolant swirl counteracts the effect of CRVP and reduces jet lift-off at higher blowing ratios.

Similar to the steady state evaluation of film cooling parameters, a transient analysis could also be used to determine the effectiveness and heat transfer coefficient with a short duration experiments. A significant advantage of a transient study is that it

can replace the two-test strategy of steady-state analysis. However, transient study pertaining to film cooling is very limited in the literature. A major difficulty was to measure the transient surface temperature data and a suitable data reduction technique which is mathematically simple and easy to implement. The existing transient studies have also followed the two-test method due to difficulties associated with the data reduction technique. Hence, developing a data reduction technique for the transient analysis of film cooling situations using a single test approach can be beneficial.

Following are the few research gaps observed after the literature review.

1. Since there is significant amount of swirl exists in the coolant flow due to internal cooling channel construction in turbine blades, it is necessary to consider the effect of swirl in the film cooling performance evaluation.
2. Also, there is a need to develop a method which can control the coolant swirl and use it to enhance the heat transfer capability.
3. It would also be useful to study if other geometrical parameters influence the coolant distribution along with the presence of coolant swirl.
4. Since the existing transient methodologies are based on two-test strategy, it is required to study on a data reduction technique which can evaluate film cooling parameters from a single test.

2.9 OBJECTIVES OF THE PRESENT WORK

The main aim of the present thesis is to study and explore an innovative concept of film cooling through computational fluid dynamics over a flat surface. The main requirement of the proposed modification is that it would alter the coolant flow characteristics and helps in enhancing the film cooling protection. Film cooling effectiveness and heat transfer coefficient are investigated as the performance parameters. Instead of obtaining these two parameters separately, a single transient measurement can provide information on both parameters. To achieve the aforementioned aims, the following objectives are attempted in the present work,

- To study the film cooling performance of swirled film cooling generated using a twisted tape inserted inside the film hole.

- To explore the effect of different parameters such as coolant swirl intensity, injection angle and hole length on film cooling performance.
- To maximize the effectiveness of the new film cooling configuration by optimizing its geometrical variables.
- To develop a simple data reduction technique to simultaneously evaluate film cooling effectiveness and heat transfer coefficient using an inverse heat transfer solution approach.

2.10 CLOSURE

This chapter furnished a brief review of essential studies undertaken in the past. Studies pertaining to the effect of the coolant hole exit profile on the film cooling characteristics were explored. Recent developments in the area of film cooling are examined to identify the research gap. Applications of advanced techniques to optimize the current film cooling designs were investigated and the literature regarding transient studies on film cooling is presented. The chapter is closed by specifying the motivation behind the present work and thesis objectives. [Equation Chapter \(Next\) Section 1](#)

CHAPTER 3

NUMERICAL MODELING

3.1 GEOMETRY OF THE COMPUTATIONAL DOMAIN

A three-dimensional computational domain for numerical simulation is created for film cooling arrangement. The computational domain contains a mainstream, a coolant hole and a plenum chamber. The computational geometry is shown in Figure 3.1, created similarly to the experimental conditions of Takeishi et al. (2010). The geometry contains a single film hole inclined at 30° from the wall surface towards the mainstream flow direction with a diameter (d) of 5mm. Other dimensions of the computational domain are non-dimensionalized using film cooling hole diameter, as shown in Figure 3.1. The origin of the coordinate system is located on the trailing edge of the film hole exit having x -direction along the wall, y -coordinate normal to the wall and z -coordinate representing lateral direction. The film cooling hole is located at $190d$ from the inlet so that the boundary layer approaching the coolant jet will be fully turbulent. The computational domain is extended to $50d$ downstream of the film hole. The width of the film cooled wall is made $5d$ each on lateral sides ($\pm z$) from the center plane of symmetry over the circular hole. The domain is extended $20d$ in the direction normal to the wall surface.

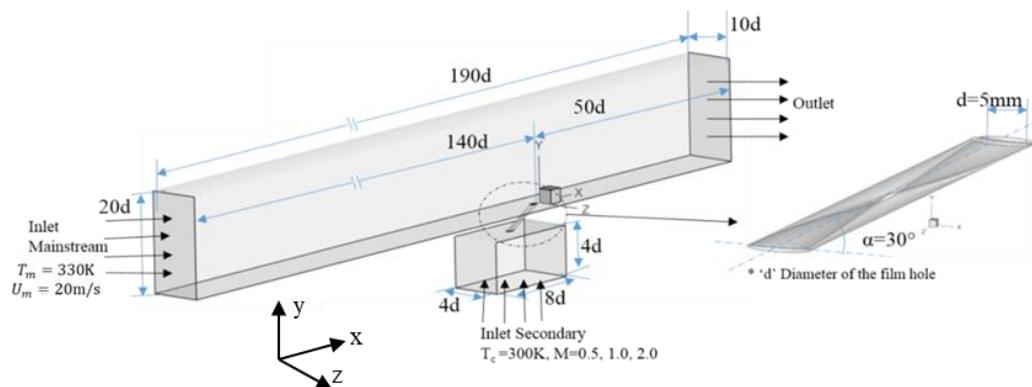


Figure 3.1. Three-dimensional view of the computational domain used for the numerical simulation.

The coolant has to pass through the film cooling hole of length $40d$ before coming out of the hole, which is equal to the plate thickness used in the case of experiments. Coolant is introduced into the hole through a plenum chamber having a height (y -direction) and width of $4d$ (z -direction) and a length of $8d$ (x -direction). Supplying coolant through the plenum chamber provides a much more realistic boundary condition than making a direct entry of the coolant at the inlet of the hole. Hence a coolant supply plenum is constructed at the film hole entrance.

In this work, a cylindrical hole is initially used to simulate the film cooling behavior, which is similar to the work reported by Takeishi et al. (2013). This particular case of film cooling is considered as the base case. Further modifications are made to the base geometrical profile to accomplish the novel concept of film cooling design.

The proposed design of the film cooling hole configuration consists of a twisted tape insert inside the hole. The twisted tape imparts tangential and radial velocity components to the coolant resulting in the generation of swirled flow at the exit of the hole. A two-dimensional view of the twisted tape arrangement inside a pipe is shown in Figure 3.2. Twisted tapes are mainly characterized by a geometrical feature known as pitch. The pitch is defined as the distance between two locations in the axial direction on a twisted surface corresponding to 180° rotation of the twisted tape. Since the twisted tape is inserted inside a cylindrical hole, its width is equal to the diameter of the hole. The additional velocity components of the coolant exiting through the film hole can be controlled by varying the pitch of the tape. This result in a coolant flow having different strengths of swirl, which is denoted by a term called swirl number.

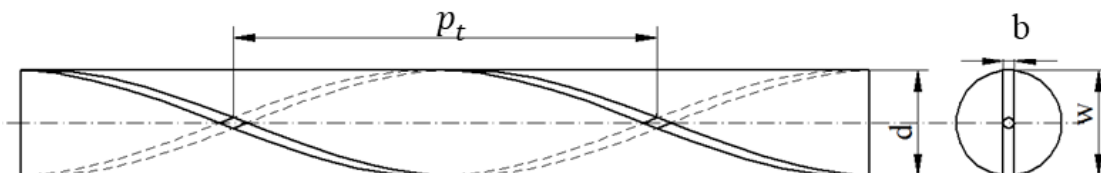


Figure 3.2. Geometrical aspects of a twisted tape insert inside a cylinder.

The intensity swirl is characterized by a non-dimensional number known as swirl number S , which is defined as the ratio of the axial flux of angular momentum to the axial flux of axial momentum (Gupta et al. 1984).

$$S = \frac{2G_\theta}{dG_x} = \frac{2 \int_0^R \rho U_x U_\theta r^2 dr}{d \int_0^R \rho U_x^2 r dr} \quad (3.1)$$

where U_x and U are the axial and tangential velocity components and r is the radial distance from the center of the cylindrical film hole.

The desired swirl number for the coolant jet can be achieved by changing the pitch of the twisted tape. The swirl number in case of flow through circular pipes having a twisted tape can be calculated in terms of twist ratio (TR) (Kumar et al. 2017) as given by Equation 3.2.

$$S = \frac{\pi}{2TR} \quad (3.2)$$

The twist ratio is a non-dimensional number defined as the ratio of the pitch of the twisted tape to the width of the tape.

$$TR = \frac{p_t}{w} \quad (3.3)$$

The following assumptions were made while arriving at Equation 3.2 from Equation 3.1.

- a) The fluid is incompressible.
- b) The average axial velocity of the fluid is constant across any two sections of the pipe having a twisted tape insert.
- c) The internal rotation of the fluid elements is negligible; hence the rotation of the fluid can be viewed as a solid body rotation.
- d) From the third assumption, it can be assumed that the tangential velocity of the fluid is constant throughout the film hole.
- e) When the fluid element makes tangential displacement of 2π radians, it travels a distance of p in the axial direction.

In the work of Takeishi et al. (2010), film cooling characteristics for coolant flow having three different swirl numbers of 0.0289, 0.116 and 0.168 were studied.

Hence in the present study, the twisted tape insert inside the film hole is generated having a pitch that can produce the same swirl numbers as that of Takeishi et al. (2010). Table 3.1 gives the values of pitch and twist ratios of the twisted tape insert corresponding to the required swirl numbers. Further, a parametric study is carried out by varying the swirl number, inclination angle and length of the hole. Table 3.2 provides the details of the geometrical variables studied during the parametric study.

Table 3.1 Swirl numbers and corresponding pitch for the twisted tape insert during the initial study.

Sl. No.	S	TR	p_t (mm)
1	0.0289	54.35	271.75
2	0.116	13.54	67.7
3	0.168	9.35	46.75

Table 3.2. Various geometrical parameters examined in the present study.

Geometrical Parameters	Values
Film hole diameter, d	5 mm
Coolant swirl number, S	0, 0.2, 0.4, 0.6, 0.7
Inclination angle of the film hole, α	15°, 30°, 45°, 60°, 90°
Hole length to diameter ratio, L/d	4, 8, 12, 16

3.2 NUMERICAL MESH

Figure 3.3 shows the computational domain which is discretized using unstructured tetrahedral elements for the numerical simulation. The numerical grid generation is achieved using ANSYS Meshing modular. Fine mesh elements are created over the film hole domain as well as over the wall surface, where the possibility of high gradients might occur. The element sizes were controlled by specifying edge and surface mesh control options. A general growth rate of 1.15 is provided to coarsen the elements in the regions of less significance. A very fine mesh is created in the wall normal direction to capture the effect of the boundary layer using inflation layers. Around 30 inflation layers are provided, having its first layer

located at a distance of around 10^{-2} mm from the wall. This result in a y^+ value of less than 1.

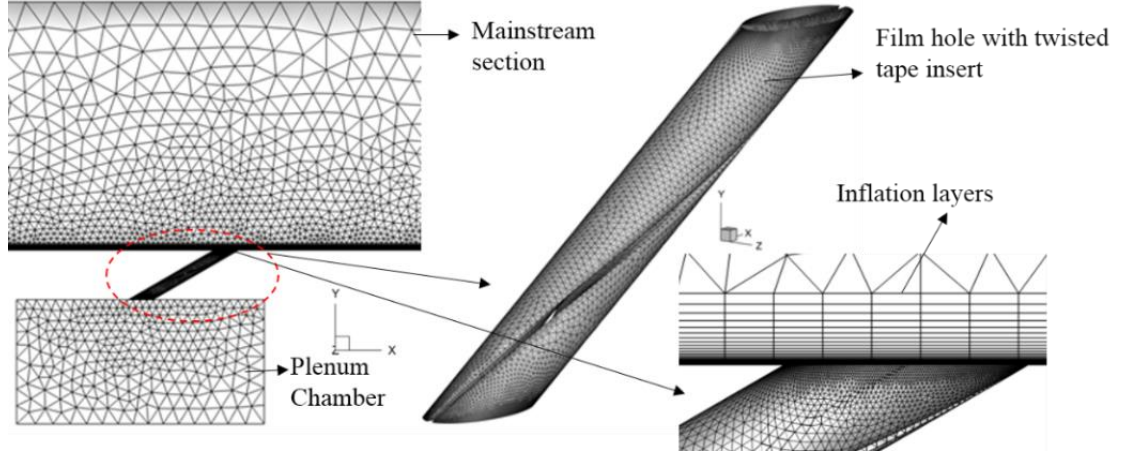


Figure 3.3. Computational mesh highlighting the film hole region with twisted tape insert.

3.3 GOVERNING EQUATIONS

The present numerical simulation solves for three-dimensional governing equations for the conservation of mass, momentum and energy within a finite control volume. Equation 3.4 and 3.5 represents the Navier-Stokes equations and Equation 3.6 represents the energy equation in tensor form.

Continuity equation:

$$\frac{\partial(\rho U_i)}{\partial x_i} = 0 \quad (3.4)$$

Momentum equation:

$$\frac{\partial(\rho U_i U_j)}{\partial x_j} = -\frac{\partial P}{\partial x_j} + \frac{\partial}{\partial x_j} \left[\mu \left(\frac{\partial U_i}{\partial x_j} + \frac{\partial U_j}{\partial x_i} \right) - \rho \overline{u'_i u'_j} \right] \quad (3.5)$$

Energy equation:

$$\frac{\partial(\rho U_j T)}{\partial x_j} = \frac{\partial}{\partial x_j} \left[\frac{\mu}{Pr} \left(\frac{\partial T}{\partial x_j} \right) - \rho \overline{T' u'_j} \right] \quad (3.6)$$

where i, j, k are the directional indices.

These equations are solved under the following assumptions

- i. The operating fluid is air
- ii. All the equations are solved for steady state
- iii. Air is considered as incompressible ideal gas
- iv. The density of air is assumed to vary only with respect to temperature.

The film cooling flow situation is highly complex due to the interaction of two fluid streams generating a complicated turbulent shear layer and boundary layer flows. In order to capture the instantaneous fluctuations existing in the turbulent flow, the variables in the Navier-Stokes equations and energy equation are decomposed using the Reynolds time averaging technique. The time averaging leads to additional unknown quantities known as Reynolds stress (represented by the last term in Equation 3.5) and turbulent heat flux (represented by the last term in Equation 3.6) which are modeled using the Boussinesq hypothesis as given in Equations 3.7 and 3.8.

$$-\overline{\rho u'_i u'_j} = \mu_t \left(\frac{\partial U_i}{\partial x_j} + \frac{\partial U_j}{\partial x_i} \right) - \frac{2}{3} \rho k \delta_{ij} = \tau_{ij} \quad (3.7)$$

$$-\overline{\rho \theta' u'_j} = \frac{\mu_t}{Pr_t} \left(\frac{\partial T}{\partial x_j} \right) \quad (3.8)$$

The term μ_t , in Equations 3.7 and 3.8, is known as turbulent viscosity, which is calculated by solving additional transport equations for turbulent kinetic energy (k) and dissipation rate (ε) or specific dissipation rate (ω). Various turbulence models were proposed to solve the unknown turbulence quantities. Shear Stress Transport (SST) $k - \omega$ model is one of the turbulence models which combines the characteristics of both $k - \varepsilon$ and $k - \omega$. In this model, the turbulent boundary layer is resolved using $k - \omega$ model, and the free-stream flow is predicted by $k - \varepsilon$ model. A blending function combines the models that solve for appropriate transport variables in the near wall region and far field.

3.3.1 The SST $k - \omega$ turbulence model

The transport equations of SST $k - \omega$ turbulence model are as follows (ANSYS Inc. 2014),

$$\frac{\partial(\rho k U_i)}{\partial x_i} = \tau_{ij} \frac{\partial U_i}{\partial x_j} - \rho \beta^* k \omega + \frac{\partial}{\partial x_j} \left[\left(\mu + \frac{\mu_t}{\sigma_k} \right) \frac{\partial k}{\partial x_j} \right] \quad (3.9)$$

$$\begin{aligned} \frac{\partial(\rho\omega U_i)}{\partial x_i} &= \frac{\alpha}{\nu_t} \tau_{ij} \frac{\partial U_i}{\partial x_j} - \rho\beta\omega^2 + \frac{\partial}{\partial x_j} \left[\left(\mu + \frac{\mu_t}{\sigma_\omega} \right) \frac{\partial \omega}{\partial x_j} \right] \\ &+ 2\rho(1-F_1) \frac{1}{\omega\sigma_{\omega,2}} \frac{\partial k}{\partial x_j} \frac{\partial \omega}{\partial x_j} \end{aligned} \quad (3.10)$$

The blending function, F_1 is computed as,

$$\begin{aligned} F_1 &= \tanh \left\{ \min \left[\max \left(\frac{\sqrt{k}}{0.09\omega y}, \frac{500\mu}{\rho y^2 \omega} \right), \frac{4\rho k}{\sigma_{\omega,2} D_\omega^+ y^2} \right] \right\}^4 \\ D_\omega^+ &= \max \left(2\rho \frac{1}{\sigma_{\omega,2}\omega} \frac{\partial k}{\partial x_j} \frac{\partial \omega}{\partial x_j}, 10^{-10} \right) \end{aligned} \quad (3.11)$$

The turbulent viscosity, μ_t is calculated from Equation 3.12 as,

$$\mu_t = \frac{\rho k}{\omega} \frac{1}{\max \left(\frac{1}{\alpha^*}, \frac{SF_2}{a_1\omega} \right)} \quad (3.12)$$

Where S is the magnitude of strain rate tensor defined as,

$$S = \sqrt{2S_{ij}S_{ij}}, \text{ where } S_{ij} = \frac{1}{2} \left(\frac{\partial u_j}{\partial x_i} + \frac{\partial u_i}{\partial x_j} \right) \quad (3.13)$$

The second blending function, F_2 , will be determined by,

$$F_2 = \tanh \left[\max \left(\frac{2\sqrt{k}}{0.09\omega y}, \frac{500\mu}{\rho y^2 \omega} \right) \right]^2 \quad (3.14)$$

The terms in Equation 3.9 and 3.10 are computed as follows,

$$\beta = 0.075F_1 + 0.0828(1-F_1) \quad (3.15)$$

$$\sigma_k = \frac{1}{F_1/\sigma_{k,1} + (1-F_1)/\sigma_{k,2}} \quad (3.16)$$

$$\alpha^* = \left(\frac{0.024 + (\rho k/6\mu\omega)}{1 + (\rho k/6\mu\omega)} \right) \quad (3.17)$$

$$\sigma_\omega = \frac{1}{F_1/\sigma_{\omega,1} + (1-F_1)/\sigma_{\omega,2}} \quad (3.18)$$

The model constants are,

$$\sigma_{k,1} = 1.1746, \sigma_{k,2} = 1.0, \sigma_{\omega,1} = 2.0, \sigma_{\omega,2} = 1.168, \alpha_1 = 0.31, \beta^* = 0.09, a_1 = 0.31$$

3.4 BOUNDARY CONDITIONS

The boundary conditions applied during the numerical simulation are given in Table 3.3, which are analogous to the experimental conditions. The mainstream domain consists of an inlet and outlet boundary, a wall surface and open boundaries on the lateral and top sides. At the inlet boundary of the mainstream domain, as shown in Figure 3.1, the free-stream flow is supplied with a uniform velocity of 20 m/s and a uniform temperature profile of 330K. The static pressure at the outlet boundary is prescribed with a 1atm. The top surface and the lateral sides of the domain are mentioned with a symmetry boundary condition, which can avoid any interference with the flow from lateral and top surfaces by making the gradients of velocity and temperature zero in the direction normal to the boundary. The film cooling hole surface and the top and longitudinal sides of the plenum chamber are specified as adiabatic walls with no-slip boundary conditions. The lateral boundaries of the plenum are mentioned with a symmetry boundary condition similar to the mainstream.

The coolant flow is introduced through an inlet boundary located at the bottom of the plenum chamber with a specific mass flow rate and a temperature of 300K. The coolant mass flow rate is calculated through the required blowing ratio at the exit of the film hole, as mentioned in Table 3.3. Along with these boundary conditions, a turbulence intensity of 0.36% is provided to maintain similarity with the experimental conditions.

Table 3.3. Film cooling parameters used in the present study.

Parameters	Values
Mainstream velocity, U_m	20 m/s
Mainstream Temperature, T_m	330 K
Blowing ratio, M	0.5, 1.0, 1.5 and 2.0
Coolant inlet temperature, T_c	300 K
Turbulence intensity	0.36%

In the present study, the surface heat transfer characteristics of film cooling are analyzed from the adiabatic film cooling effectiveness and the surface heat transfer coefficient. While evaluating effectiveness, the film cooled wall is made adiabatic by specifying zero heat flux on the surface. Later, the same wall is subjected to a heat flux of 1000 W/m^2 to evaluate the heat transfer coefficient.

3.4.1 Numerical set-up

All numerical simulations are carried out in a commercial CFD solver ANSYS Fluent V16 based on a finite volume approach. A three-dimensional steady-state numerical solution is obtained for an incompressible turbulent flow. The material property of the computational domain is made up of air having ideal gas properties. The density of air is made to change as a function of temperature using the equation of state for an ideal gas. This maintains the necessary density ratio between the mainstream and the coolant. The relationship between velocity and pressure correction is accomplished using the SIMPLE algorithm. The momentum and energy fluxes over the cell faces are computed using a second-order upwind interpolation scheme. For other quantities, such as turbulent scalars, first-order upwind interpolation is used for spatial discretization.

Each numerical solution took approximately 20 hours on a 12-core parallel processing workstation. The convergence criteria for the residuals of mass and momentum are set to the order of 10^{-5} , and for the energy 10^{-7} and 10^{-4} for turbulence scalars.

3.5 GRID INDEPENDENCE STUDY

The numerical results are needed to be independent of the grid resolution used in the study. Unstructured tetrahedral elements are generated for the base case of film cooling to perform the grid independence study. Element sizes on the edge of the film cooling hole at the hole exit and on the downstream wall surface are varied to obtain various refinement levels of the mesh. Four sets of grid refinements are tested, having the number of elements of around 1, 1.5, 2.2, 3.5 and 4 million. Figure 3.4 shows the effectiveness obtained for different mesh resolutions for film cooling having no

twisted tape arrangement. It can be seen that all mesh arrangements more or less produced similar results. A slight deviation was observed in the far downstream region when $x/d > 20$. This could be due to insufficient element sizes which are required to capture the exact temperature gradients existing in the region of coolant-mainstream interaction. The error may increase due to larger element sizes along downstream leading to slight overprediction of the effectiveness.

When the mesh is created for the case of film cooling with a twisted tape insert, the element sizes in the downstream region of the film hole are kept same as that of the base case. Element sizes on the edge profiles of the twisted tape are given similar to the edge sizing mentioned in the base case.

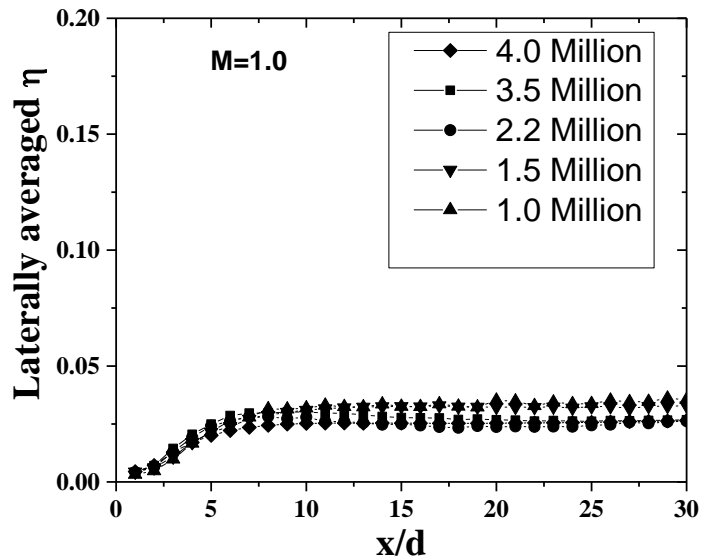


Figure 3.4. Verification of grid independent solution for the numerical simulations.

3.6 EVALUATION OF TURBULENCE MODELS

The fidelity of turbulence models in predicting numerical results are evaluated using four different turbulence models for the base case. Laterally averaged effectiveness is computed using SST $k - \omega$, Std. $k - \epsilon$, Realizable $k - \epsilon$ and RNG $k - \epsilon$ turbulence models at $M = 1.0$. Figure 3.5 shows the computed effectiveness using these turbulence models, which are compared with the experimental result.

From the figure, it can be deduced that the effectiveness predicted by SST $k - \omega$ turbulence model closely follows the experimental trend. However, beyond

$x/d = 20$, the deviation is predominant. Meanwhile, other turbulence models tend to over predict the effectiveness earlier than SST $k - \omega$, where the deviation starts from $x/d \approx 10$. Only in the region $x/d \approx 3$ to 10, the $k - \varepsilon$ based turbulence models gave better prediction than SST $k - \omega$.

While looking at the coolant distribution on the center plane ($x - y$), the $k - \varepsilon$ based turbulence models did not predict the coolant jet lift-off which predominantly occurs in the immediate downstream of coolant exit through the hole. This creates accumulation of more coolant concentration over the surface leading to overprediction of $\bar{\eta}$. On the other hand, the SST $k - \omega$ model has predicted the initial jet separation to some extent resulting in closer agreement with the measurements. One major reason observed for such deviation between the turbulence models is that the eddy viscosity computed inside the film hole was higher for $k - \varepsilon$ versions than SST $k - \omega$ model.

Previous studies also observed and reported that the prediction accuracy of the SST $k - \omega$ turbulence model is higher than other variants of eddy viscosity based models (Yang et al., 2015 and Jiang et al., 2017). The average error value for the SST $k - \omega$ turbulence model is found to be around 20%, while other models produced an error of more than 40%. Hence all further numerical calculations are conducted using the SST $k - \omega$ turbulence model.

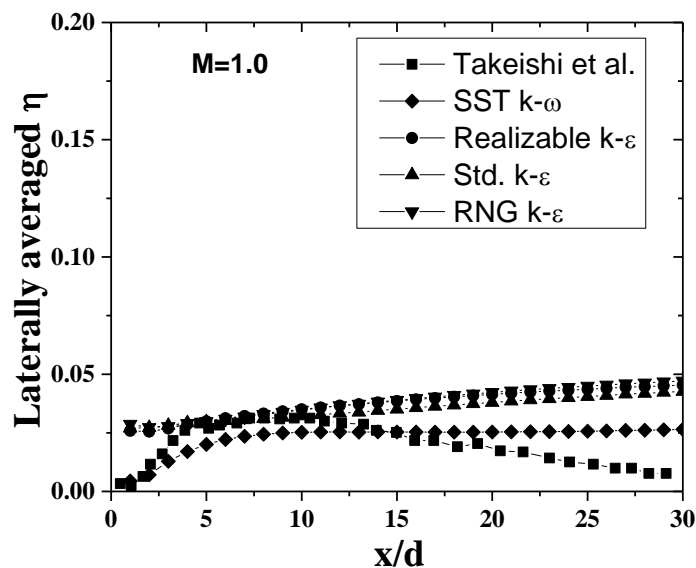


Figure 3.5. Performance evaluation of turbulence models.

3.7 VALIDATION

Validation of the present numerical result is carried out by considering the experimental data of Takeishi et al. (2010) for a cylindrical hole film cooling without a twisted tape insert. Figure 3.6 compares the laterally averaged effectiveness for $M = 0.5$ and 1.0 obtained from the present numerical simulation with the experimental results. $\bar{\eta}$ obtained using LES by Oda et al. (2011) is also shown in the figure for comparison. It is clear from the figure that the present numerical simulation produced a reasonably accurate prediction of effectiveness. For the case of $M = 1.0$, an average deviation of around 0.5% is observed from the experimental data for $x/d < 20$.

Computed effectiveness distribution is in good agreement with the experimental results up to $x/d \approx 10$ for $M = 0.5$ and $x/d \approx 15$ for $M = 1.0$ than LES. The overprediction of $\bar{\eta}$ in LES is reported due to underestimation of turbulent mixing near the region of film hole exit which failed to predict the flow separation and reattachment phenomena. Additionally, for the LES, the turbulence statistics and time-mean velocity components in the region upstream of the film hole exit are computed by RANS simulation with realizable $k - \varepsilon$ turbulence model.

In the far downstream ($x/d > 15$), the present numerical results as well as LES results have deviated from the experimental results and the effectiveness values are overpredicted. Such overprediction occurs due to more coolant accumulation near the wall as a result of underprediction of the coolant diffusion in the lateral direction. The primary source for this disparity is attributed to the isotropic eddy viscosity assumption used in predicting turbulence quantities in case of RANS simulations. As it can be observed for LES at $M = 0.5$ that the downstream prediction is better than the present simulation. However, at $M = 1.0$, when compared with the results of LES, present numerical results are more accurate in predicting the film cooling behavior. This could be due to the suppressed jet lift-off phenomena in LES leading to more coolant concentration in the far downstream. As far as the present simulation is concerned, the jet detachment is fairly captured resulting in closer agreement with respect to experimental observations.

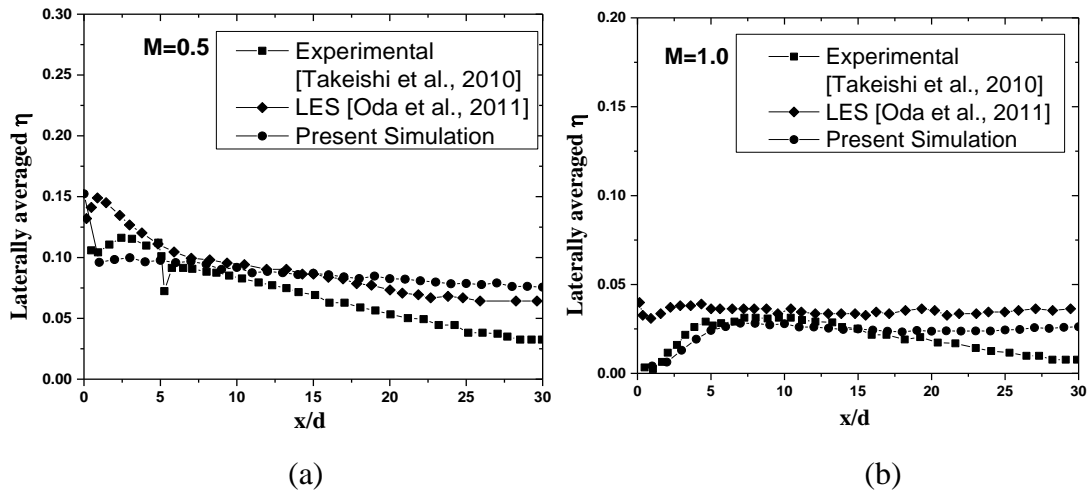


Figure 3.6. Comparison of the present numerical results with the experiments for (a) $M = 0.5$ and (b) $M = 1.0$.

3.8 CLOSURE

In the present chapter, details of the geometrical configurations are provided for a base case of film cooling and for the proposed concept of film cooling. The proposed hole shape has a twisted tape inserted inside the film hole, which generates coolant swirl. Concepts such as swirl number and twist ratio are introduced. Also, details regarding the grid generation technique and the numerical procedure adopted in the simulation are explained. Further, the numerical results are verified against the possible grid sensitivity of the solution. A detailed study on the effect of turbulence models such as SST $k - \omega$, Std. $k - \varepsilon$, Realizable $k - \varepsilon$ and RNG $k - \varepsilon$ on the accuracy of effectiveness estimation is evaluated. In the last part, the present numerical results are validated by comparing them with experimental results obtained from the literature.

Equation Chapter (Next) Section 1

CHAPTER 4

EFFECT OF COOLANT SWIRL ON FILM COOLING BEHAVIOR

4.1 INTRODUCTION

The effect of introducing a twisted tape on the coolant flow path inside the film cooling hole is analyzed in this chapter. The twisted tape insert imparts a swirl to the coolant flow while exiting through the hole. At first, numerical simulation is carried out for the base case comprising a simple cylindrical hole film cooling without a twisted tape insert. Later simulations have been performed for film cooling with a twisted tape insert. The base case is considered as a reference to compare the results of swirled film cooling with the twisted tape insert.

As discussed in the previous chapter, the coolant is issued with different swirl strengths, denoted in terms of swirl number (S). Initially, three swirl numbers, such as $S = 0.0289, 0.116$ and 0.168 are investigated since the experimental work of Takeishi et al. (2010) used the same swirl numbers. Further, the swirl numbers are varied from 0.2 to 0.7 to study the effect of the swirl number on film cooling behavior and performance. Finally, a parametric study is performed to study the influence of injection angle and film cooling hole length-to-diameter ratio on film cooling performance in the presence of a twisted tape insert.

In the experiments of Takeishi et al. (2010) on swirled coolant flow, swirl numbers of 0, 0.0289, 0.116 and 0.168 were studied. Hence our preliminary analyses are conducted at the same swirl numbers. Since the mechanism used to generate coolant swirl in the present study is entirely different from the method used in Takeishi et al. (2010), a direct comparison of the results are not provided.

4.2 EFFECTIVENESS

Laterally averaged effectiveness evaluated for $M = 0.5, 1.0, 1.5$ and 2.0 having swirl numbers of 0, 0.0289, 0.116 and 0.168 shown in Figure 4.1. The base case has

zero coolant swirl ($S = 0$) representing film cooling with no twisted tape insert. A clear observation is that $\bar{\eta}$ increases with swirl number for all blowing ratios studied in the present work except for the case of $M = 0.5$ and $S = 0.0289$ which shows less $\bar{\eta}$ values than the base case. This particular behavior could be due to mixing phenomena between the coolant and mainstream when the swirl is imposed. At low blowing ratio, the coolant jet is less likely to penetrate even in the absence of swirl ($S = 0$). However, addition of a small amount of swirl would increase the mixing rate. Meanwhile, at high swirl numbers ($M = 0.5, S = 0.168$), higher mixing rate might get compensated by higher lateral diffusion of the coolant, causing an improvement in the effectiveness compared to the base case.

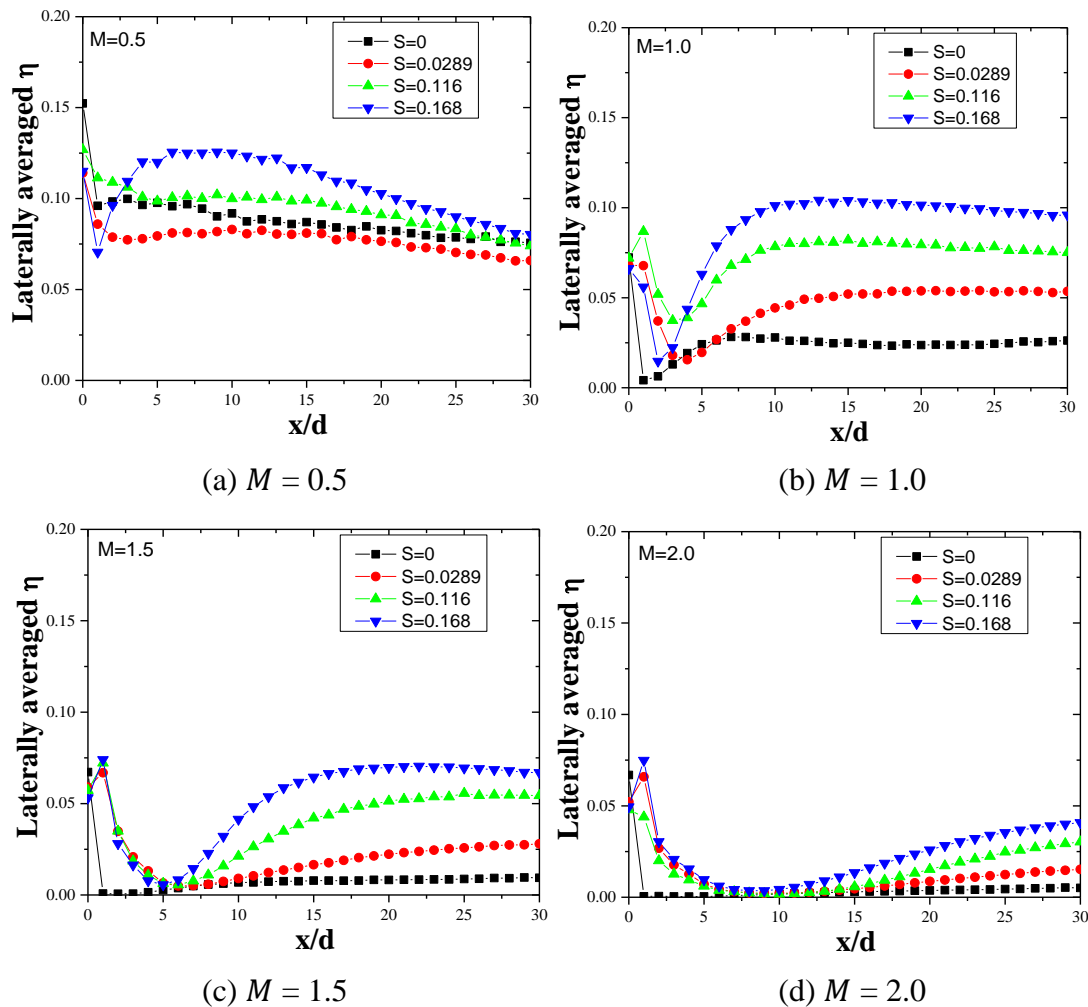


Figure 4.1. Laterally averaged effectiveness for different blowing ratios and swirl numbers along the downstream direction of film hole.

A sudden drop in the values of $\bar{\eta}$ immediately after the hole exit, is by virtue of coolant jet momentum trying to penetrate through the mainstream. Meanwhile, the cross-flow imparts a pressure gradient across the jet, deflecting it towards the wall. As the coolant jet travels downstream, it reattaches over the wall leading to better protection. The point where minimum occurs seems to move along x direction with the blowing ratio. The average increase in the effectiveness values for $S = 0.168$ are about 20%, 290% and 1500% for $M = 0.5, 1.0$ and 2.0 , respectively when compared with the base case.

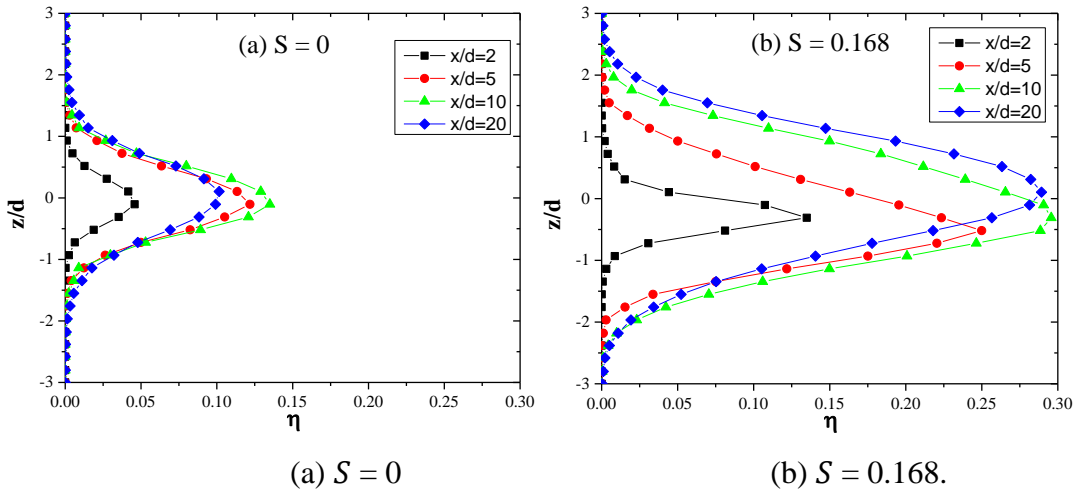


Figure 4.2. Lateral effectiveness distribution at downstream locations of the film hole.

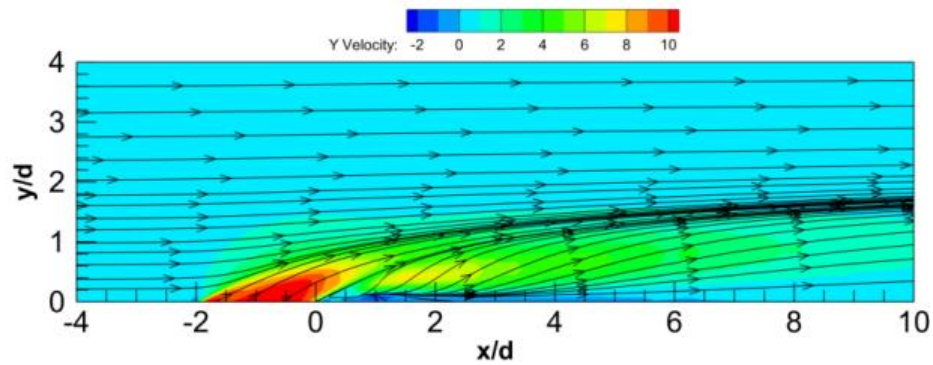
Modifications to the coolant distribution over the flat surface due to the presence of swirl will be examined through the lateral dispersion of the coolant stream. Figure 4.2 illustrates the effectiveness distributed laterally for a non-swirl case (Figure 4.2(a)) and swirl case with swirl number of 0.168 (Figure 4.2(b)) at a few selected x/d 's for $M = 1.0$. Two important observations can be perceived by comparing the results of the two cases. The first observation is the peak effectiveness values which occur at the centerline at $z/d = 0$. The centerline effectiveness for swirl case has been enhanced to almost double that of a non-swirled case. Secondly, the lateral dispersion of the coolant is also improved by the swirled jet than in the zero swirl case. It should be noted that the η distribution at $x/d = 20$ for $S = 0$ is less than at $x/d = 5$ and 10 whereas for $S = 0.168$ it is almost equal for $x/d = 10$ and 20. This is basically due to the diffusion of a majority of the coolant lump while the jet is

detached from the wall and the coolant concentration becomes weak when it reaches $x/d = 20$. The swirled flow might have reduced the coolant mixing by keeping the jet close to the wall, which could lead to achieving higher η values at $x/d = 20$ for $S = 0.168$ than the $S = 0$ case. A trivial observation demonstrates that a symmetrical lateral distribution of η towards the $z/d = 0$ plane has now become asymmetrical with the imposition of swirl. The centerline η values are slightly moved towards $-z$ direction for $S = 0.168$ case.

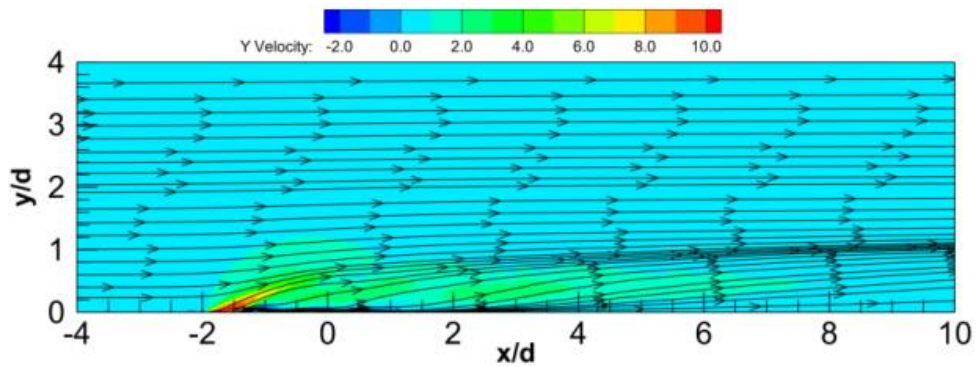
4.3 FLOW STRUCTURE

The flow structures for swirled and non-swirled cases are shown in Figure 4.3 to Figure 4.5 with the help of streamlines and contour plots. When a coolant jet emanates out of a film hole, it tends to bend in the free stream direction due to the static pressure exerted by the cross flow. Non-swirled jet possesses a higher y –velocity component at the hole exit (Figure 4.3(a)), which may lead to jet penetration and separation from the wall. The streamlines are getting squeezed from all sides, accelerating the jet even further. Swirled flow, on the other hand, has a lower y –velocity component due to twist insertion, as observed from Figure 4.3(b) and tends to bend easily towards the cross-flow, making them less likely to penetrate through the mainstream. When looking at the top view (Figure 4.4(a)), wake vortices will form on the leeward side of the coolant jet when $S = 0$ because of the pressure gradient across the jet. Eventually, these vortices aid in to the z –velocity component leading to less lateral spreading. The twisted tape insert would not allow the formation of wake vortices behind the jet causing smaller z –velocity components (Figure 4.4(b)) and subsequently helping the jet to spread laterally.

When the coolant jet exists from the film hole, there will be a formation of counter-rotating vortex pair (CRVP) due to shear between the mainstream and the coolant jet. CRVP constitutes two vortices rotating in opposite directions in a plane perpendicular to the mainstream, which travels downstream. CRVP is the major source for jet lift-off and detachment from the wall. It will augment the coolant-mainstream interaction and enhances the mixing by driving the mainstream towards the coolant jet core from lateral sides.

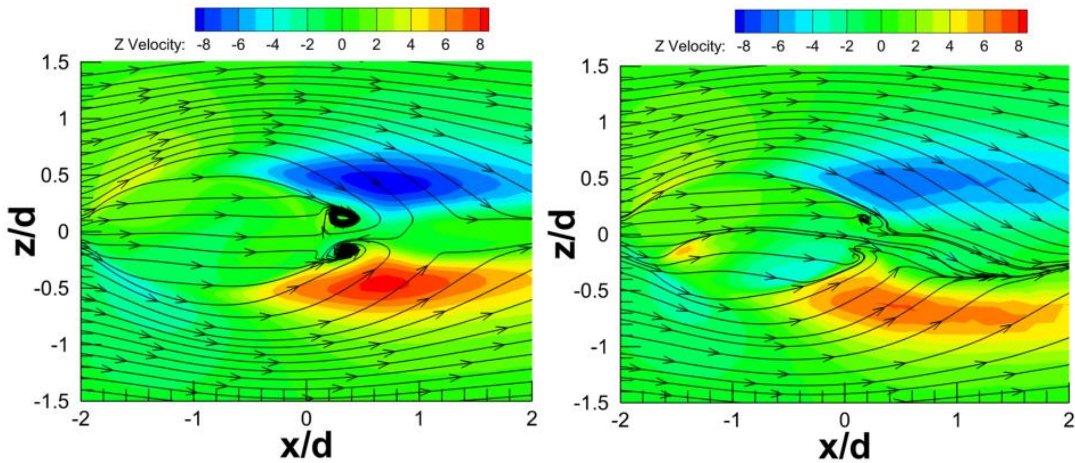


(a) $S = 0$



(b) $S = 0.168$.

Figure 4.3. Streamlines on $x - y$ plane at $z/d = 0$ with $y -$ velocity contour.



(a) $S = 0$

(b) $S = 0.168$.

Figure 4.4. Streamlines on $x - z$ plane at $y/d = 0.05$ with $z -$ velocity contour.

In the non-swirling case, as shown in Figure 4.5(a), the CRVP is symmetrical about the center plane (at $z/d = 0$) which will suck the mainstream fluid from the lateral sides and push towards the center plane of symmetry. At the central plane, low temperature coolant will be driven away in the y -direction resulting in coolant jet lift-

off from the wall. As the jet travels downstream, the center of vortices starts moving away from each other in z –direction and also moves towards $+y$ –direction. Coolant jet mixing with the mainstream increases the jet temperature and reduces the cooling effectiveness over the surface. Further increase in blowing ratio increases the jet penetration height due to a higher momentum of the coolant jet. The temperature profile takes the form of a kidney shape due to the effect of CRVP.

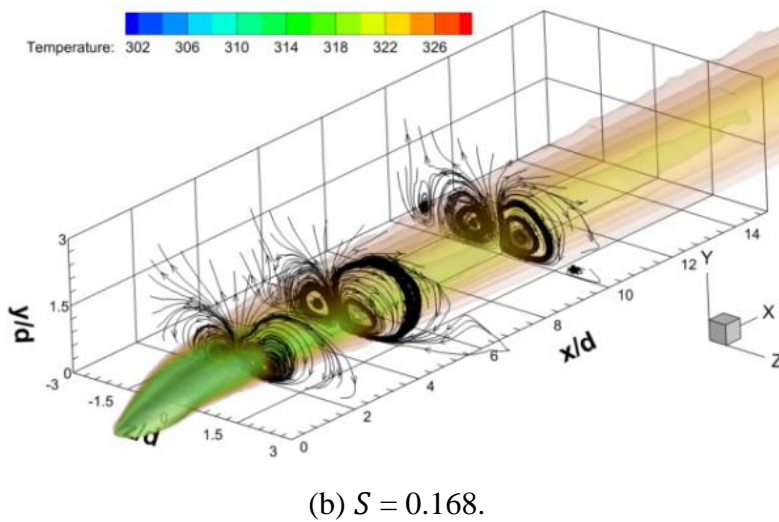
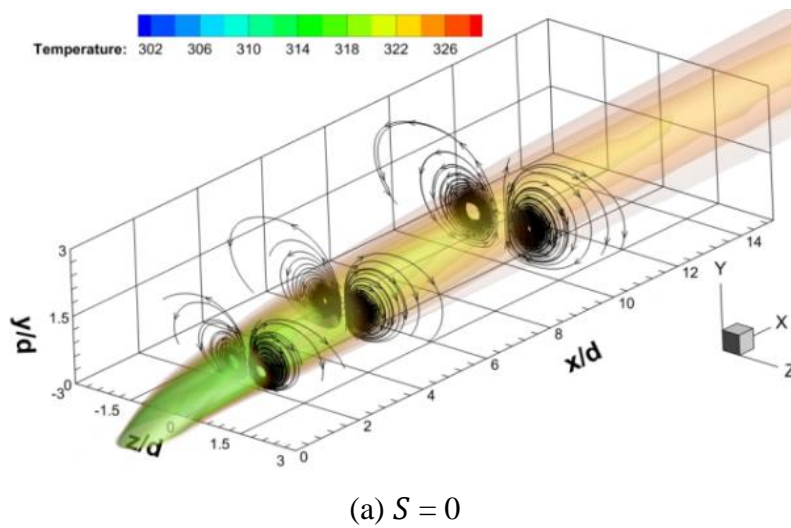


Figure 4.5. Three-dimensional iso-contours of temperature along with streamlines on $y - z$ plane at $x/d = 2, 5$ and 10 .

Inserting a twisted tape inside the film hole divides the coolant jet into two lobes of different sizes, one smaller than the other. The induced swirl yields an asymmetrical CRVP structure, as shown in Figure 4.5(b), in which two vortices will have different strengths of rotation. Reduced vortex interaction at the center plane

($z/d = 0$) keeps the jet closer to the wall. The vortex on one side of the center plane tries to push the coolant away from the wall; meanwhile, the other vortex pushes the coolant in the lateral direction and helps in better coolant spreading. It can also be observed from Figure 4.5(b) that there is a formation of a secondary vortex downstream at $x/d = 10$ (for $S = 0.168$), which might further suppress the strength of the main vortex and aid in better spreading. A noticeable fact is that the vortex height from the wall has dramatically reduced compared with the non-swirling case, which helps keep the coolant jet closer to the wall. These features contribute towards retaining a lower wall temperature and better protection against hot gases.

4.4 JET TRAJECTORY

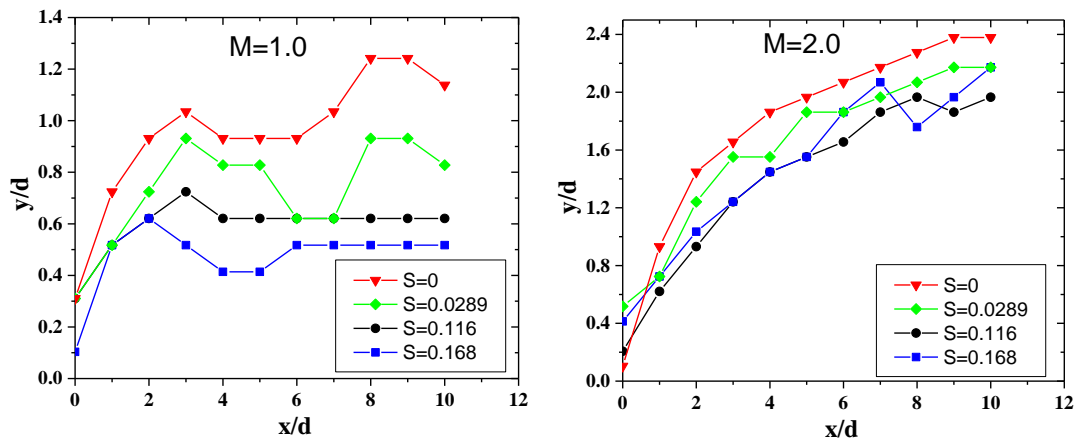


Figure 4.6. Comparison of observed jet trajectory for different swirl numbers.

The extent of coolant jet penetration into the mainstream will be characterized by calculating the jet trajectory. Different methods have been followed in the literature to estimate the jet trajectory (Mahesh 2013). In the present work, the jet trajectory is calculated by finding the minimum value of the local scalar concentration in $x - y$ plane at $z/d = 0$. The jet trajectories for different swirl numbers are plotted in Figure 4.6 for blowing ratios of 1.0 and 2.0. It is obvious that with the increase in blowing ratio (from $M = 1.0$ to $M = 2.0$), there will be deeper jet penetration. But the advantage of having a swirled flow over a non-swirled case can be observed by the reduction in jet penetration height. Compared to non-swirled flow, the swirled flow ($S = 0.168$) has reduced the penetration height by up to 48% and 22% for $M = 1.0$ and 2.0, respectively. At a higher blowing ratio ($M = 2.0$), the penetration height does not

seem to reduce beyond a certain limit with an increase in swirl number. This could be due to the higher jet momentum dominating the swirl effect.

4.5 EFFECT OF TWISTED TAPE THICKNESS

The numerical simulations so far have been conducted by considering twisted tape at a thickness (b) of 0.5mm. However, it is essential to study the influence of twisted tape thickness on the coolant distribution. Hence a parametric study is conducted by considering the twisted tapes having a thickness of 0.5mm, 0.25mm and 0.1mm. There is no particular reason behind selecting these three values. But a thick tape might offer more resistance for the coolant flow through the film hole and increase pressure drop across the hole. Hence a maximum thickness of $0.1d$ and a minimum value of $0.02d$ are considered. Laterally averaged effectiveness evaluated at $S = 0.168$ and $M = 1.0$ for these three thickness cases are shown in Figure 4.7. No significant variation is observed in the computed $\bar{\eta}$ within the range of thickness studied. Only for the case of $b = 0.1\text{mm}$, a slight deviation in the value of $\bar{\eta}$ for $x/d < 3$ and $x/d > 15$ with an increase of around 7% is observed. Here, in these cases, as the thickness of the tape increased, there exists sufficient gap between the two parts of the coolant flow. So, a small amount of coolant flows through the gap and occupy over the wall immediately upon exit. For thin twisted tape, this loss does not exist and hence more coolant is available in the downstream which improves effectiveness.

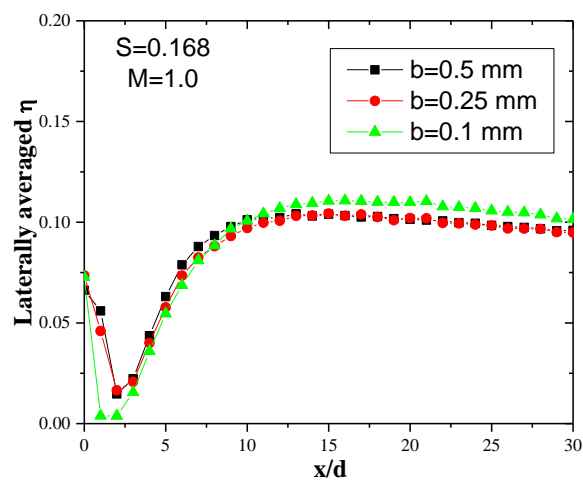


Figure 4.7. Twisted tape thickness effect on the laterally averaged effectiveness.

4.6 COEFFICIENT OF DISCHARGE

Inserting twisted tape could require additional pumping power to eject the coolant through the hole. Discharge coefficient (C_d) illustrate the pressure losses occurring through the film hole and it is defined as the ratio of actual mass flow rate (\dot{m}_c) to the theoretical mass flow rate. The theoretical mass flow rate can be obtained by measuring the pressure losses occurring between the inlet (p_c) and exit (p_∞) of the film hole. The discharge coefficient can be calculated as,

$$C_d = \frac{\dot{m}_c}{\frac{\pi d^2}{4} \sqrt{2\rho_c(p_c - p_\infty)}} \quad (4.1)$$

Figure 4.8 shows the discharge coefficient obtained using Equation (4.1) for different blowing ratios and swirl numbers. It appears that the value of C_d has reduced approximately 7% - 11% for swirled flow cases than non-swirled flows. This is the direct consequence of increased frictional losses inside the film hole due to the presence of twisted tape. The twisted tape necessitates additional pumping power to inject the coolant. But the twist ratio does not appear to affect C_d , since the length of the twisted tape is the same for all three swirl numbers. It is recommended that one has to optimize the blowing ratio and the pumping power to obtain maximum efficiency.

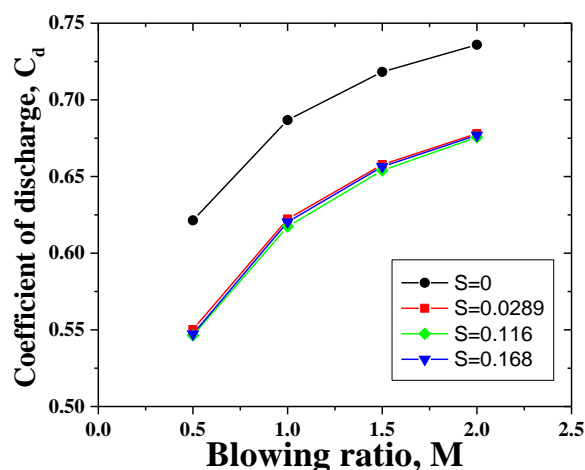


Figure 4.8. Discharge coefficient for the case of with and without twisted tape insert.

4.7 TWISTED TAPE ALIGNMENT INSIDE THE FILM HOLE

The coolant flow inside the film hole gets divided into two parts due to the twisted tape insert, as shown in Figure 4.9. When the twisted tape edge is in-line with the mainstream, the two halves of the coolant stream at the exit lay side by side laterally and such configuration is referred to as in-line twist (Figure 4.9(a)). On the other hand, out of the two halves of the coolant stream, one half ejects from the leading edge side and the other half comes out from the trailing edge (Figure 4.9(b)). Such configuration is achieved by giving a 90° phase angle to the twisted tape with in-line arrangement and is referred to as 90° twist in the present study.

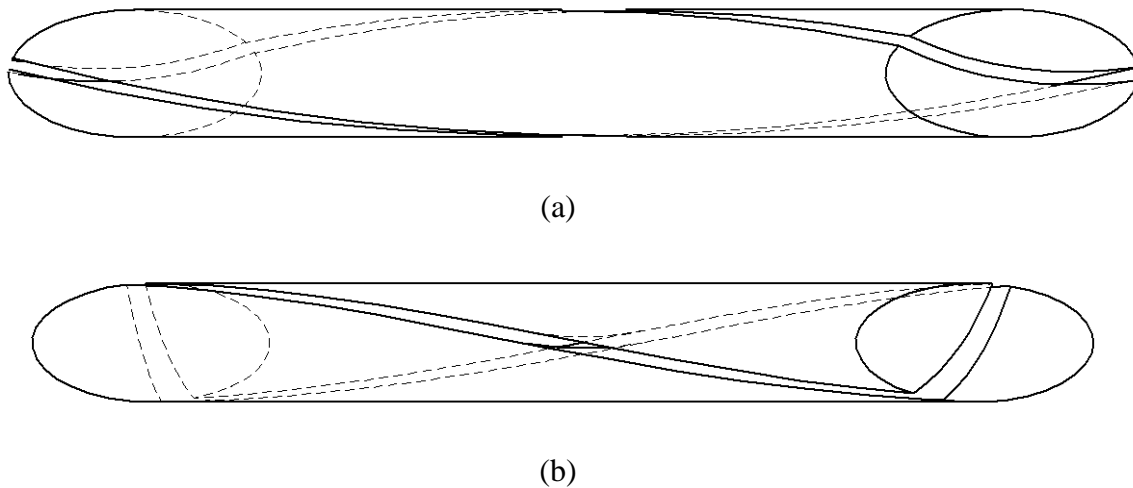
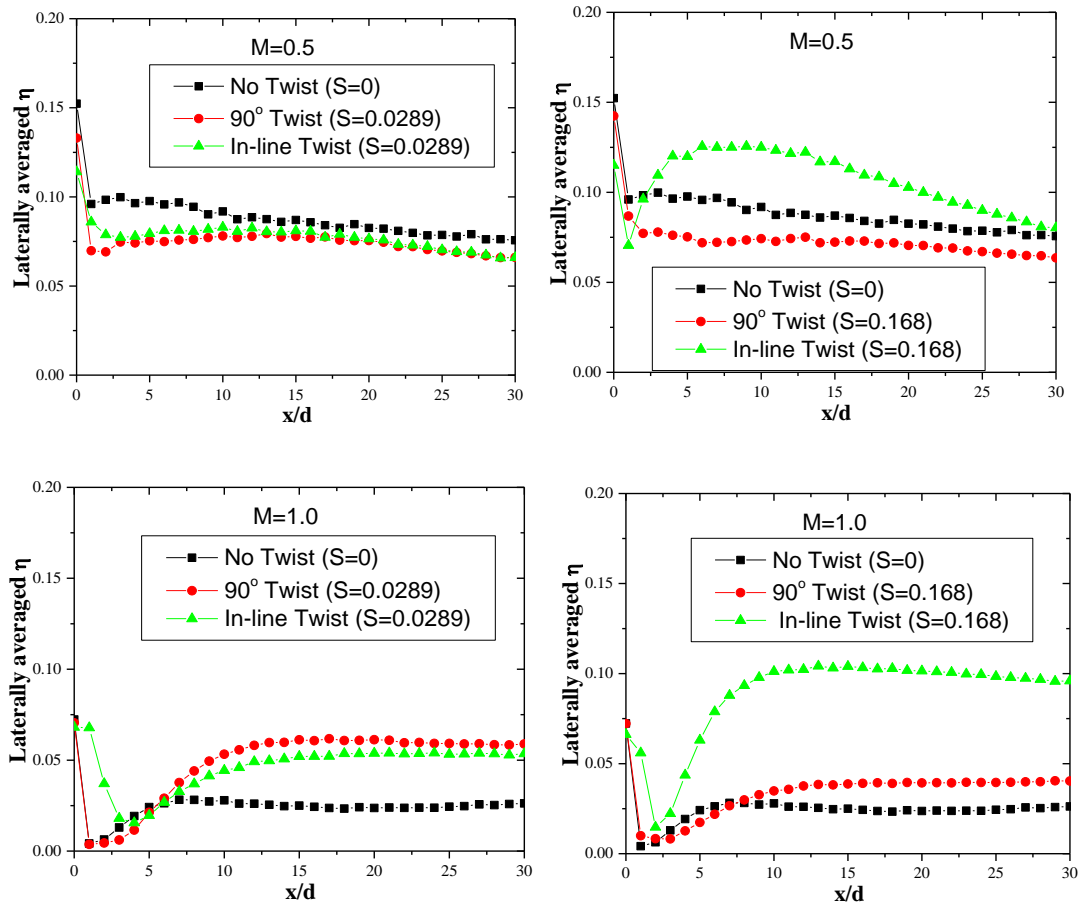


Figure 4.9. Arrangement of twisted tapes (a) In-line twist (b) 90° twist.

Figure 4.10 compares the $\bar{\eta}$ obtained for non-swirl case ($S = 0$) and swirl cases of $S = 0.0289$ and 0.168 for $M = 0.5, 1.0$ and 2.0 having twisted tape with 0° and 90° phase angle with respect to mainstream. It can be noticed that there is no significant improvement in the laterally averaged effectiveness for the case of twisted tape insert at 90° phase difference with respect to the mainstream. At a low swirl number ($S = 0.0289$) both phase angles of the twist produced similar results. With higher swirl numbers, the twist with 90° phase angle shows a slight improvement, whereas the case with inline arrangement significantly improved the effectiveness. To understand the exact reason behind such differences in the results, the velocity profiles at the hole exit are studied and it is discussed below.

If we observe the y –velocity components at the exit of the hole, as shown in Figure 4.11, the mainstream approaching the jet gets blocked by the windward part of the jet for a 90° twist. Meanwhile, the y –velocity component on the leeward side could penetrate the mainstream easily and thereby promoting jet lift-off from the wall. The z –velocity components are also higher for the twist with a 90° phase angle, causing more coolant mainstream mixing than the in-line arrangement. Consequently, the effectiveness observed in case of in-line twist arrangement resulted in higher η values than the case of twist with 90° phase angle.



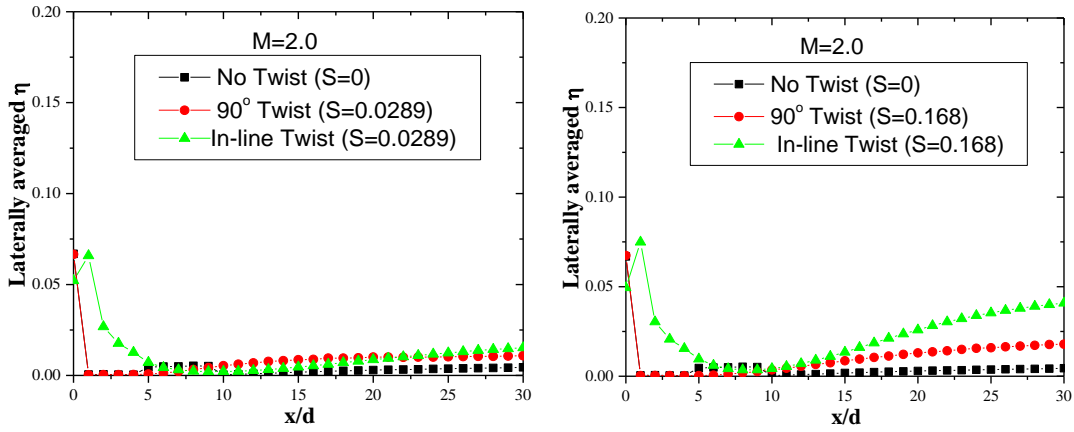
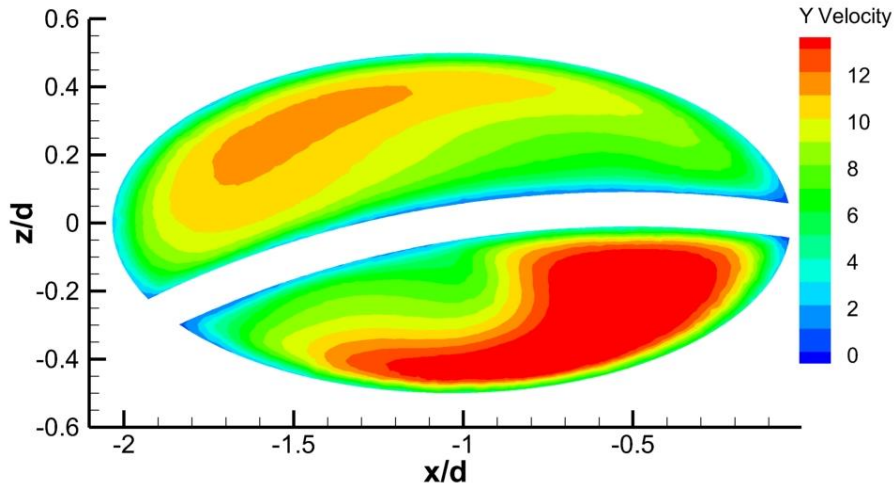
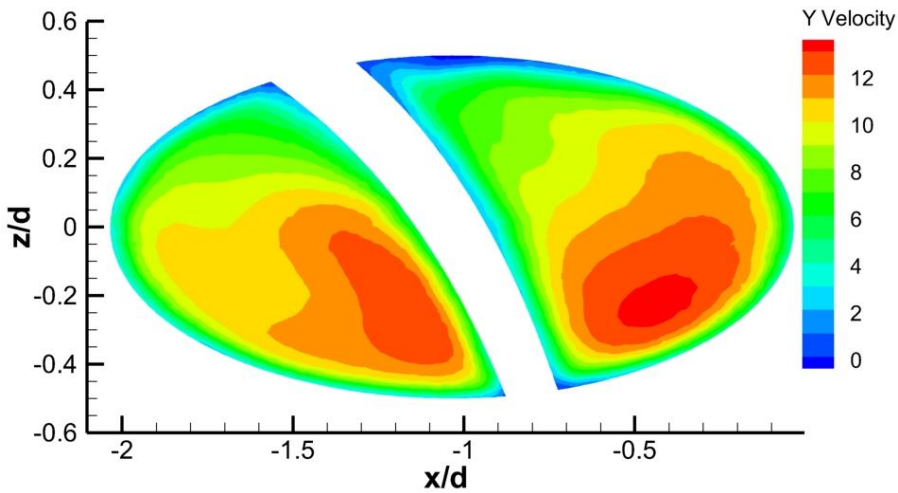


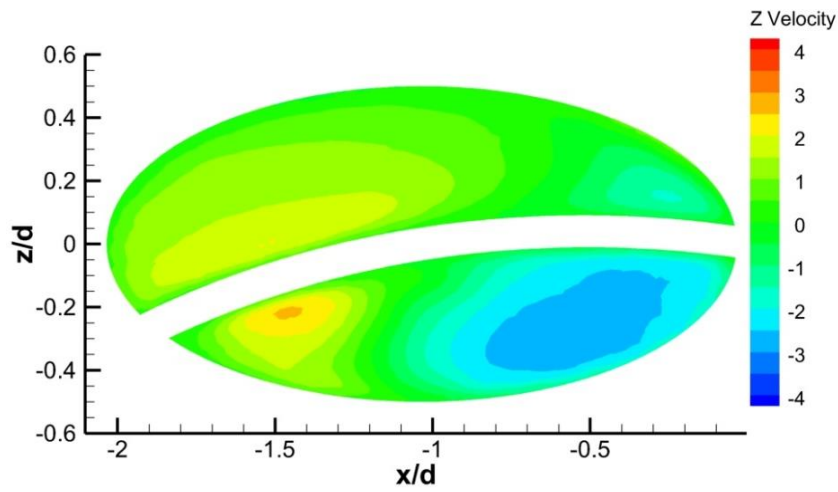
Figure 4.10. Comparison of laterally averaged effectiveness for twisted tape insert being in-line and 90° out of phase with respect to mainstream for different M and S .



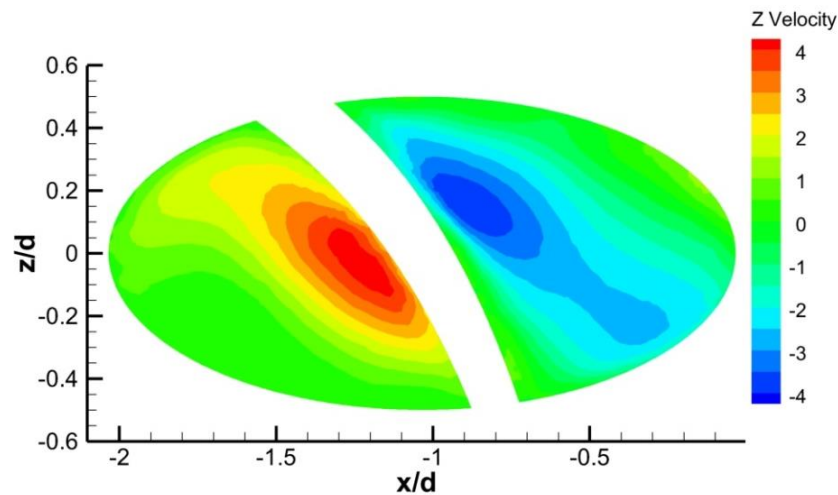
(a) y –velocity for in-line twisted tape insert case.



(b) y –velocity for twist with 90° phase angle.



(c) z –velocity for in-line twisted tape insert case.



(d) z –velocity for twist with 90° phase angle.

Figure 4.11. Comparison of y and z velocity at the exit of film hole for twist insert being in-line and 90° out of phase cases.

Figure 4.12 compares coolant distribution over $x - y$ and $x - z$ planes along with streamlines for an in-line and 90° twisted tape arrangement. It can be seen from the figure that the coolant in case of in-line twisted tape insert is deviated more towards the wall as soon as it comes out of the hole. The streamlines are less deviated from the wall and are more evenly spread on the XY plane. While in case of 90° twisted tape insert, the coolant stream appears to be less disturbed by the mainstream since the coolant concentration is gradually decreasing along the length and also elongated penetration in y -direction. In this case, the streamlines appears to be steadily moving away from the wall and are more concentrated at the edge of the

shear layer. Hence, the in-line twisted tape insert produces better coolant distribution than the 90° twisted tape insert leading to improved effectiveness.

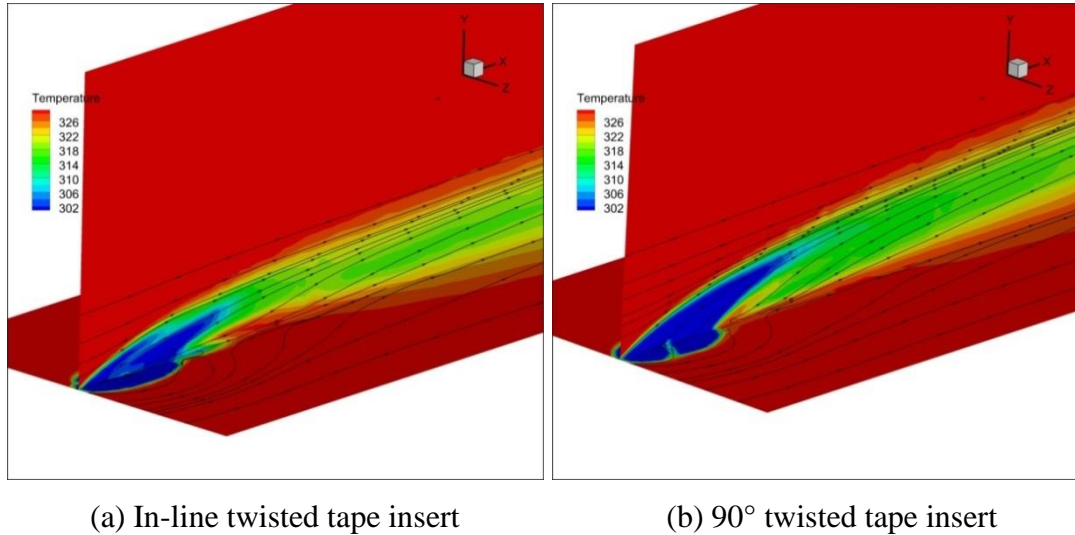


Figure 4.12. Comparison of coolant distribution using temperature contour and streamlines for $M = 1.0$ and $S = 0.168$.

4.8 HEAT TRANSFER COEFFICIENT RATIO (h/h_0)

Analyzing the performance of film cooling requires heat transfer distribution over the surface along with effectiveness values. The heat transfer coefficient in case of film cooling is normalized using the flat plate heat transfer coefficient without the film cooling. Figure 4.13 shows the normalized laterally averaged heat transfer coefficient for $M = 0.5$ to 2.0.

It is evident from Figure 4.13 that the effect of blowing ratio on heat transfer is substantial. Low blowing ratio ($M \leq 1.0$) has a positive effect by keeping h/h_0 below 1.0 on account of the additional coolant mass flux injected into the boundary layer, which reduces the heat transferred to the surface. A higher blowing ratio enhances the heat transfer rate by amplifying the local turbulence levels due to injected coolant. Addition of swirl to the coolant flow further adds up to the mean turbulence level of the mainstream and affect the heat transfer rate more than a non-swirl case. except for blowing ratio of 0.5. Since the flow is predominantly attached throughout the length for $M < 1.0$, the disturbances due to swirl would eventually decay by wall shear stress. At $M = 1.0$, the HTC seems to increase with S in the near

downstream region and becomes more or less equal in the far downstream. At high blowing ratios ($M > 1.0$), the heat transfer coefficient values are similar for all swirl numbers adjacent to the hole exit. This could be due to the mixing phenomena which occurs away from the wall due to jet penetration and less disturbed flow near the wall. But along the downstream, there is almost more than 6% ($S = 0.168$) increase in HTC at $S = 0.168$ than a typical non-swirl case. It can be concluded that the blowing ratio of 1.0 with $S = 0.168$ can produce highest effectiveness as well as it can keep HTC to be almost as equal to no-swirl film cooling situation. In this particular case, a reduction in heat transfer coefficient of up to 1.6% can be observed for $M = 1.0$ with $S = 0.168$ in the far downstream region. A possible explanation for such behavior could be due to the reattached coolant jet which helped in reducing the wall temperature in that region of the flow.

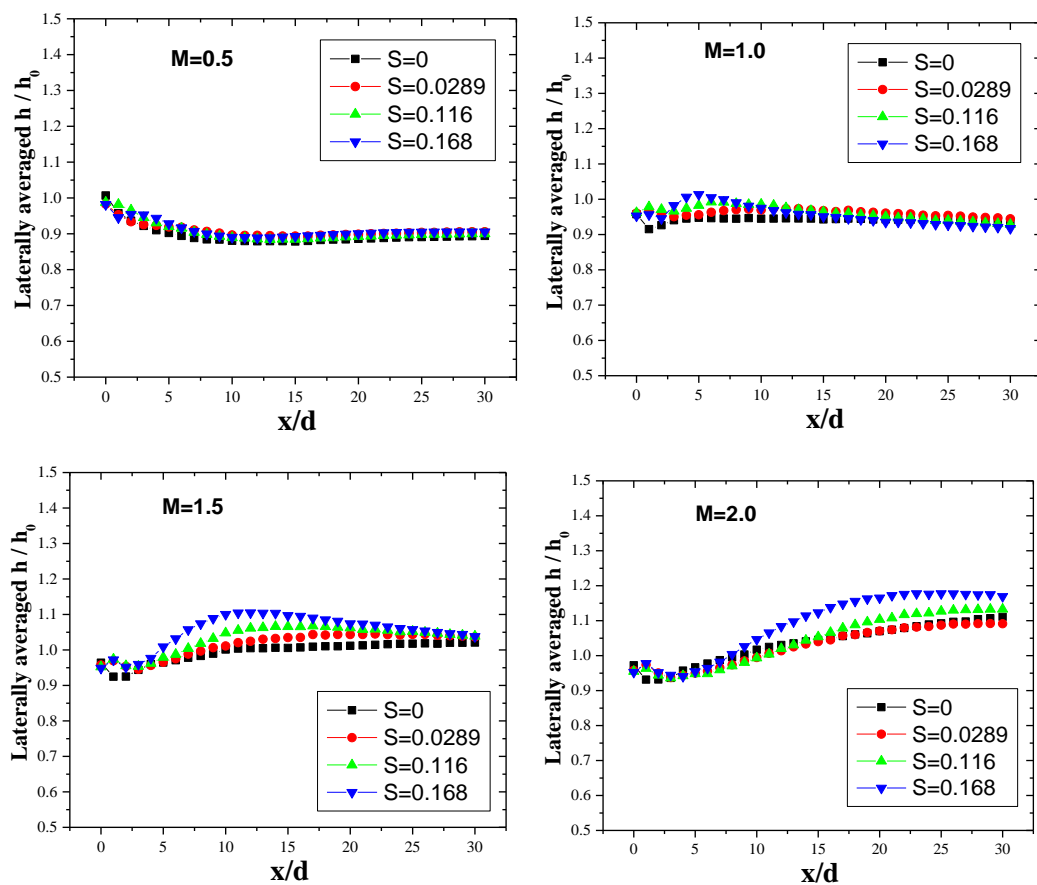


Figure 4.13. Heat transfer coefficient in downstream of the film hole for different swirl numbers and blowing ratios.

4.9 NET HEAT FLUX REDUCTION

To know the combined effect of effectiveness and heat transfer coefficient in any new film cooling design requires calculation of net heat flux reduction (NHFR) over the surface. A positive NHFR denotes that the film cooling configuration is favorable, whereas a negative NHFR indicates a detrimental effect.

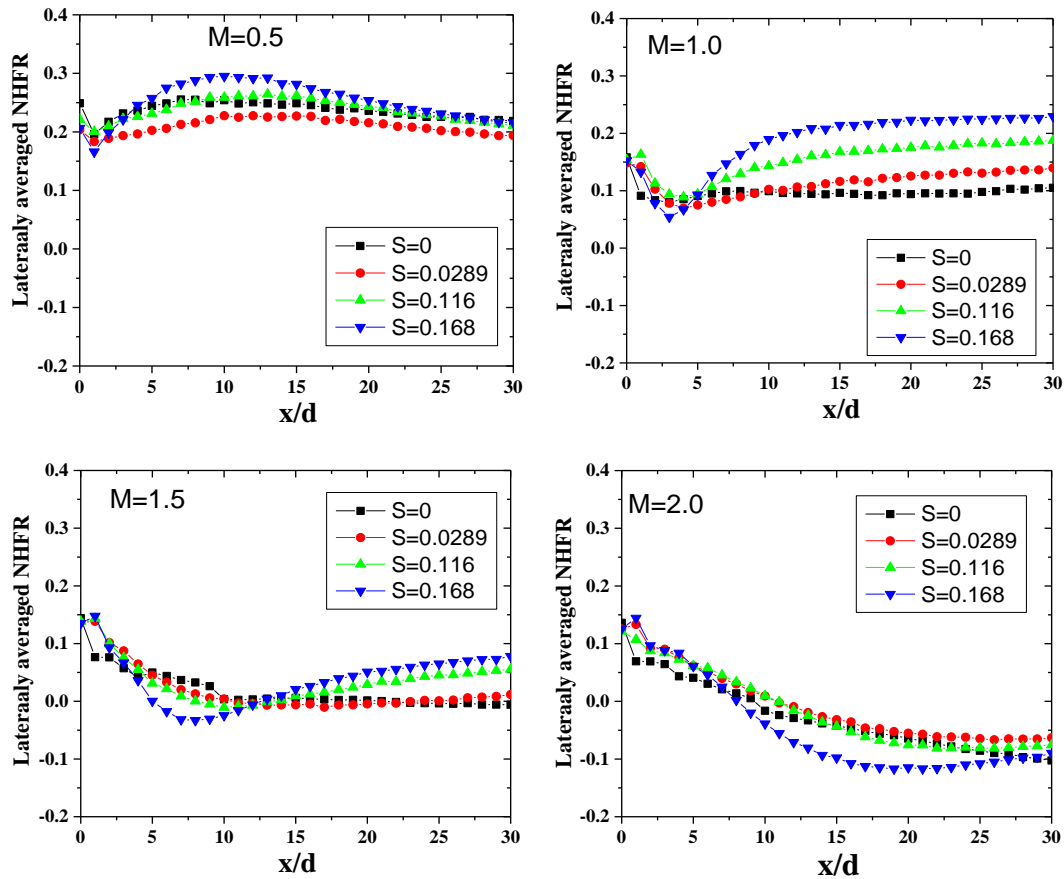


Figure 4.14. Reduction of the laterally averaged net heat flux in downstream of the film hole for different swirl numbers and blowing ratios.

The effect of twisted tape insert with different swirl numbers on the evaluated NHFR using laterally averaged quantities are shown in Figure 4.14 for $M = 0.5$ to 2.0. Mild coolant swirl ($S = 0.0289$) did not affect NHFR considerably compared with the zero swirl case except for $M = 0.5$, where a reduced NHFR is because of lower effectiveness values. But NHFR improves significantly with higher swirl numbers, which is the consequence of enhanced η and simultaneously keeping heat transfer coefficient values close to the non-swirl condition. The increase in blowing ratio appears detrimental as negative NHFR is observed for $M > 1.0$. Even though swirled

coolant for $M = 1.5$ and 2.0 produces substantial coolant coverage over the surface, a higher heat transfer rate deteriorates the NHFR values. Hence, it may not always be helpful to supply coolant at higher swirl numbers at high blowing ratios.

A direct consequence of the results observed in Figure 4.2 and Figure 4.6 is the improvement in the overall film cooling behavior represented as area-averaged effectiveness, as shown in Figure 4.15(a). The area-averaged effectiveness is defined as the average effectiveness evaluated over an entire film cooled surface. It can be determined as given below in Equation (4.2),

$$\bar{\eta} = \frac{1}{x/d \times z/d} \int_{x/d=0}^{x/d=30} \int_{z/d=-3}^{z/d=3} \eta(x/d, z/d) d(z/d) d(x/d) \quad (4.2)$$

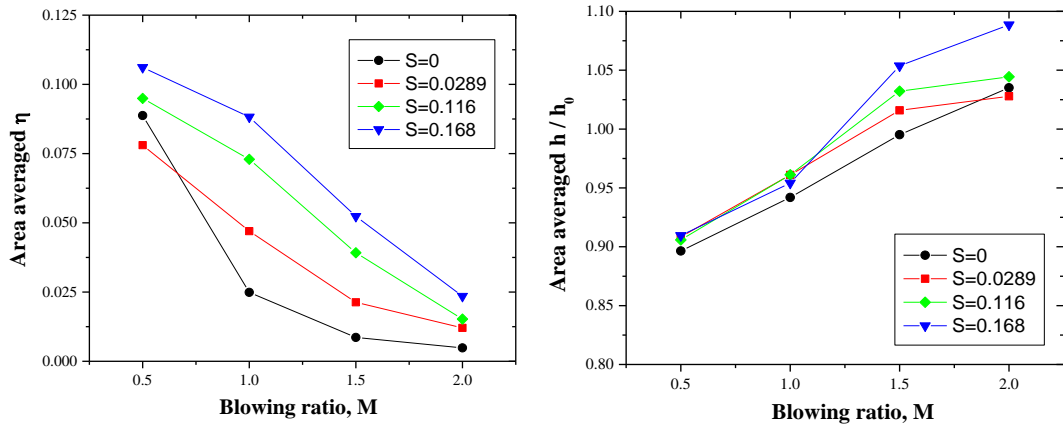


Figure 4.15. Area averaged film cooling (a) effectiveness (b) heat transfer coefficient for different swirl numbers and blowing ratios.

Area averaged effectiveness corresponding to all the swirl numbers studied are plotted with respect to the blowing ratio in Figure 4.15(a). An immediate observation is that the swirled film cooling produces higher effectiveness than non-swirled cases, which increases with swirl number. Average $\bar{\eta}$ gradually drops for higher blowing ratios due to the increased jet momentum resulting in coolant separation from the wall surface. The coolant swirl seems to have a minor effect at $M = 0.5$ and 2.0 due to lower momentum of the coolant jet in the former case. In the latter case, i.e., at $M = 2.0$, the coolant jet separation seems to dominate over the effect of swirl. It can be observed that the rate of increase in average $\bar{\eta}$ with S is high for $M = 1.0$ compared to other blowing ratios, which makes $M = 1.0$ an optimum blowing ratio for operational engine conditions.

For the present film cooling design, the computed heat transfer coefficient values are normalized and averaged over the surface area and are plotted against M for different swirl numbers and presented in Figure 4.15(b). It can be seen that the heat transfer rate is proportional to the blowing ratio since the increase in the blowing ratio amplifies the local turbulence levels. The addition of swirl to the coolant flow further enhances the disturbance in the mean flow, causing a higher heat transfer rate for swirled cases than non-swirled cases.

4.10 EFFECT OF SWIRL NUMBER – COOLANT HAVING HIGH SWIRL INTENSITY

In the previous sections it was observed that the film cooling effectiveness increases with swirl number. But, it is important to study till what extent of swirl number this statement holds true. Also, it is necessary to investigate the coolant jet behavior and its distribution at higher swirl numbers to widen the scope for the applicability of this method of swirl generation. Hence, the effect of swirl number is further studied for $S = 0.2, 0.4, 0.6$ and 0.7 in this section.

4.10.1 Effectiveness

Figure 4.16 illustrates the effect of swirl number on the laterally averaged effectiveness for $M = 0.5$ to 2.0 . It appears that when the blowing ratio is less ($M = 0.5$), effectiveness increases till $S \approx 0.4$ and decreases thereafter. For the case of $M = 1.0$, the $\bar{\eta}$ is higher for all swirl numbers at all x/d 's compared with $S = 0$ and the highest $\bar{\eta}$ occurs nearly at the same value of S as that of $M = 0.5$. The $\bar{\eta}$ at $M = 0.5$ for $S = 0.6$ and 0.7 falls below $S = 0$. Even though for $M = 0.5$ and 1.0 , a peak value $\bar{\eta}$ occurs at $S = 0.7$ but there is a steep decrease immediately after exiting the hole and drops to a very low values for a significant length along x/d . This might have occurred due to high swirl numbers which exters significant z -velocity component so that most of the coolant coming out of the hole gets completely mixed with mainstream. At $M = 1.5$ and 2.0 , the maximum $\bar{\eta}$ occurs at around $7.5 < x/d < 10$ for $S = 0.6$ and shows a gradual decrease in the downstream of coolant injection. Till x/d

< 7.5 , the jet separation due to high blowing ratio and the reattachment phenomena occurs.

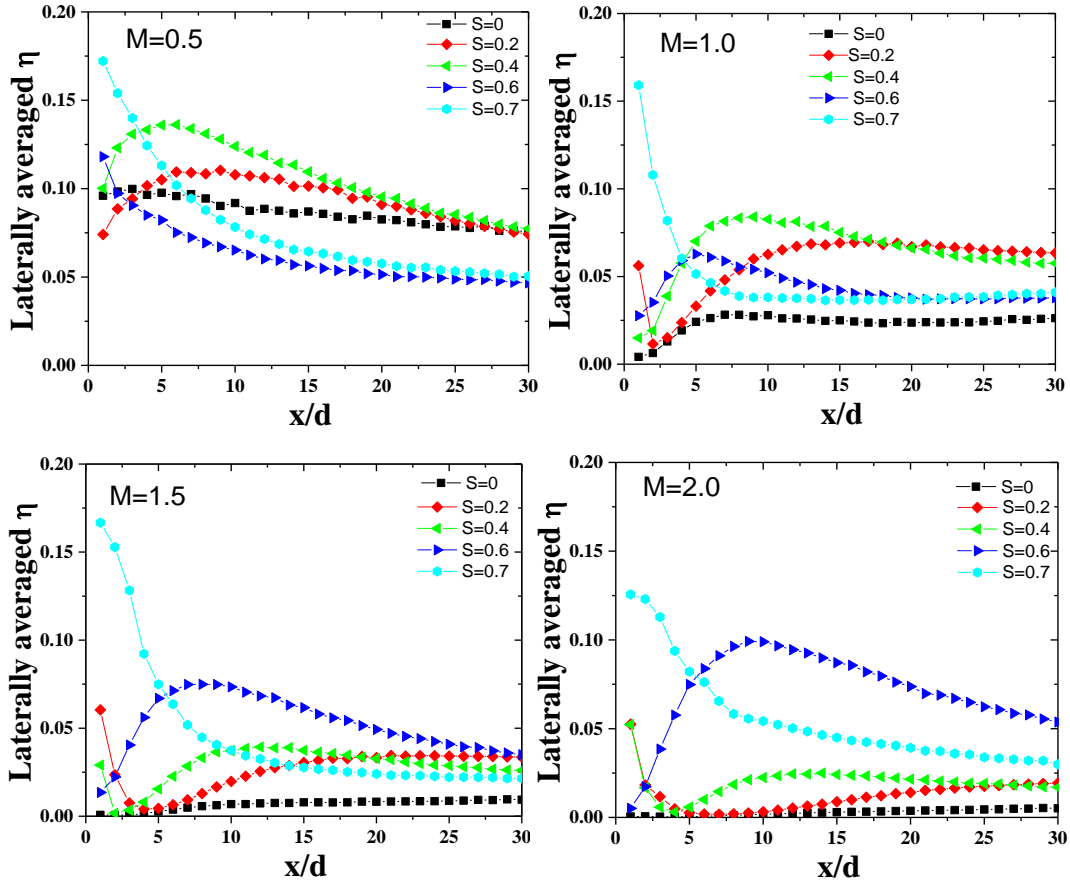


Figure 4.16. Laterally averaged effectiveness with respect to different swirl numbers at (a) $M = 0.5$, (b) $M = 1.0$, (c) $M = 1.5$, and (d) $M = 2.0$.

If we observe $\bar{\eta}$ values at the immediate downstream of injection (i.e., $x/d < 5$) there is a sudden drop till $x/d \approx 2$ or 3 and then starts increasing. The rate of increase from lowest to highest $\bar{\eta}$ value pretends to be a function of S where with increase in S this rate also seems to increase. But as far as the case of $S = 0.7$ is concerned, $\bar{\eta}$ distribution is not following such patterns instead, it peaks around $x/d \approx 1$ and then there is a sudden drop till $x/d \approx 7$ and a gradual decrease further downstream. In this case the swirl number dominates against the blowing ratio and hence there will not be any jet separation near the hole exit. The rate of coolant mixing with the mainstream will be so high that a majority of coolant quantity gets diluted by the mainstream with in a short distance ($x/d < 7$).

4.10.2 Heat transfer coefficient

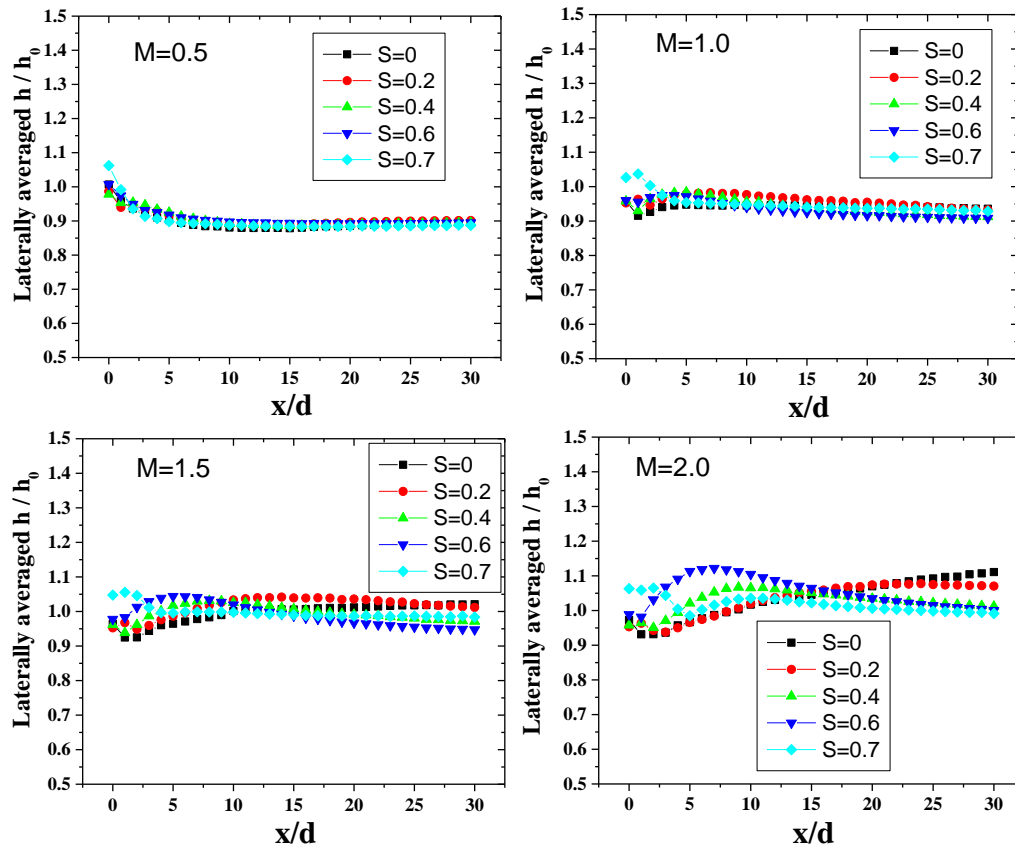


Figure 4.17. Heat transfer coefficient in the downstream of film hole.

Laterally averaged normalized heat transfer coefficients are plotted for different swirl numbers and blowing ratios in Figure 4.17. It is noticed that, \bar{h}/h_0 is less affected for $M < 1.0$ for all swirl numbers, but as M increases, a significant change can be observed. For $M > 1.0$, HTC starts increasing with S near the coolant injection location and decreases in the downstream. Both M and S contributes in increasing HTC values because both variables mainly generates more turbulence in the flow field. It appears that when the swirl is absent or very low, the coolant mixing happens away from the wall due to lift-off and hence HTC to stay lower. As the coolant reattaches to the wall in the downstream, the HTC increases. Major coolant-mainstream interaction occurs near the downstream at high swirl numbers, resulting in high HTC at these locations.

4.10.3 Net heat flux reduction ratio

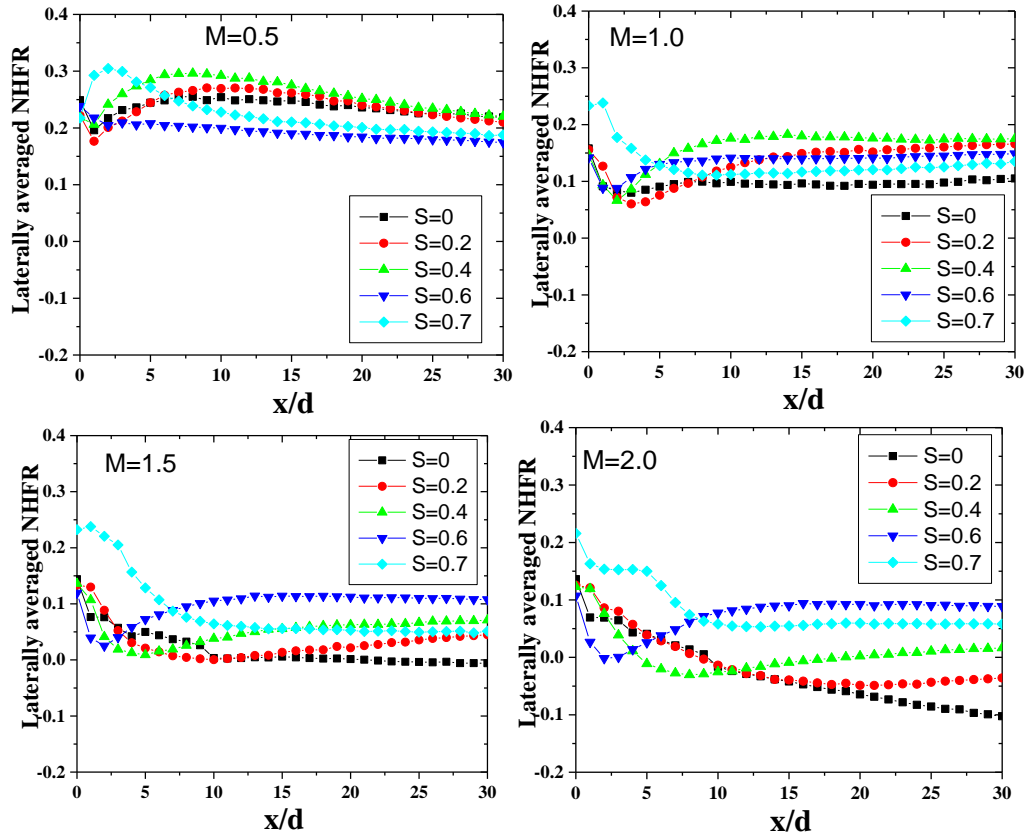


Figure 4.18. Reduction of the laterally averaged net heat flux in the downstream of film hole for high swirl numbers and blowing ratios.

The NHFR is calculated for higher swirl numbers for all blowing ratios and presented in Figure 4.18. In most of the cases, NHFR stays positive throughout the surface except for the case of $M = 2.0$. In this particular case negative values were appeared for $S = 0, 0.2$ and 0.4 cases. A major reason behind such deviation can be attributed to high HTC meanwhile no significant improvement in η . The trends of NHFR more or less follow a similar trend as effectiveness since NHFR is majorly driven by η . For $M \leq 1.0$, maximum NHFR obtained at around $S = 0.4$ and when M lies between 1.0 to 2.0, the highest NHFR is shifted towards $S \approx 0.6 - 0.7$.

4.10.4 Area averaged parameters

The area-averaged quantities of η , HTC and NHFR for higher swirl numbers are reported in Figure 4.19. $\bar{\eta}$ can be seen reducing with increasing in swirl numbers at low blowing ratios. But higher blowing ratio tends to increase η with swirl number.

This behavior might be because of the availability of more coolant mass flux which has a high tendency to penetrate, but the swirl is trying to reduce the fluid temperature inside the boundary layer by increasing the mixing of two fluid streams. An important observation that can be noticed is that the area-averaged effectiveness at $S \approx 0.6$, tend to yield more or less close η values for all blowing ratios. Further increase in both M and S appears to reduce area average η . Whereas, HTC is mildly affected by S compare to M . For a particular M , \bar{h}/h_0 is relatively constant. By looking at the combined effect of both parameters $((NHFR)_{\bar{\eta}})$, it can be deduced that high swirl numbers can certainly modify and increase the film cooling effect when the coolant is supplied at higher blowing ratios.

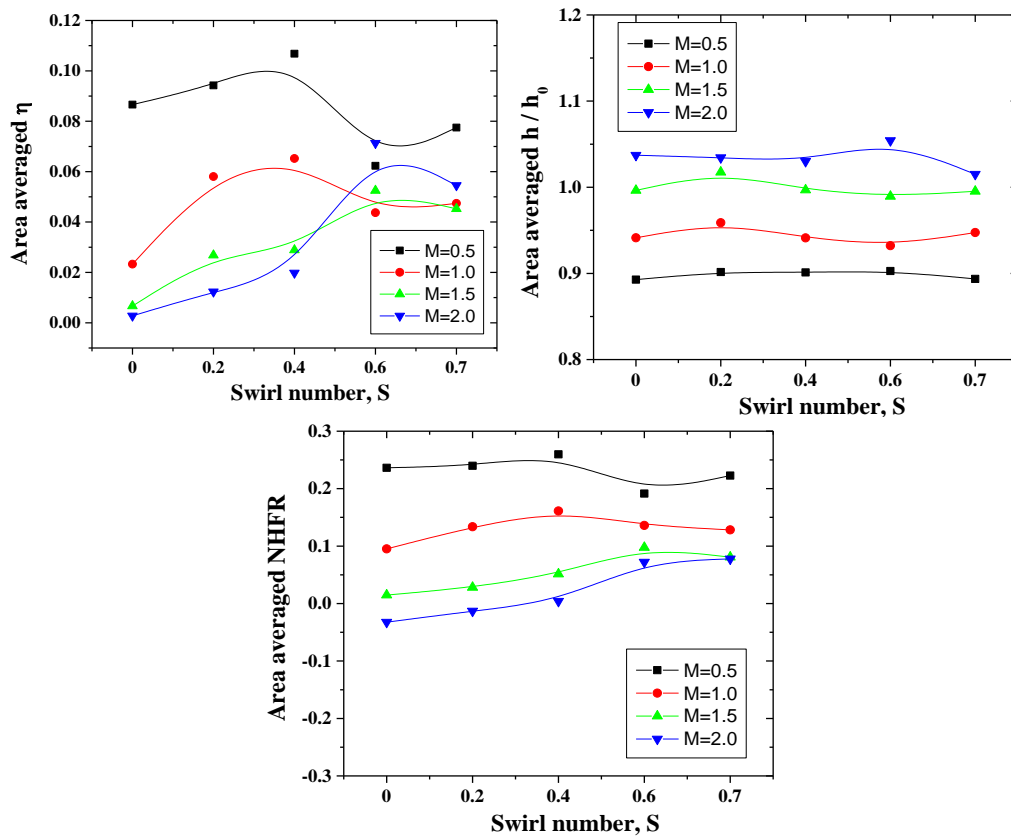


Figure 4.19. Area average quantities of effectiveness, heat transfer coefficient and NHFR for high swirl cases.

4.10.5 Flow features

To understand such behavior in the variation of $\bar{\eta}$ at different M and S , the local η distribution provides more clarity. Hence contours of η on $y - z$, $x - y$ and $x - z$ plane are plotted in Figure 4.20 - Figure 4.25 for the cases of $S = 0, 0.4$ and 0.7

at $M = 1.0$ and 2.0 . The flow patterns are represented through streamlines on the corresponding planes along with the contours.

On the center plane of symmetry ($x - y$ plane) at $z/d = 0$, the coolant jet lift-off reduces with the swirl number. The base case, Figure 4.20, has a thin layer of high temperature mixture along the length, just above the wall, whereas as S increased to 0.4 (Figure 4.21), low temperature fluid comes in contact with the wall after an initial separation for x/d of around 1 to 3. Further for the case of $S = 0.7$, Figure 4.22, the coolant jet tends to bend in such a way that the jet is attached over the surface starting from the point of jet exit. The streamlines at this swirl number are forced towards the wall when the coolant exits from the hole and then gradually moves away. But it appears that for $x/d > 6$, the surface is getting exposed to high temperature flow. This might be due to very high mixing rate at high swirl numbers where majority of the coolant jet is mixed immediately exiting the hole with the mainstream. At high blowing ratio in a non-swirled case, Figure 4.23, the jet moves even further away from the wall compared to Figure 4.20. Whereas for the swirled cases at $S = 0.4$ (Figure 4.24), there is an increased coolant spreading on the center plane. The streamlines are more evenly distributed but still, they are angled away from the wall. Further increase in swirl number to $S = 0.7$, creates a high degree of mixing meanwhile making the coolant jet to attach to the surface, as shown in Figure 4.25. In this case the streamline patterns are almost evenly distributed over the $x - y$ plane.

The second figure in each subfigure displays the top view of the film cooled surface, depicting the local lateral distribution of η over the surface. In case of Figure 4.25, the point of jet reattachment occurs nearly at $x/d = 4$, whereas for $S = 0.4$ (Figure 4.21), the jet seems almost continuous with a weak lateral distribution near the hole exit up to $x/d = 2$. Further increase in swirl number to 0.7 creates a strong disorientation of the coolant jet on the $x - z$ plane which can be observed in Figure 4.22. As the swirled coolant jet exits through the hole, it spreads towards $+z$ and along the downstream the jet stays more towards $-z$. When the blowing ratio is increased to 2.0 , the coolant jet in zero swirl case (Figure 4.23) is completely detached from the surface. Introducing a swirl of $S = 0.4$ at such high blowing ratio has very little effect, since the coolant concentration occurs mildly for $x/d > 6$ as

shown in Figure 4.24. Further increase in swirl intensity of coolant to $S = 0.7$ when $M = 2.0$ (Figure 4.25), creates a significant coverage over the surface throughout the downstream length. Hence it can be concluded that the adverse effect of the blowing ratio can be counteracted when the coolant is supplied with sufficient swirl strength to enhance the cooling performance.

As discussed in section 4.3, the structure of CRVP has been greatly affected by the strength of swirl imposed on the coolant flow. Figure 4.20 to Figure 4.25 shows the effectiveness distribution on $y - z$ planes at $x/d = 2$ and 8 for $S = 0, 0.4$ and 0.7 with $M = 1.0$ and 2.0 . When the swirl is absent (Figure 4.20), the coolant distribution produces a classic kidney shape generated by CRVP which is growing in size along the far field. At high blowing ratio (Figure 4.23), the center of CRVP moves away from the wall allowing more space for the mainstream seepage towards the plane at $z/d = 0$. When the swirl number is increased, a noticeable asymmetry of the vortices starts appearing slowly in the far field at $x/d = 8$ for $S = 0.4$ (Figure 4.21) and becomes significant as S tends towards 0.7 (Figure 4.22). The vortex on the $+z$ domain is growing stronger and becoming predominant whereas the opposite vortex is diminishing as it travels downstream. A major portion of the coolant lies in this dominant vortex, creating a rigorous mixing with the mainstream. Due to the weakened vortex on the $-z$ domain, the counterpart vortex is staying close to the surface resulting in achieving higher effectiveness.

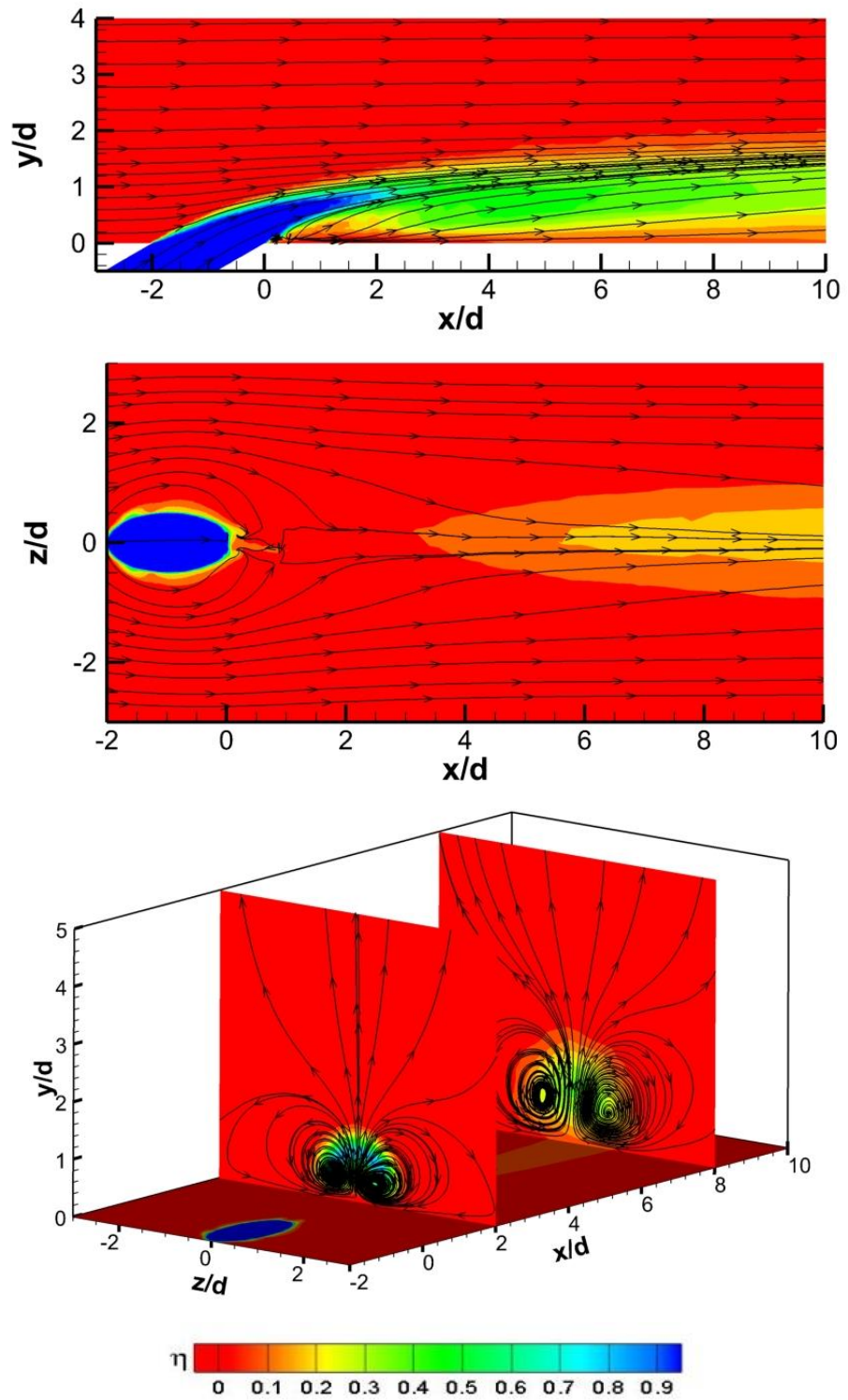


Figure 4.20. Contours showing the distribution of η on different planes along with the streamlines representing the flow pattern for $S = 0$, $M = 1.0$.

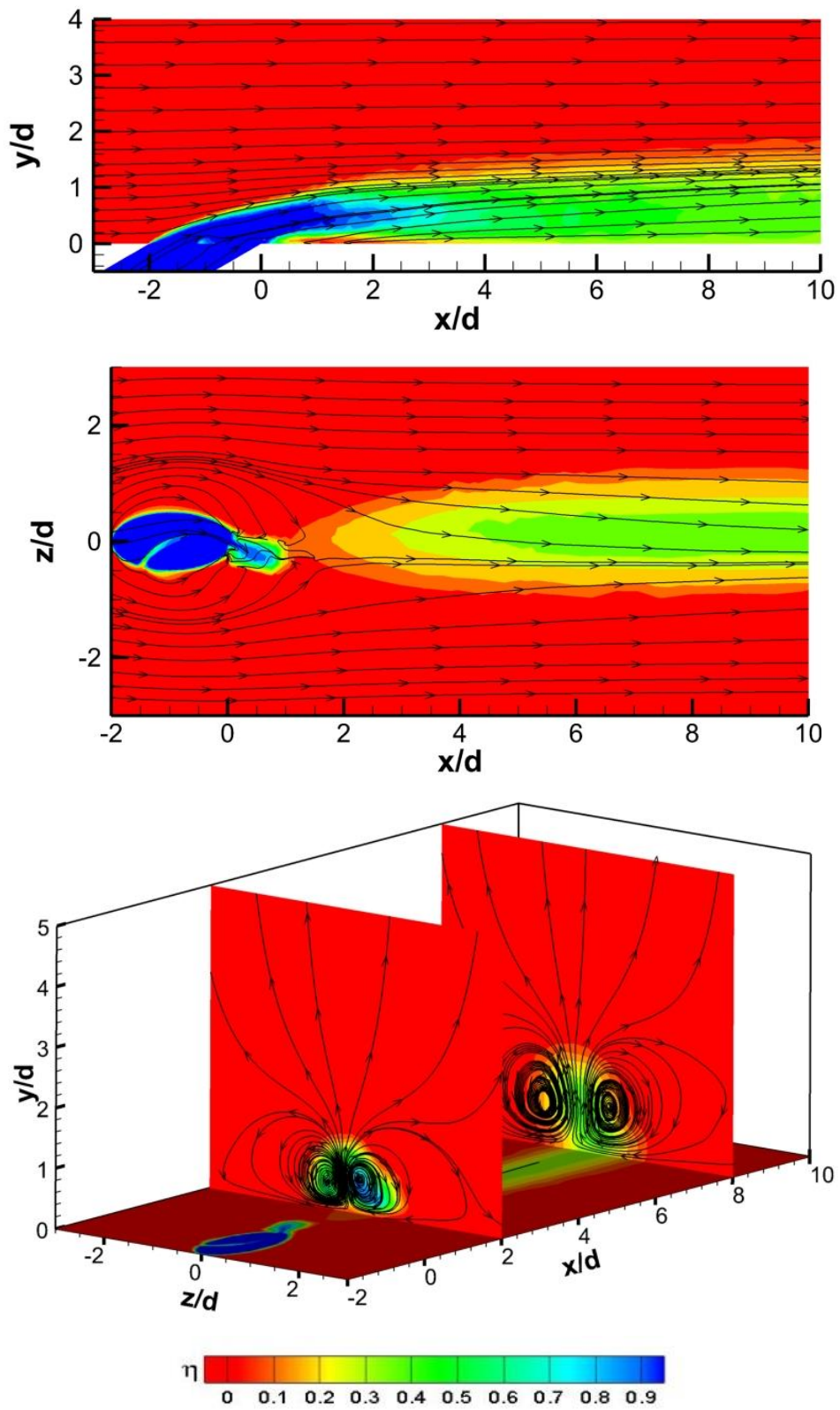


Figure 4.21. Contours showing the distribution of η on different planes along with the streamlines representing the flow pattern for $S = 0.4$, $M = 1.0$.

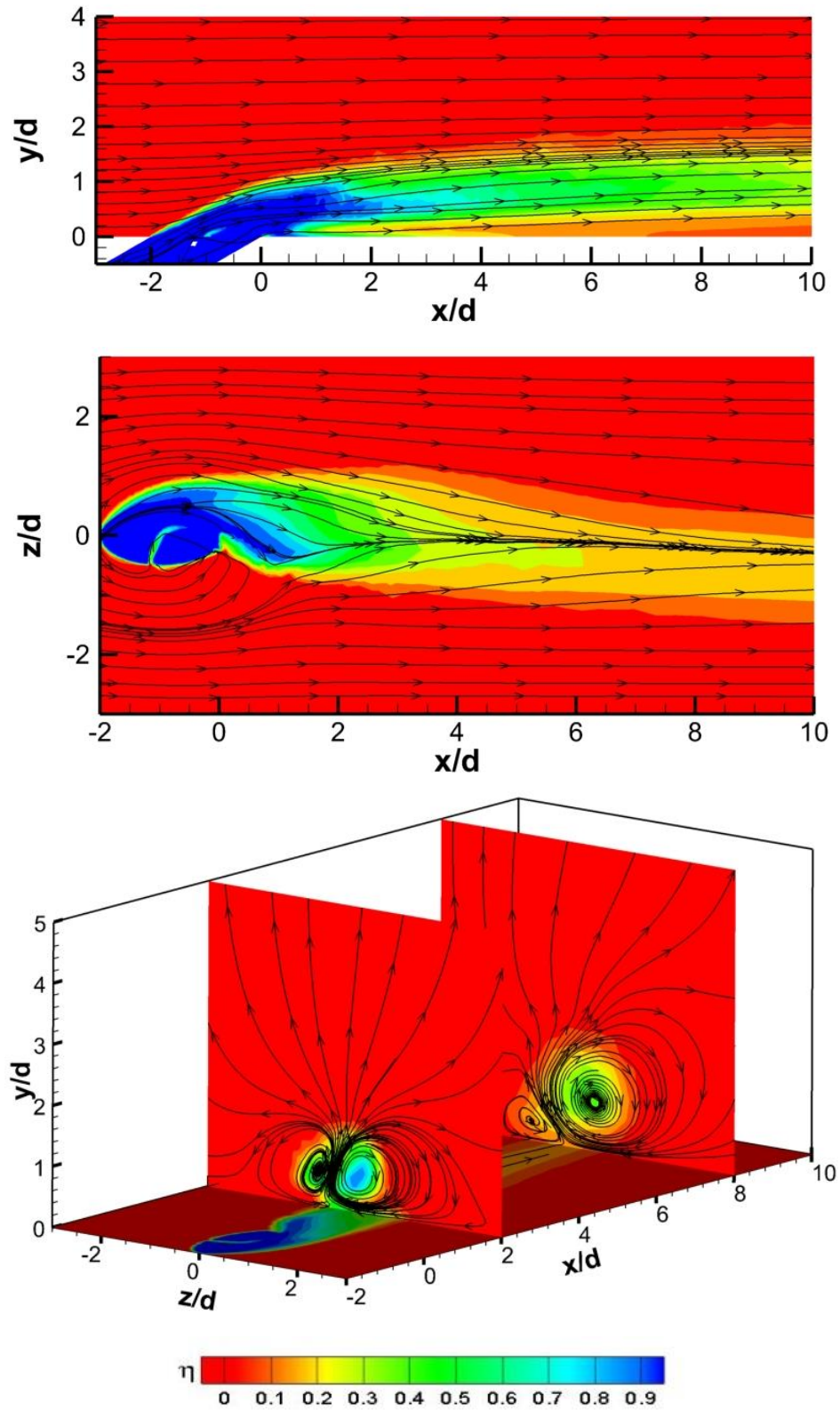


Figure 4.22. Contours showing the distribution of η on different planes along with the streamlines representing the flow pattern for $S = 0.7$, $M = 1.0$.

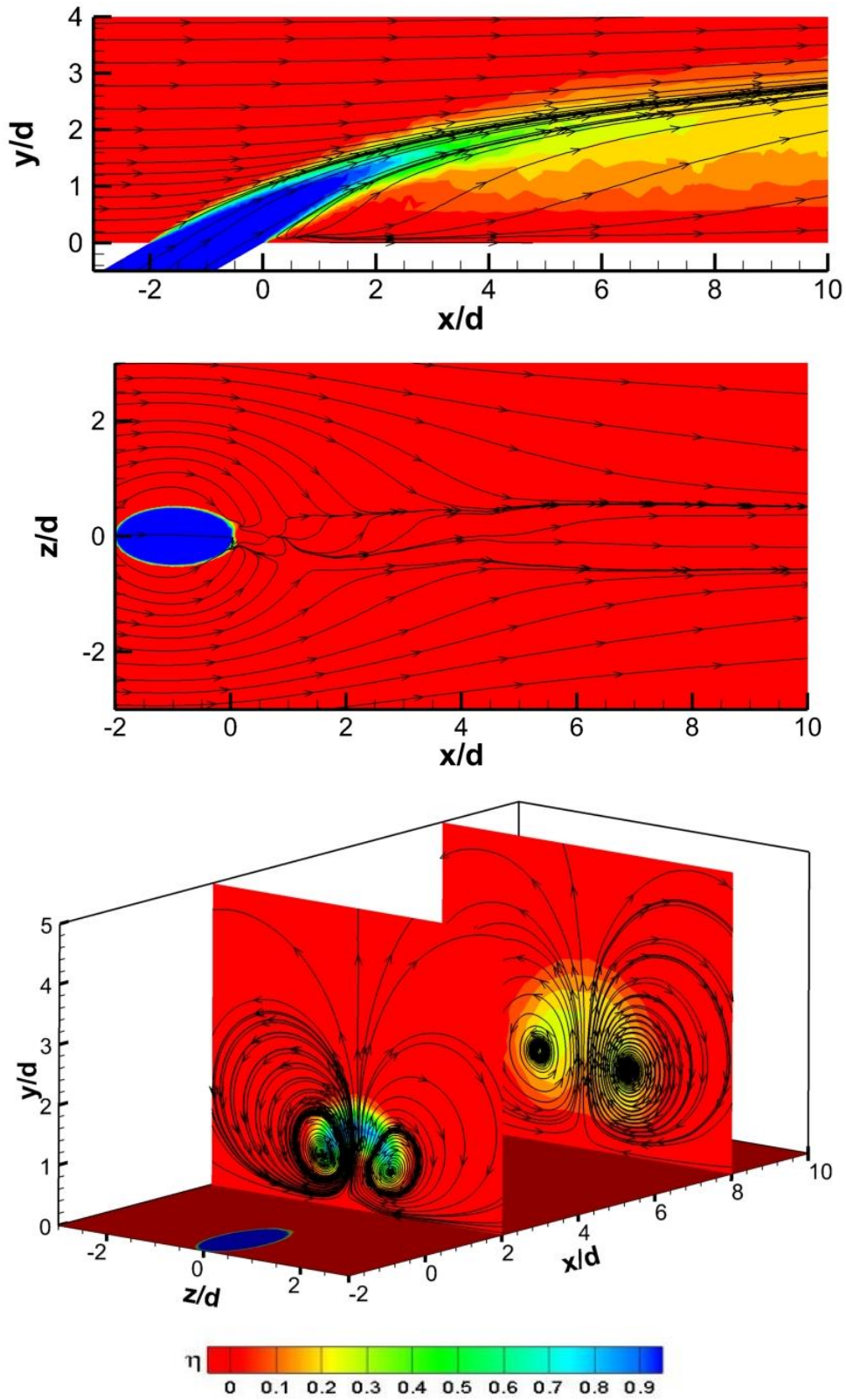


Figure 4.23. Contours showing the distribution of η on different planes along with the streamlines representing the flow pattern for $S = 0, M = 2.0$.

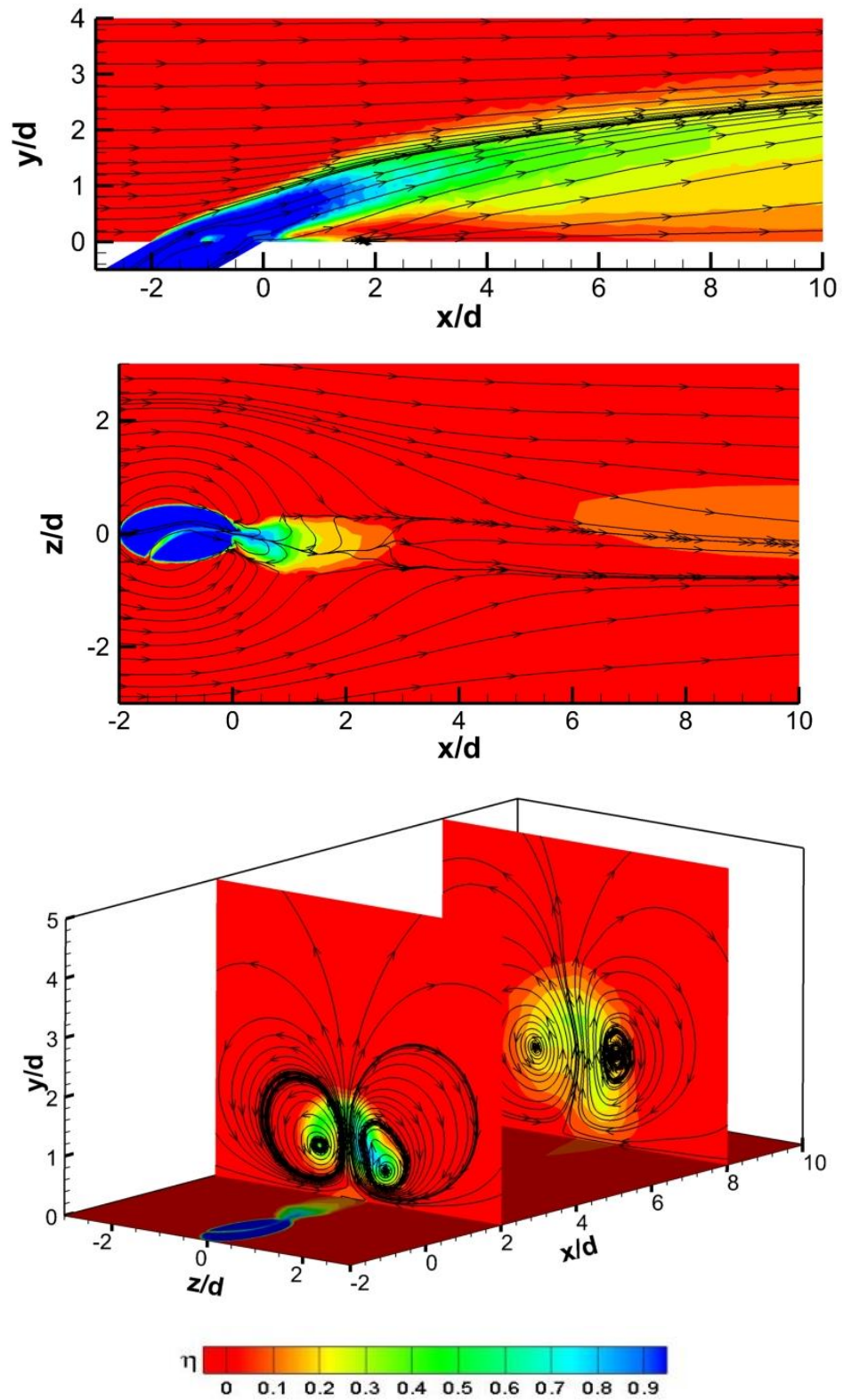


Figure 4.24. Contours showing the distribution of η on different planes along with the streamlines representing the flow pattern for $S = 0.4$, $M = 2.0$.

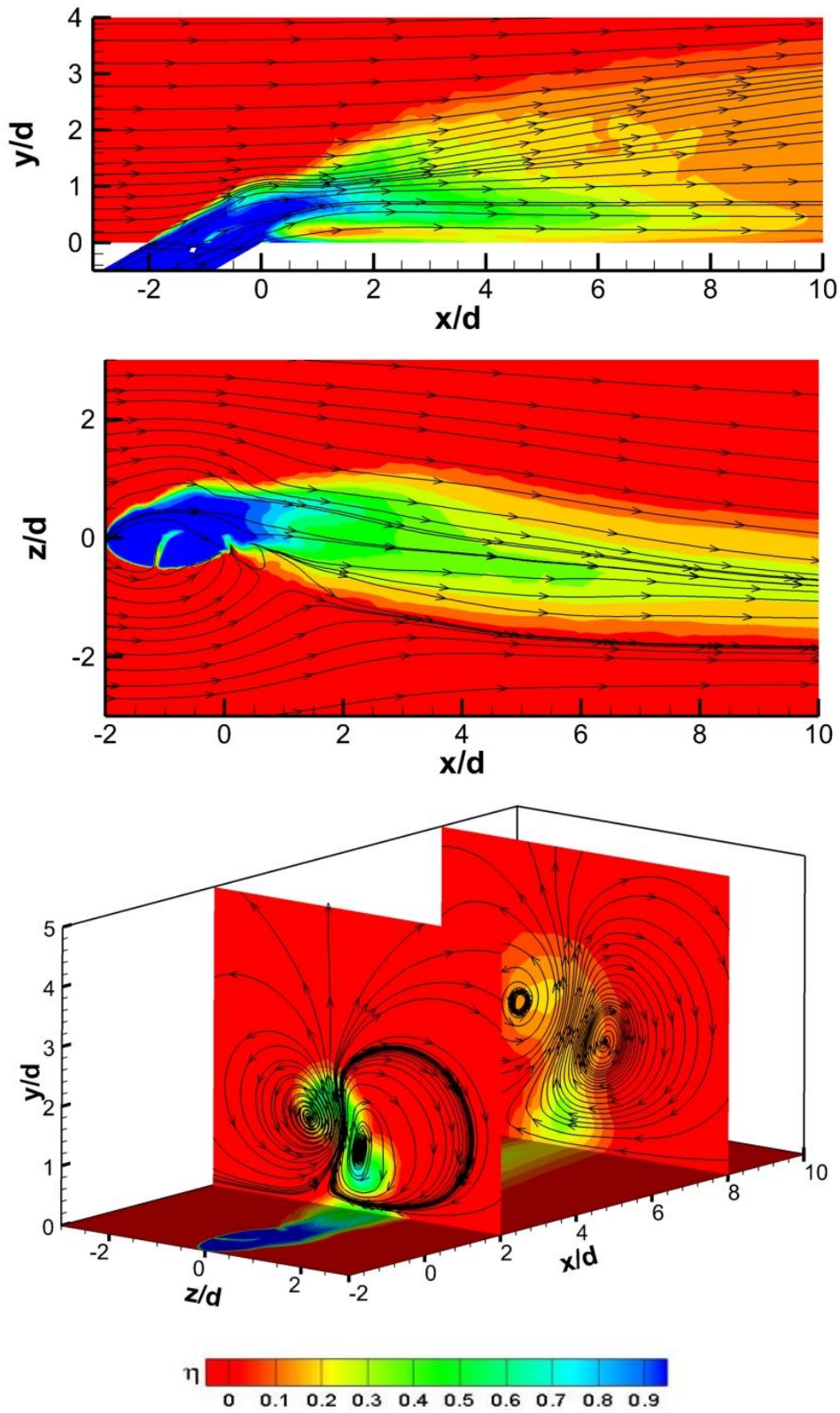


Figure 4.25. Contours showing the distribution of η on different planes along with the streamline representing the flow pattern for $S = 0.7$, $M = 2.0$

It is to be noted that the shape of CRVP gets influenced by the magnitude of coolant blowing ratio. At a higher blowing ratio, the kidney shape of scalar concentration no longer exists and the right lobe of CRVP on the +z surface gets distorted (Figure 4.24), which retains a small portion of coolant towards the surface. This becomes more compelling with an increase in blowing ratio as the concentration profile relatively gets divided into two parts as shown in Figure 4.25. Out of these two parts, one part lies above the wall and the other stays closer to the wall. Unlike low blowing ratio, in this case, both vortices are prevalent, but the right vortex is moderately elongated in y-direction.

4.11 EFFECT OF INJECTION ANGLE

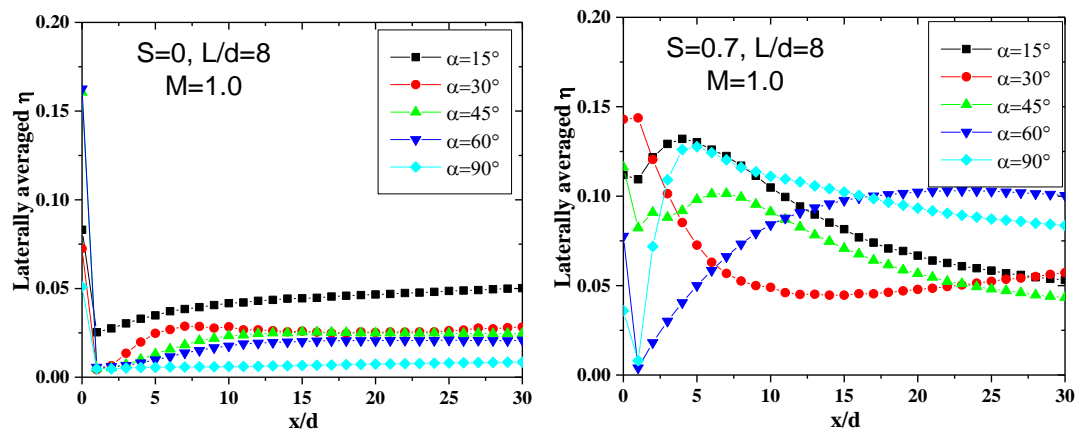


Figure 4.26. Effect of injection angle on laterally averaged effectiveness.

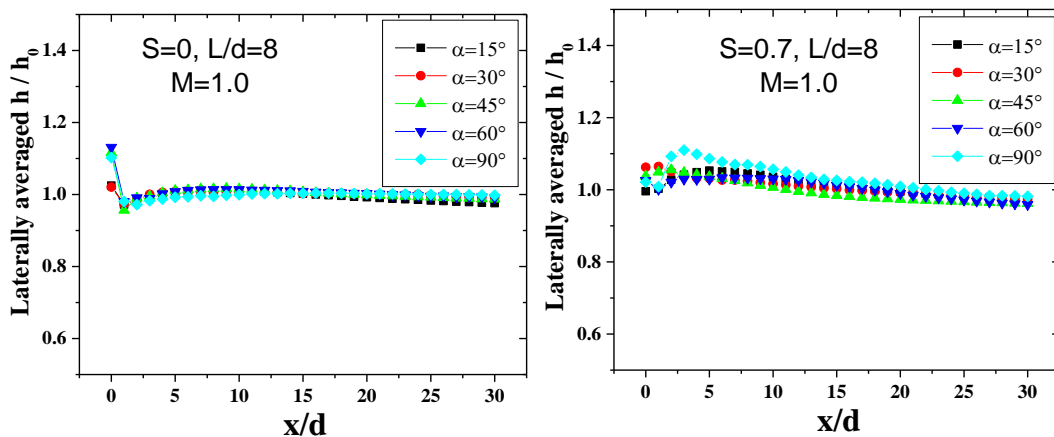


Figure 4.27. Effect of injection angle on laterally averaged heat transfer coefficient.

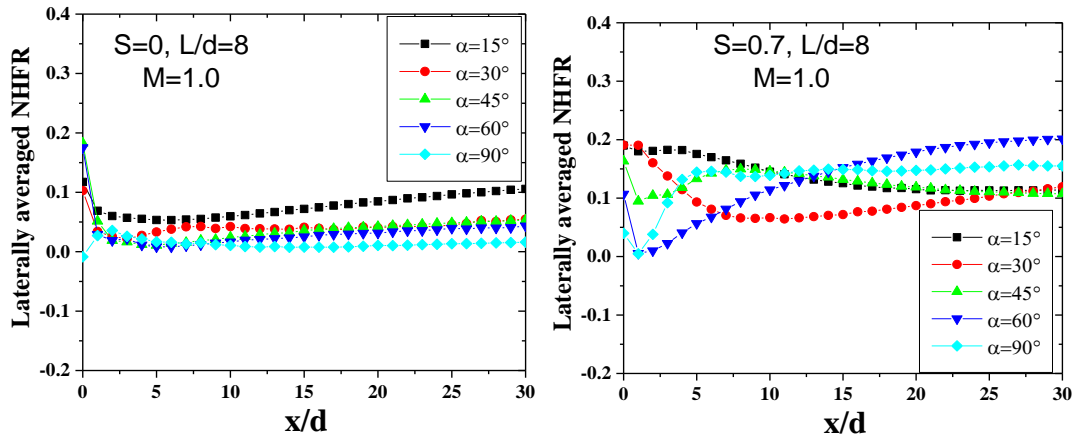


Figure 4.28. Effect of injection angle on laterally averaged net heat flux reduction.

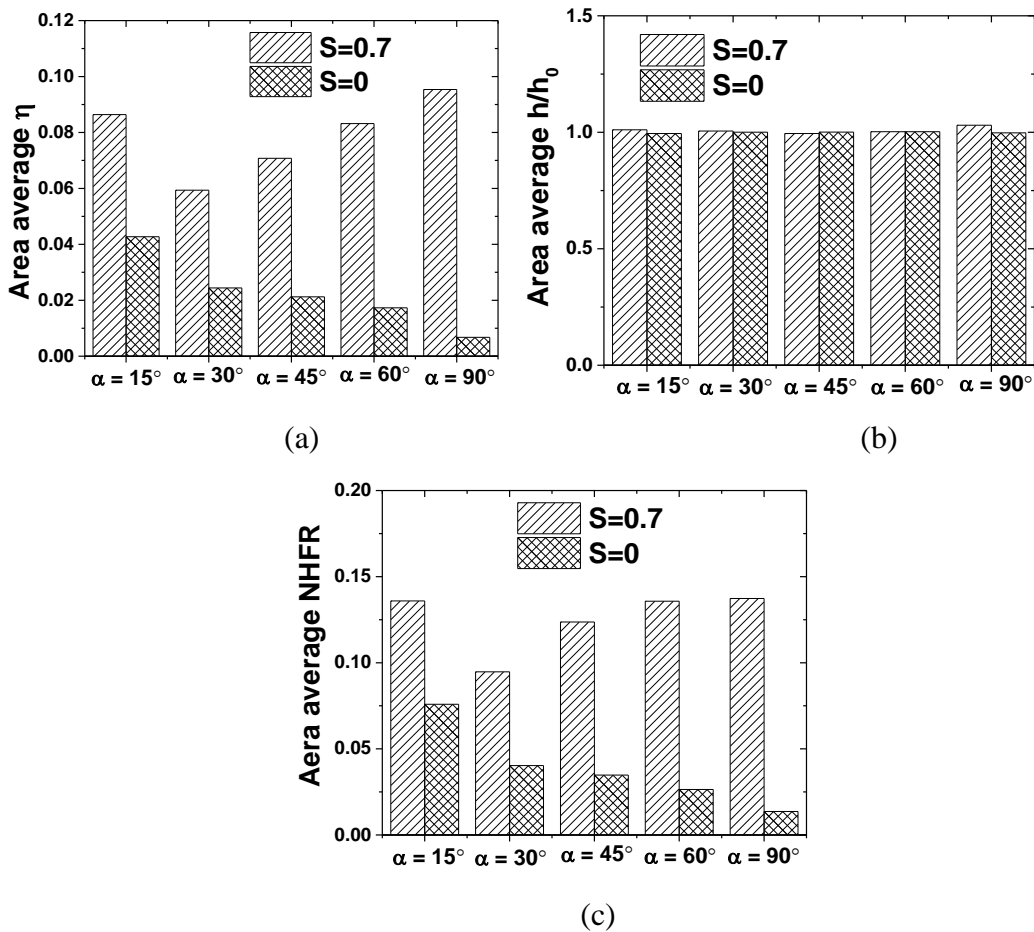


Figure 4.29. Comparison of area average quantities of (a) Effectiveness, (b) Heat transfer coefficient and (c) Net heat flux reduction for different injection angles.

Along with the blowing ratio and swirl number, the angle of inclination of the coolant hole can significantly affect coolant distribution. The results presented in the

preceding sections are obtained for the case of a 30° injection angle. Hence a parametric study is carried out by injecting coolant at various inclination angles.

The effect of injection angle on the film cooling behavior is studied by varying α from 15° to 90° . Figure 4.26 - Figure 4.28 shows the laterally averaged quantities of η , h/h_0 , and NHFR for $S = 0$ and 0.7 at $M = 1.0$. Values of η for the non-swirl case has moderately affected but showing obvious results where a lower injection angle produces better coolant distribution. At $\alpha = 30^\circ$, 45° and 60° , the distribution appears to be more or less similar over the surface. Only at $\alpha = 15^\circ$ and 90° , a noticeable change in the values of η can be observed. When swirl is introduced to the coolant flow, a drastic variation occurs in the distribution. With the low injection angles such as $\alpha = 15^\circ$, 30° and 45° , η peaks in near downstream and drops continuously along the downstream. As α crosses a certain limit, it appears that η starts with a very low value at the hole exit and increases further downstream. However, the case of $\alpha = 60^\circ$ yields more coolant accumulation on the surface than the case of $\alpha = 90^\circ$ in the far downstream. One major reason behind such peculiar behavior of the coolant flow could be due to the change in the shape of the film hole at the exit, which is a result of different inclination angles in the presence of twisted tape. Change in coolant exit profile primarily alters the y and z velocity components controlling the jet lift-off and lateral spreading.

Meanwhile, HTC seems to be least affected by the angle of injection for both cases ($S = 0$ and 0.7), as shown in Figure 4.27. In case of $S = 0$, a maximum difference in the HTC values are observed to be around 3% - 4% for all injection angles when compared with $\alpha = 30^\circ$ and for $S = 0.7$ this difference is less than 2%. Only the case of $\alpha = 90^\circ$ has slightly higher heat transfer rate for $x/d = 2$ to 5 with a deviation of around 5% - 6%. Hence the resultant NHFR follows a similar pattern as that of the effectiveness since it is the most influential parameter, as shown in Figure 4.28. It can be observed that for $S = 0$, $\alpha = 30^\circ$ gives highest reduction in heat flux than other injection angles, while for $S = 0.7$, $\alpha = 15^\circ$ would be best in the region immediately after injection. Whereas $\alpha = 60^\circ$ might be effective in reducing the heat flux over the far downstream region. It can also be observed that the values of NHFR

obtained for injection angles of 15° , 45° and 90° are higher for $S = 0.7$ than the case of $S = 0$.

In order to decide an optimum injection angle, area averaged η , h/h_0 and NHFR are calculated and plotted in Figure 4.29 (a), (b) and (c), respectively. It appears η continuously deteriorates with α when $S = 0$ whereas it improves when $S = 0.7$. The effect of α on HTC can be considered insignificant even in the presence of coolant swirl. On the other hand, NHFR is highest at $\alpha = 30^\circ$ when $S = 0$ but it is lowest for $S = 0.7$. Also it is observed that the injection angles of 15° , 60° and 90° have resulted approximately the same amount of area averaged net heat flux reduction.

4.12 EFFECT OF HOLE LENGTH-TO-DIAMETER RATIO

The effect of hole length on the film cooling characteristics is presented in Figure 4.30 to Figure 4.33 for hole length-to-diameter ratios of 4, 8, 12 and 16. It was observed that non-swirl cases showed a negligible effect on $\bar{\eta}$. These results are in accordance with the experimental work of Golstein and Ekart (1973) for a long hole that supplies coolant with the fully developed condition and a short hole. On the other hand, in the case of $S = 0.7$, Figure 4.30, a major effect can be seen for $x/d < 10$ where $L/d = 4$ produced lowest effectiveness and $L/d = 16$ resulted in highest $\bar{\eta}$. There is almost 80% - 90% increment in $\bar{\eta}$ occurs in this region and further downstream, there is a difference of around 30%. HTC also follows similar behavior as that of η as shown in Figure 4.31. When $S = 0$, shortest and longest holes have produced as high as 1.8% increase in h/h_0 , while $S = 0.7$ resulted in a highest increment of around 8% at $x/d = 1$ and around 4% in most of the downstream locations. It is to be noted that $L/d = 4$ creates a low HTC near the hole exit and increases subsequently whereas for $L/d > 4$, HTC is highest near the exit and reduces afterwards. If we compare the trends of h/h_0 for $S = 0$ and $S = 0.7$ of $L/d = 4$, then both cases appears to follow similar trend. Hence a short hole might not be able produce significant effects on film cooling performance even when a swirl is introduced on the coolant flow path. This might be due to insufficient hole length to impart the tangential velocity components on the coolant.

The effect of hole length on NHFR is shown in Figure 4.32, gives up to 60% reduction in heat flux for $S = 0$ between $L/d = 4$ and $L/d = 16$ at $x/d = 3$ whereas for $x/d > 15$, the case of $L/d = 4$ gives 10% better protection than $L/d = 16$. In case of $S = 0.7$, $L/d = 16$ improves the protection against hot gases up to 100% for $5 < x/d < 10$ than $L/d = 4$. When looking at the area averaged quantities, the η in case of $S = 0$ (Figure 4.33(a)) appears to deteriorate with L/d while $S = 0.7$ shown an average improvement of 60%. The HTC (Figure 4.33(b)) is mildly affected with respect to L/d as well as the presence or absence of coolant swirl. The NHFR (Figure 4.33(c)) exhibits an improvement of around 80% from $L/d = 4$ to 16 in the presence of swirl meanwhile there is only 2% enhancement can be observed for a non-swirl case. Hence a higher length of film hole is desirable to achieve better surface protection.

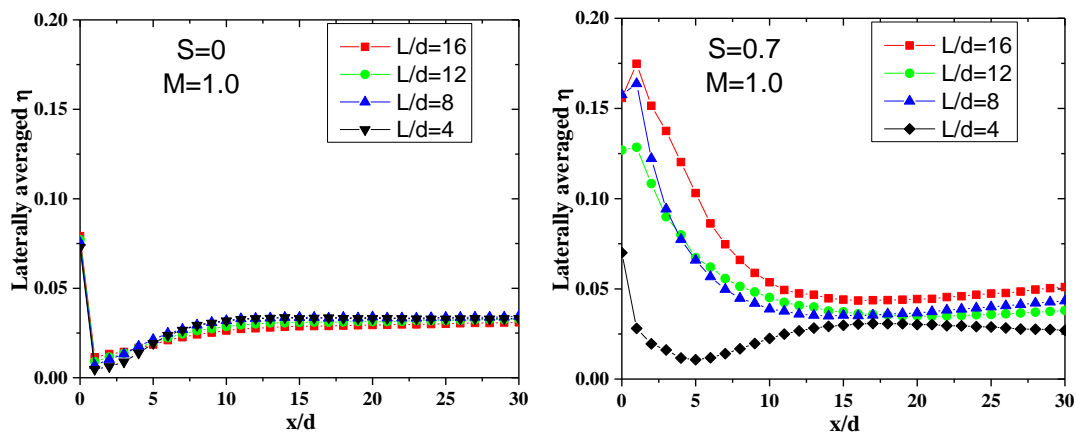


Figure 4.30. Effect of L/d on laterally averaged effectiveness.

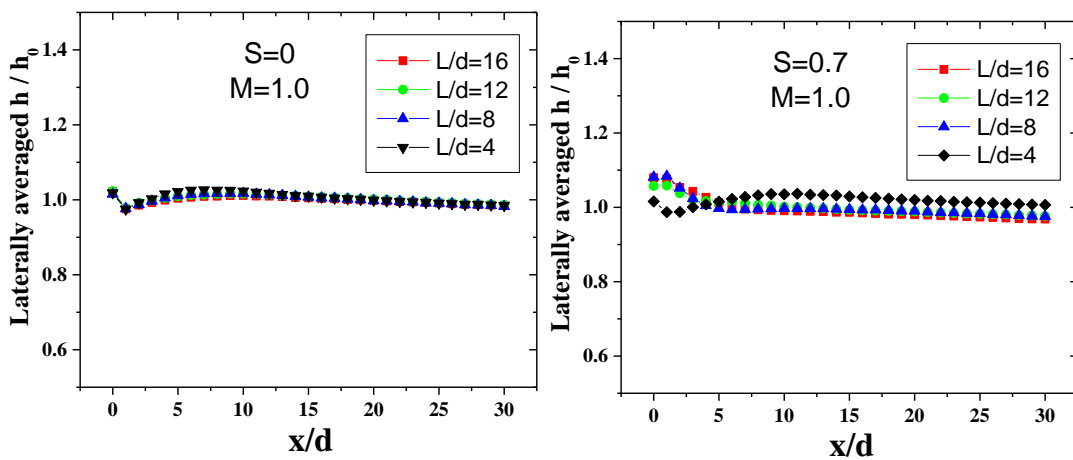


Figure 4.31. Effect of L/d on laterally averaged heat transfer coefficient.

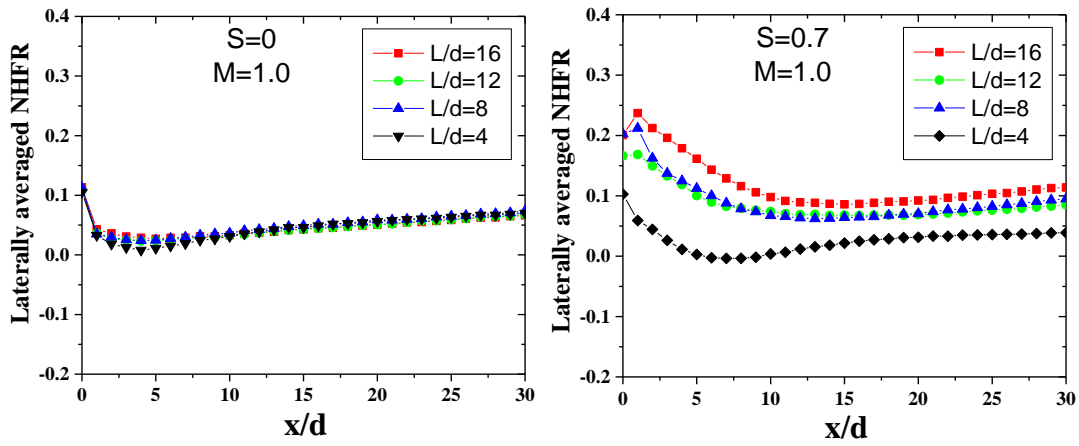


Figure 4.32. Effect of L/d on laterally averaged net heat flux reduction.

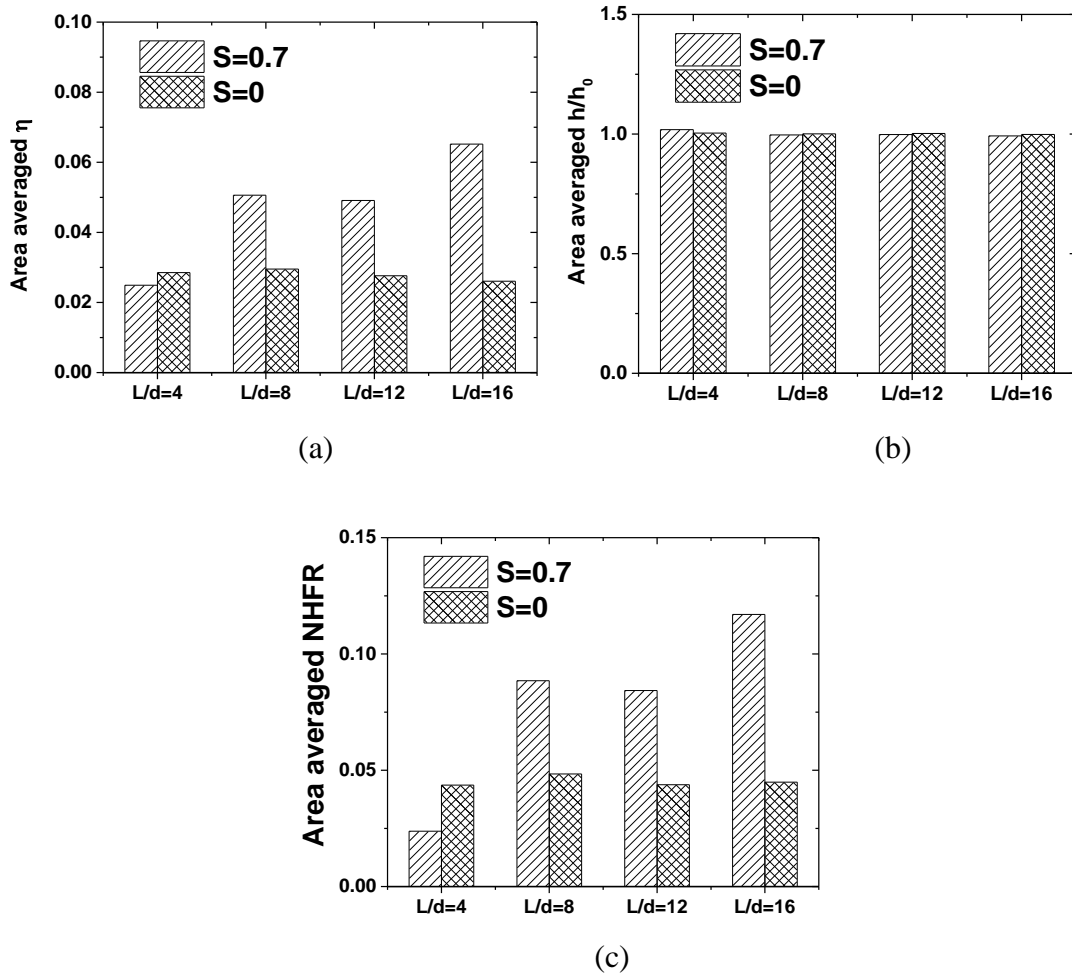


Figure 4.33. Comparison of area average quantities of (a) Effectiveness, (b) Heat transfer coefficient and (c) Net heat flux reduction for different L/d ratios.

4.13 CLOSURE

This chapter presented the film cooling behavior in terms of effectiveness, heat transfer coefficient and net heat flux reduction for different swirl intensities, injection angles, and hole lengths. The effect of swirl intensity is elaborately discussed using temperature and velocity contours and streamlines on various locations. The coolant swirl number is found to be a major parameter in enhancing film cooling performance via modified CRVP structures. The parameters such as S , α , and L/d can be seen affecting the coolant distribution individually, but evaluating an optimum combination of these three parameters is essential. Hence, the following chapter discusses optimizing the geometric parameters in case of swirled film cooling.

Equation Chapter (Next) Section 1

CHAPTER 5

OPTIMIZATION OF GEOMETRICAL PARAMETERS IN SWIRLED FILM COOLING

5.1 INTRODUCTION

The influence of geometrical factors such as coolant swirl number, injection angle and hole length on film cooling characteristics was explored in the previous chapter. These parameters appear to have a high degree of non-linearity with the effectiveness. Hence it becomes highly challenging to represent the interconnection between the input parameters and the output variable in terms of mathematical correlations. A surrogate model can be constructed in such situations to obtain the relationship between input and output variables. This surrogate model can then find the optimum design point, such as maximized effectiveness.

The optimization of geometrical parameters of film cooling such as coolant swirl number, injection angle and length of the hole to obtain maximum effectiveness is discussed in the present section. The optimization procedure mainly involves four steps. Design variables and their upper and lower bounds are decided in the first step. Sampling points are generated for the design variables using an efficient data sampling method since the efficiency of the surrogate model mainly depends on it. The second step involves conducting numerical simulations for the data sets obtained from the first step and calculating the corresponding effectiveness values. A surrogate model is constructed in the third step using the data obtained from CFD solutions. The last step comprises of finding the optimum design point using an efficient optimization algorithm.

In the present work, the sampling points are collected through Latin Hypercube Sampling (LHS) technique and the surrogate model is constructed using a Radial Basis Function Neural Network (RBFNN). Table 5.1 shows the three design variables and their corresponding lower and upper limits which are considered in the present study. The sampling points of the design space variables are divided into

training points and testing points. The RBFNN model is constructed using the training data sets containing input parameters and their corresponding outputs. A trained neural network is tested against unknown data points to know the accuracy level of the network in predicting the output for unknown sets of input values. The optimization of the design variables is carried out using one of the global optimization techniques known as genetic algorithm (GA).

Table 5.1. Design variables and corresponding lower and upper limits used to evaluate the optimum design point.

Design Variables	Lower bound	Upper bound
S	0	0.7
α	15°	90°
L/d	4	16

Swirl number is varied from 0 to 0.7 with $\Delta S = 0.1$, injection angle is varied from 15° to 90° with $\Delta\alpha = 5^\circ$ and variation of hole length is considered from $L/d = 4$ to 16 with $\Delta L/d$ of 1. Around 45 sampling points are generated for the design variables between the upper and lower limits using Latin Hypercube Sampling technique in matlab.

5.2 LATIN HYPERCUBE SAMPLING

The number of samples and the distribution of sampling points in the design space can significantly enhance a neural network's performance. A random sampling technique does not ensure covering the entire design space and there is a possibility of getting repetitive samples leading to considerable variance. On the other hand, LHS generates stratified sampling points, which ensure only one sample point from each row and column of the design space. The stratification in LHS is achieved by equally dividing the probability density function of the variables into n intervals and randomly selecting the variable within the intervals. Figure 5.1 shows the distribution of LHS data points generated from 'lhsdesign' function available in Matlab throughout the design space, which are used for training the neural network. The output, spatially averaged effectiveness corresponding to the training data points are

color contoured based on the corresponding η_s values. The data set used to test the performance of RBFNN is also shown in Figure 5.1, represented by cubes and η_s values are mentioned over them. The η_s values for the training and testing data sets are obtained by running RANS based CFD simulations using ANSYS Fluent, as explained in chapter 3.

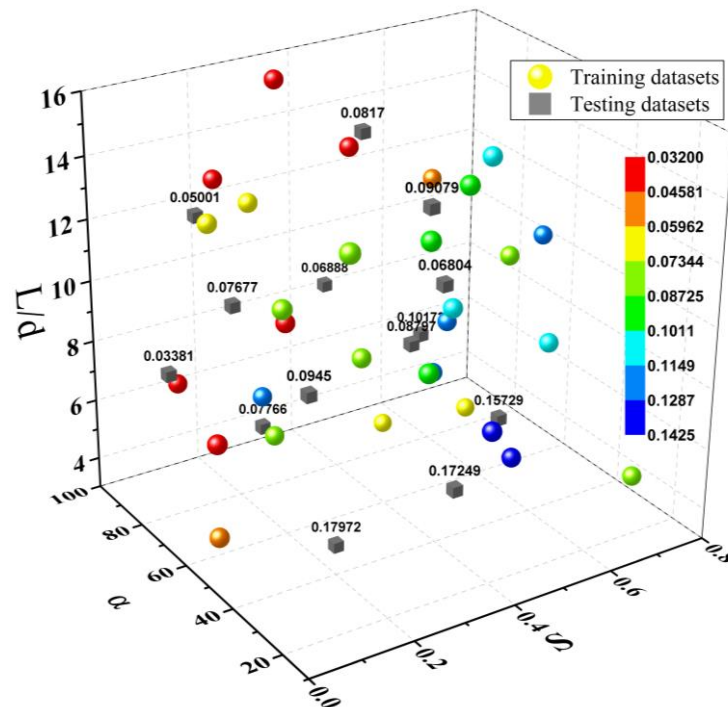


Figure 5.1. Sampling points distributed in latin hypercube space for training and testing the RBF neural network.

5.3 RADIAL BASIS FUNCTION NEURAL NETWORK

The surrogate model used to predict film cooling effectiveness is constructed using a Radial Basis Function Neural Network (RBFNN) in the present work. RBF neural network is a three-layer feed-forward network consisting of one input layer followed by a hidden layer and an output layer. This an added advantage of using an RBFNN since, it eliminates the requirement of finding an optimum number of hidden layers required to create a network. Also, the RBFNN creates one neuron for each variable which avoids the necessity of conducting a neuron independent study.

A typical structure of RBFNN, when applied to the present class of problems, is shown in Figure 5.2. The input layer is made up of vectors of input parameters

which are design space variables in the present case. The hidden layer consists of radial basis neurons, which uses the Gaussian transfer function defined as,

$$\varphi(g) = \exp\left(-\frac{\|g - c\|^2}{2\zeta^2}\right) \quad (5.1)$$

where ζ is the variance of Gaussian distribution. The term $\|g - c\|$, in Equation 5.1, is called Euclidean distance between the center c and the input vector g . The output layer is computed as,

$$O(g) = \sum_{j=1}^n w_j \varphi_j(g) + e_j \quad (5.2)$$

where w is the weight and b is the bias associated with every neuron in the hidden layer. The transfer function used in the output layer is a linear neuron. Weights are multiplied to the output from the hidden node, and a bias will be added to form an output layer neuron. The value of variance in Equation 5.1 is calculated from the spread constant. The matlab function ‘newrb’ creates a trained RBF neural network by taking input and output vectors along with a spread constant. A suitable value for the spread constant is evaluated by trial and error, which can develop the model having a maximum R^2 value.

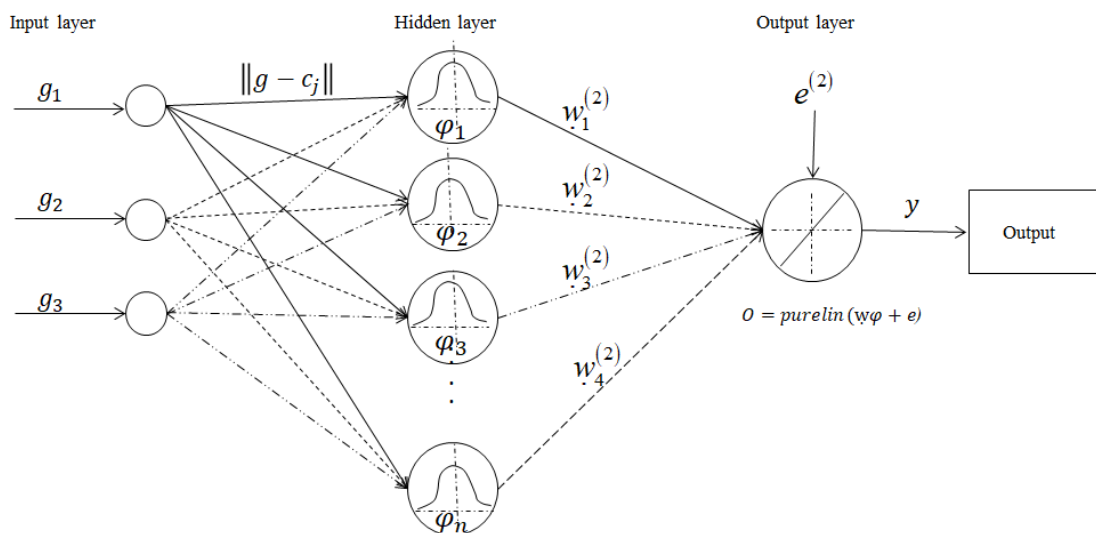


Figure 5.2. A typical structure RBFNN consists of three input variables and a single output vector.

Figure 5.3 compares the correlation between measured data points from CFD with the predicted values of effectiveness by RBFNN for both training and testing data sets. The ANN model has been trained by achieving a correlation coefficient of 0.903 and the same model has produced an R-value of 0.934 for the test data set. The regression equation corresponding to the output is given on the ordinate axis. A total of 45 data points were generated through LHS, of which 30 data points were used to train the RBFNN model, and the remaining 15 were used to validate the model. The value of the spread constant can be adjusted such that the trained model would produce an R-value equal to 1. However, as R increases towards 1, the model seems to get to overfit for the training data set and degrades its generalization to any unknown data points. Hence, in the present study, the spread constant is chosen such that the model response to the test data set results in the highest R-value while maintaining sufficient accuracy with the training data set.

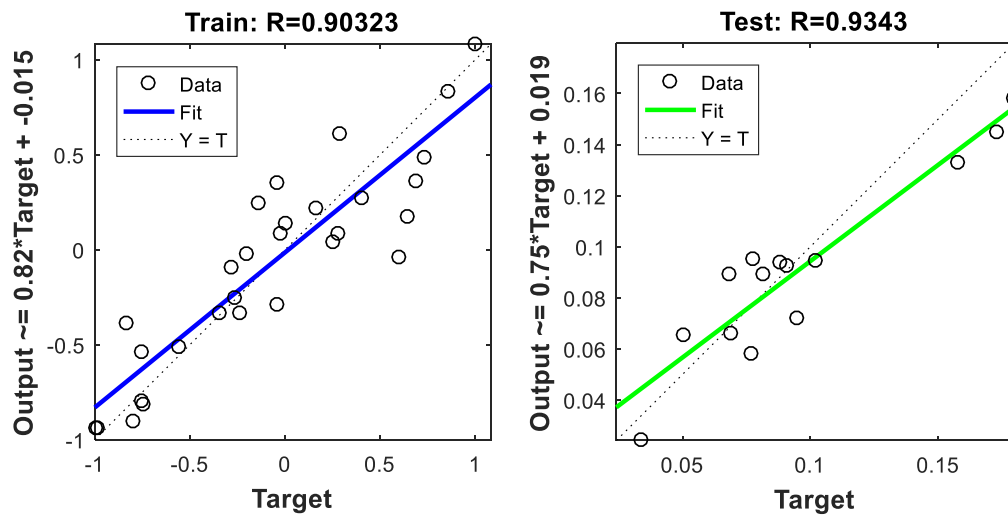


Figure 5.3. Training and testing accuracies of RBFNN model of the present study.

5.4 GENETIC ALGORITHM

Once the neural network model is constructed, the geometrical variables are optimized using one of the robust global optimization techniques known as genetic algorithm (GA). It is an evolution-based method that tries to generate better offspring from the existing population by removing weaker generations and arriving at the best design. In the present optimization problem, the optimum value of design variables within the design space is found using the Genetic Algorithm (GA) tool available in

matlab. The GA uses the RBFNN model to search globally for the optimum design point between the upper and lower limits of S , α , and L/d . The main objective of the present optimization is to maximize the spatially averaged effectiveness (η_s) defined as,

$$\eta_s = \frac{1}{x/d \times z/d} \int_{x/d=0}^{x/d=20} \int_{z/d=-2}^{z/d=2} \eta(x/d, z/d) d(z/d) d(x/d) \quad (5.3)$$

The GA tool in matlab tries to minimize the output of a particular fitness function which is obtained from the trained RBF neural network in the present case. Hence the fitness function for the optimization is defined as,

$$\min \{F(S, \alpha, L/d)\} = \frac{1}{\eta_s(S, \alpha, L/d)} \quad (5.4)$$

The flowchart shown in Figure 5.4 depicts the conventional steps involved in optimization using GA. The optimization tool in matlab takes the fitness function, total number of design variables and their upper and lower bounds as input parameters. The fitness function is defined as a separate function that contains the trained RBF neural network and evaluates the objective function value as a scalar using the three input variables supplied by the GA tool.

Before starting the optimization process, a population size of 50 individuals is defined. A rank based fitness scaling function is chosen, and a stochastic uniform function is used to select the parents allowed to produce the next generation. The mutation is carried with a Gaussian function which implies random changes to the populated individuals. In the next step, two individual parents are combined to produce the next generation or the offspring, known as crossover. The crossover is carried out at a random location of the parents. At last, the iteration is stopped by specifying three different stopping criteria: a maximum number of generations of 300, 50 stall generations, and a fitness function tolerance of 10^{-6} .

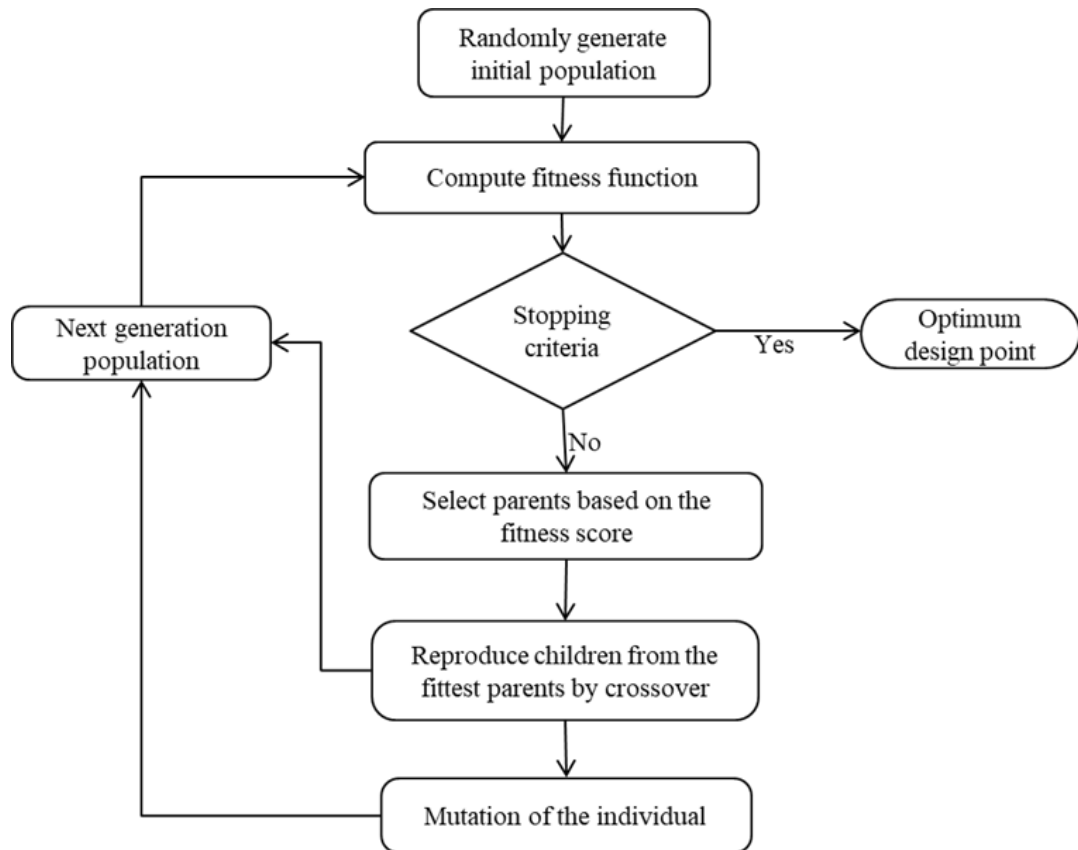


Figure 5.4. Procedure for optimization using GA tool in matlab.

5.5 RESULTS AND DISCUSSION

Once the RBFNN model is established, the model can be used to evaluate η_s at any desired value of S , α and L/d within the design space. Before running the genetic algorithm for optimization, η_s is evaluated at $S = 0 - 0.7$, $\alpha = 15^\circ - 90^\circ$ and $L/d = 4 - 16$. The distribution of η_s obtained from RBFNN throughout the design space is shown in Figure 5.5. From the figure, it can be directly deduced that the maximum value of the objective function lies between $0.1 < S < 0.4$, $15^\circ < \alpha < 40^\circ$ and $L/d < 10$. The effect of L/d seems to have a minor effect on the objective function compared to S and α .

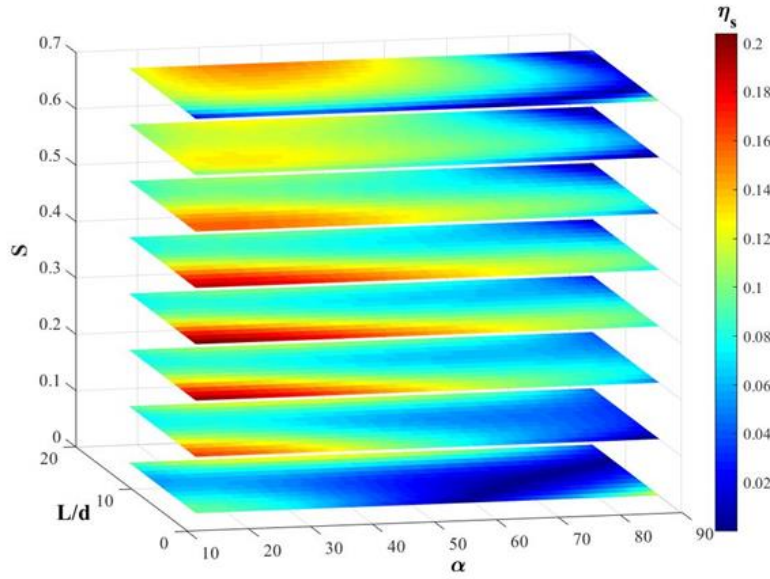


Figure 5.5. Distributions of the objective function within the design space of film cooling parameters used for optimization.

Also, it appears that there could be a secondary maximum of η_s at $S > 0.6$, $\alpha \approx 30^\circ$ and $L/d > 16$. However, the value of η_s seems to be less than the global maximum value. There is a possibility that η_s could peak again if S and L/d are increased further. But these points are situated outside the design space considered in this study; hence the ANN model would not be able to predict the η_s values with considerable accuracy. It is to be noted that $L/d > 16$ might be practically unfeasible. Also, when S goes beyond 0.7, it was observed from the previous chapter that the effectiveness peaks immediately after the hole exit and falls sharply to very low values. At very high swirl numbers, the downstream region might get exposed to high temperatures due to maximum deterioration of coolant concentration. Another difficulty associated with high swirl numbers is increase in heat transfer coefficient values. Hence the present study is limited to $S \leq 0.7$.

The GA has generated the optimized value for the design variables, which can produce maximum spatially averaged effectiveness. The resulting optimized geometrical parameter is compared with a reference case of $S = 0.168$, $\alpha = 30^\circ$ and $L/d = 8$. The optimum values of the design variables obtained from GA in the present study are $S = 0.32$, $\alpha = 19.3^\circ$ and $L/d = 4$.

Table 5.2. Comparison of η_s obtained from CFD and RBFNN model for reference and optimized geometries.

Geometry	S	α	L/d	η_s from CFD	η_s from ANN
Reference	0.168	30	8	0.089	0.099
Optimum	0.32	19.3	4	0.191	0.205
Increase in η_s				114 %	107 %

Table 5.2 compares the outputs of reference geometry with the optimized film cooling geometric configuration obtained from CFD solution as well as through the ANN model. It is found that there is an increase in spatially averaged effectiveness of more than 110% for an optimized film cooling geometrical configuration than the reference geometry considered. It can also be observed that the difference between η_s obtained from CFD and ANN is around 7%, which assures that the present RBFNN model is relatively reliable in predicting the high-fidelity CFD results.

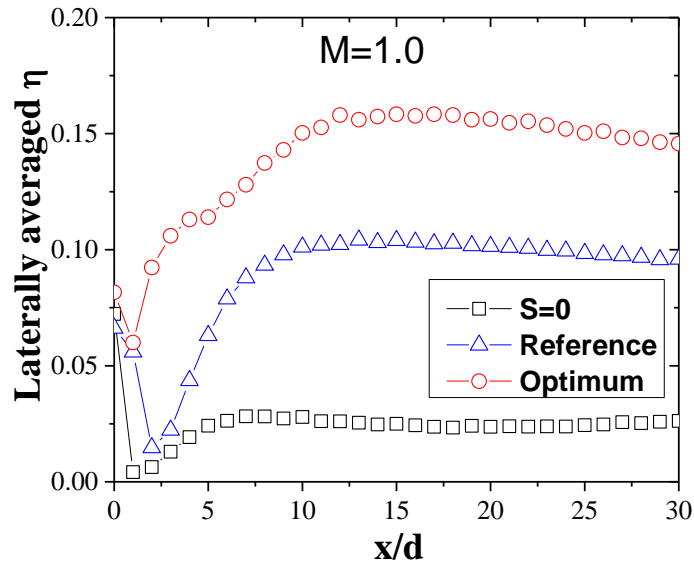


Figure 5.6. Comparison of laterally averaged effectiveness for the base case, reference geometry and optimized geometry.

Figure 5.6 compares the laterally averaged η distribution in case of optimized geometry and the reference geometry along with the non-swirl film cooling result. There is more than 50% higher effectiveness obtained for $x/d = 6$ to 30 in case of optimum geometry than the reference case and around 300% increment for $x/d < 5$.

When compared with the non-swirl case, there is a nearly 500% improvement observed.

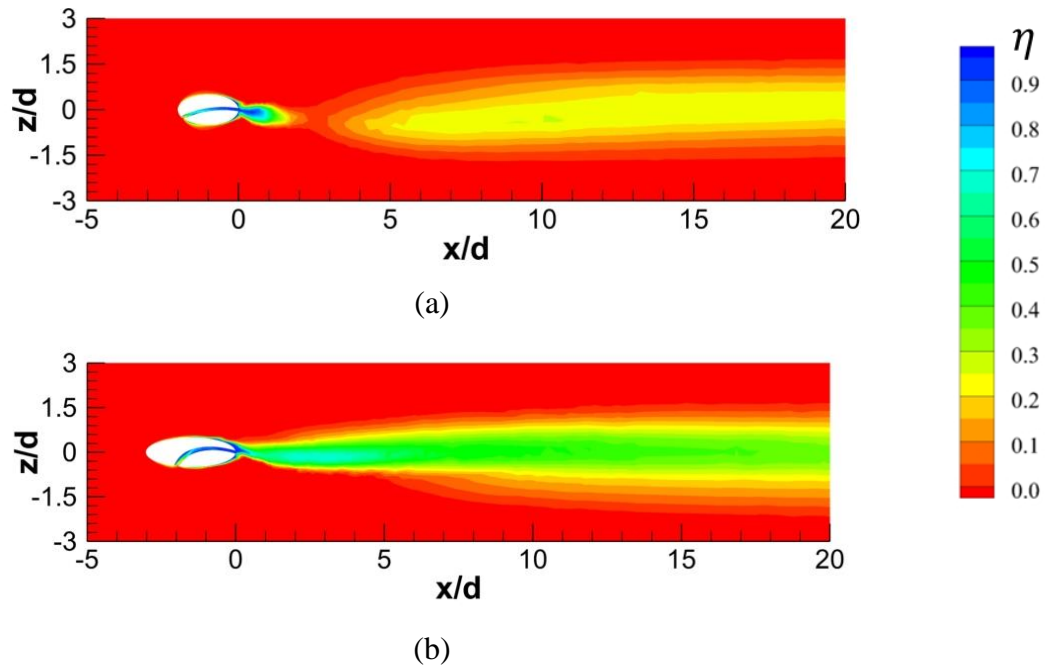


Figure 5.7. Lateral distribution of effectiveness on the plane at $y/d = 0$ (a) reference and (b) optimized geometry.

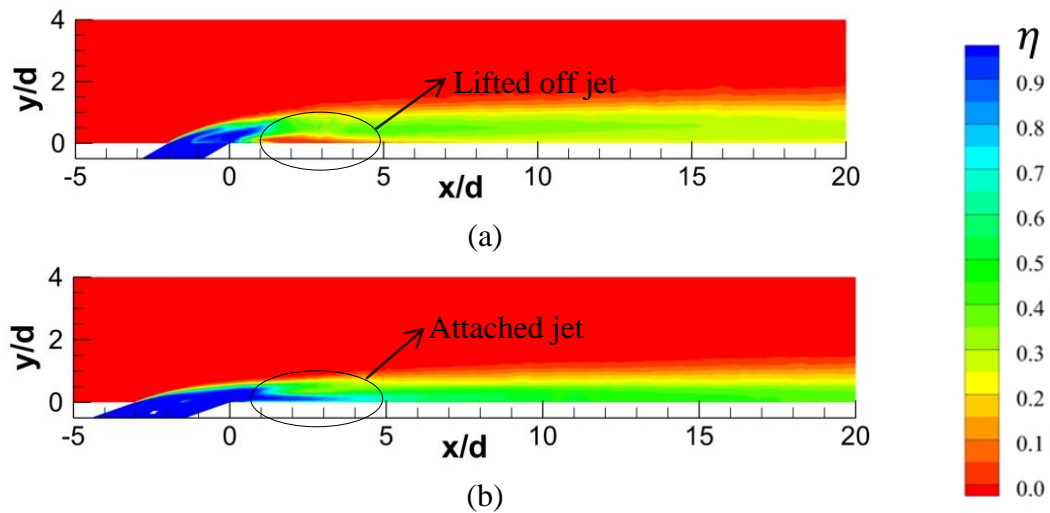
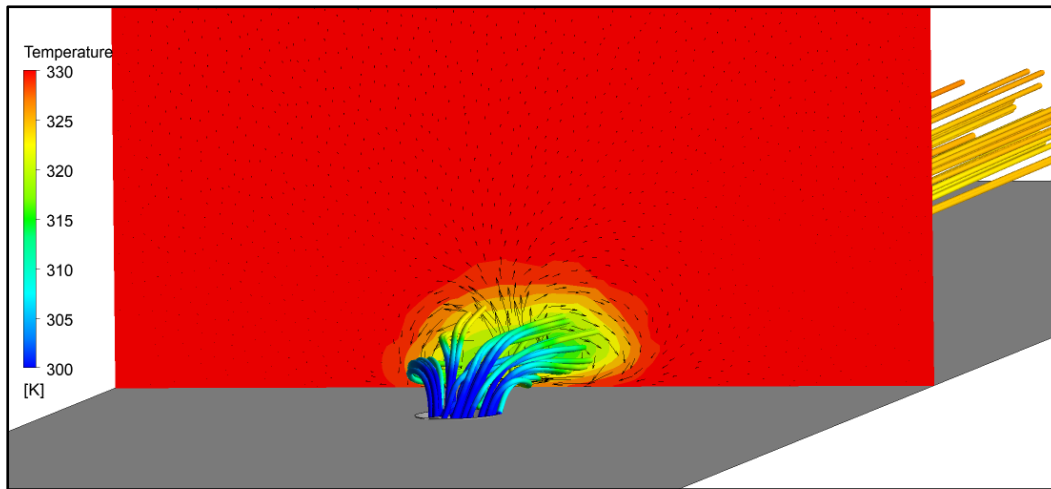


Figure 5.8. Effectiveness on the center plane (at $z/d = 0$) for (a) reference and (b) optimized geometry.

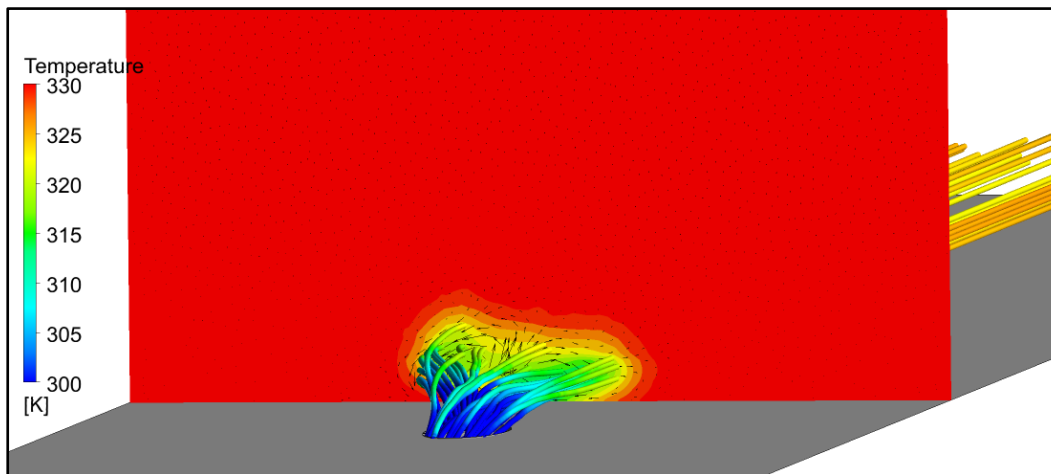
A local effectiveness distribution on the $x - z$ plane at $y/d = 0$ for reference geometry is compared with the optimized geometry in Figure 5.7. The optimized

geometry results in more coolant adherence over the surface, especially along the centerline. A weak coolant distribution in the case of reference geometry is observed from $x/d = 1$ to 4 which improves once the design is optimized. Surface effectiveness value for $x/d = 5$ to 20 and $z/d = -1$ to 1 was about 0.25 for the reference case, whereas the optimized case produced η of around 0.3 - 0.6. One major factor driving such improvement is the reduction in the height of coolant jet lift-off. It can be observed from Figure 5.8 that the coolant jet is slightly away from the surface from $x/d = 1$ to 4 for the reference geometry. As the coolant gets lifted off the surface, hot mainstream gas envelope the surface, reducing the effectiveness. Once the geometry is optimized, the jet lift-off disappears and keeps the coolant attached to the surface. Especially the effectiveness in the same region is maintained to be around 0.9. One more factor which is driving the coolant towards the surface might be the lower injection angle in the case of optimized geometry than in the reference case.

The coolant flow structure for reference and optimized cases are shown in Figure 5.9 in terms of streamlines emerging from the film hole exit. The streamlines are color contoured by the global temperature scale. Velocity vectors and temperature contour are shown on a plane normal to the coolant flow at $x/d = 5$. A major observation from the figure is that there is an increase in lateral deviation of the streamlines in the case of optimized geometry than in the reference case. This might be due to the higher swirl intensity of the coolant jet. As it can be observed, in the optimized case, the streamlines emerging from the lateral sides of the hole tend to diverge along z direction. Hence the coolant stream emerging from the windward side of the hole is readily deflected towards the wall by the mainstream resulting in more coolant adherence on the surface. Consequently, the CRVP will have less strength toward the center plane of symmetry ($z/d = 0$) which reduces the coolant jet lift-off and provides higher coolant coverage over the surface.



(a) Reference



(b) Optimized

Figure 5.9 Coolant streamlines and velocity vectors along with temperature contour on $y - z$ plane at $x/d = 5$.

5.6 CLOSURE

The present chapter discussed the optimization of film cooling geometrical parameters such as coolant swirl number, injection angle and length of the hole. One of the global optimization techniques known as Genetic Algorithm is used to obtain the optimum film cooling geometry while trying to maximize the film cooling effectiveness. The objective function for the optimization has been constructed using a radial basis function neural network. The ANN model is trained with 30 samples pertaining to different geometrical parameter combinations and additional 15 samples are used to test the network. Numerical simulations using ANSYS Fluent were

conducted for these instances to obtain a spatially averaged effectiveness. It was found that a swirl number of 0.32, injection angle of 19.3° and a hole length to diameter ratio of 4 is the optimum geometrical combination that can deliver maximum effectiveness. More than a 110% increase in the effectiveness was observed for optimized geometry than the reference case having swirl number, injection angle and length to diameter ratio of 0.168, 30° and 8, respectively.

[Equation Chapter \(Next\) Section 1](#)

CHAPTER 6

SIMULTANEOUS ESTIMATION OF REFERENCE TEMPERATURE AND HEAT TRANSFER COEFFICIENT IN TRANSIENT FILM COOLING

6.1 INTRODUCTION

It is observed from the literature that a transient film cooling analysis can quickly predict both the heat transfer coefficient and reference temperature. Also, a significant advantage of conducting a transient study is that it can replace the two-test strategy of steady-state analysis. The existing transient studies have also followed the two-test method due to difficulties associated with the data reduction technique. Hence, developing a data reduction technique for the transient analysis of film cooling situations using a single test approach is necessary. Based on the above observations, the present work aims to achieve a few objectives, such as conducting a transient analysis to evaluate boundary parameters for a film cooling problem. To develop an approach to obtain film cooling effectiveness and heat transfer coefficient using short-duration transient data from a single experiment that is accurate and easy to implement. Also, it is essential to study the effect of transient data on the solution approach.

Hence, in the present work, the feasibility of simultaneously estimating the convective heat transfer coefficient and reference temperature through a single transient experiment is attempted in the case of a film cooling situation. The novelty of the present work lies in the proposed data reduction method, which is based on the inverse heat conduction approach. This method can solve and evaluate multiple film cooling parameters using a single set of transient data. The proposed method utilizes the analytical solution of the transient one-dimensional semi-infinite heat conduction model as the forward solution. The inverse solution is obtained using an optimization technique known as the Levenberg-Marquardt algorithm. A conjugate numerical

simulation is performed in ANSYS Fluent to generate transient wall temperature data required for the analysis. The film cooling parameters, h and T_{ref} are evaluated through an in-house MatLab code using transient data obtained from the simulations. Results from the present technique are validated with the results from the steady-state numerical simulation for blowing ratios of 0.5, 0.8, and 1.0. A brief discussion on the sensitivity of input data on the current solution approach in the case of parameter estimation is also presented.

6.2 ONE-DIMENSIONAL SEMI-INFINITE ANALYSIS

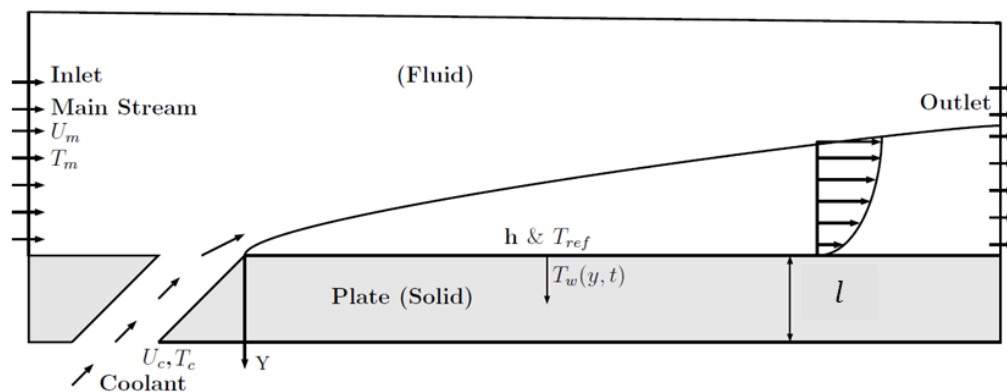


Figure 6.1. One-dimensional heat transfer across a film cooled semi-infinite flat plate.

Figure 6.1 shows a typical film cooling arrangement over a flat surface. The aim here is to calculate the local fluid temperature (T_{ref}) and heat transfer coefficient (h) over the surface using the transient temperature measured at $y = 0$. This problem can be simplified by assuming the plate as a semi-infinite model with one-dimensional heat conduction across the thickness (l) of the plate. But the semi-infinite assumption is valid only for a short duration such that the temperature change on the top surface $y = 0$ should not affect the bottom surface temperature (i.e., at $y = l$, $T_w = T_i$) (Vogel et al. 2003).

The general governing equation for one-dimensional transient heat conduction through a semi-infinite flat plate with a convection boundary condition on one side can be written as,

$$\delta \frac{\partial^2 T}{\partial y^2} = \frac{1}{\sigma} \frac{\partial T}{\partial t} \quad (6.1)$$

The boundary conditions are as follows,

$$\text{at } y=0, -\delta \frac{\partial T}{\partial y} = h (T_w - T_{ref}) \quad (6.2)$$

$$\text{as } y \rightarrow \infty, T = T_i \quad (6.3)$$

The reference temperature in Equation (6.1), T_{ref} , is the mixture temperature of the mainstream and coolant over the film cooled surface, and T_w is the temperature of the plate.

The initial condition is given by,

$$\text{at } t = 0, T = T_i \quad (6.4)$$

The solution for Equation (6.1) using the prescribed initial and boundary conditions is given by (Hahn and Özisik, 2012),

$$\frac{T_w(y,t) - T_i}{T_{ref} - T_i} = \text{erfc}\left(\frac{y}{2\sqrt{\sigma t}}\right) - \exp\left(\frac{hy}{\delta} + \frac{h^2\sigma t}{\delta^2}\right) \text{erfc}\left(\frac{y}{2\sqrt{\sigma t}} + \frac{h\sqrt{\sigma t}}{\delta}\right) \quad (6.5)$$

where δ and σ are the thermal diffusivity and thermal conductivity of the plate material, respectively.

In film cooling situations, a coolant stream is injected into the mainstream, as represented in Figure 6.1. Hence the fluid temperature downstream of injection is a mixture of two fluid streams. This mixture temperature is unknown and has to be evaluated, which is attributed as reference temperature (T_{ref}). The reference temperature is highly localized with respect to the location and depends on the mixing phenomena of hot and cold fluids. In case of film cooling arrangement, T_{ref} is represented in terms of a non-dimensional quantity known as effectiveness (η), which is defined as (Goldstein et al. 1968b),

$$\eta = \frac{T_{ref} - T_m}{T_c - T_m} \quad (6.6)$$

where T_c and T_m are the temperatures of the coolant and mainstream, respectively.

Equation (6.5) has two unknowns (h and T_{ref}) which necessitates one more additional equation to evaluate the two parameters. Since only one equation is

available, the solution for this problem can be obtained through an iterative technique with nonlinear least squares regression.

6.3 LEVENBERG-MARQUARDT ALGORITHM

The unknown boundary parameters, h and T_{ref} in Equation (6.5) is evaluated using one of the robust optimization technique known as the Levenberg-Marquardt algorithm (LMA) in the present study. LMA is an iterative approach that evaluates the optimum values of unknown parameters by minimizing the variance between the measured and the estimated temperatures.

Firstly the inverse problem needs to be constructed by defining an objective function (Z) defined as the summation of the squared difference between the measured and the estimated temperatures (Ozisik 2018), which can be written as,

$$Z(p) = \sum_{i=1}^I [Y_i - T_i(p)]^2 \quad (6.7)$$

where Y and T are the measured and estimated temperatures at a particular location (x/d) and the subscript $i=1, 2, 3, 4, \dots, I$. The estimated temperature values are obtained by solving Equation (6.5). The term p refers to the unknown parameters, T_{ref} and h in the present case. The objective function Z is in the form of ordinary least squares norm. In order to minimize the objective function, the derivatives of Equation (6.7) with respect to the unknown parameters need to be evaluated and equated to zero (Ozisik 2018).

$$\frac{\partial Z(p)}{\partial p} = 0 \quad (6.8)$$

Equation (6.8) can be represented in the form of matrix notation as follows,

$$-2J(p)[Y - T(p)] = 0 \quad (6.9)$$

where, $J(p) = \frac{\partial T^T(p)}{\partial p}$ is known as Jacobian or the sensitivity coefficient,

which is defined as the rate of change of the dependent variable with respect to the unknown parameters. In the present work, the sensitivity coefficients are evaluated by the direct differentiation of Equation (6.5) with respect to h and T_{ref} . The expressions obtained to calculate the sensitivity coefficients are as follows,

$$J(T_{ref}) = \frac{\partial T_w}{\partial T_{ref}} = \operatorname{erfc}\left(\frac{y}{\sqrt{4\sigma t}}\right) - \exp\left(\frac{hy}{\delta} + \frac{h^2\sigma t}{\delta^2}\right) \operatorname{erfc}\left(\frac{y}{\sqrt{4\sigma t}} + \sqrt{\frac{h^2\sigma t}{\delta^2}}\right) \quad (6.10)$$

$$J(h) = \frac{\partial T_w}{\partial h} = (T_i - T_{ref}) \left[\begin{array}{l} \left(\frac{y}{\delta} + \frac{2h\sigma t}{\delta^2}\right) \exp\left(\frac{hy}{\delta} + \frac{h^2\sigma t}{\delta^2}\right) \operatorname{erfc}\left(\frac{y}{\sqrt{4\sigma t}} + \sqrt{\frac{h^2\sigma t}{\delta^2}}\right) \\ -\sqrt{\frac{4\sigma t}{\pi\delta^2}} \exp\left\{\frac{hy}{\delta} + \frac{h^2\sigma t}{\delta^2} - \left(\frac{y}{\sqrt{4\sigma t}} + \sqrt{\frac{h^2\sigma t}{\delta^2}}\right)^2\right\} \end{array} \right] \quad (6.11)$$

The inverse problem becomes nonlinear if the Jacobian has a functional dependency on the unknown parameters. The solution to Equation (6.9) is obtained through an iterative procedure. Here the vector $T(p)$ is linearized using the Taylor series of expansion with respect to iteration κ as,

$$T(p) = T(p^\kappa) + J(p^\kappa)(p - p^\kappa) \quad (6.12)$$

Substituting the Equation (6.12) in Equation (6.9) and after some rearrangement yields the following expression for the unknown parameters p ,

$$p^{\kappa+1} = p^\kappa + \left[(J^\kappa)^T J^\kappa \right]^{-1} (J^\kappa)^T [Y - T(p^\kappa)] \quad (6.13)$$

Equation (6.13) is known as Gauss-Newton method. When $|J^T J|$ in Equation (6.13) becomes very small or zero, the inverse problem becomes ill-conditioned, and the parameter estimation is impossible. This difficulty has been overcome by introducing a positive scalar known as damping parameter (λ) to Equation (6.13) as,

$$p^{\kappa+1} = p^\kappa + \left[(J^\kappa)^T J^\kappa + \lambda^\kappa \Omega^\kappa \right]^{-1} (J^\kappa)^T [Y - T(p^\kappa)] \quad (6.14)$$

The Equation (6.14) is known as Levenberg-Marquardt method. The term Ω is a diagonal matrix calculated as,

$$\Omega^\kappa = \operatorname{diag} \left[(J^\kappa)^T J^\kappa \right] \quad (6.15)$$

The value of the damping parameter, λ , used in Equation (6.14), is made large during the initial iterations so that the oscillations due to ill-conditioning will be damped, and the solution tends to the steepest descent method. As the iteration

progresses, the value of λ will be reduced, and the solution follows the Gauss-Newton method. The stopping criteria for the iteration are given by,

$$|p^{\kappa+1} - p^{\kappa}| < 10^{-3} \quad (6.16)$$

$$|Z(p^{\kappa+1})| < 10^{-3} \quad (6.17)$$

The flow chart of the in-house MatLab code to find the unknown film cooling parameters using the present IHCP technique is given in Figure 6.2.

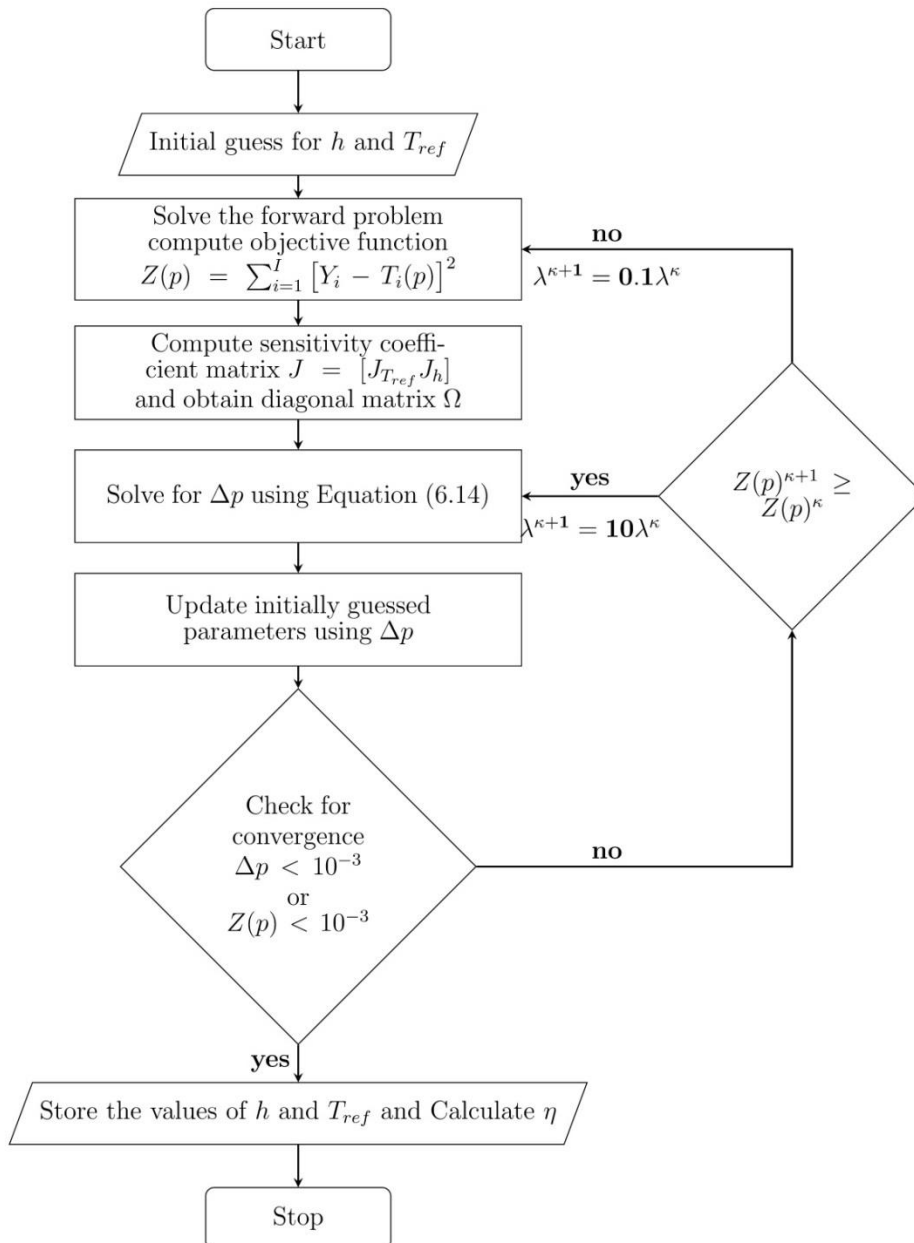


Figure 6.2. Flow chart of the present inverse algorithm for the estimation of film cooling parameters.

6.4 EVALUATION OF TRANSIENT TEMPERATURE DATA

The transient surface temperature data required for the present IHCP technique is obtained from a three-dimensional numerical simulation using ANSYS Fluent. The geometrical parameters of the computational domain are specified by following the experimental work of Sinha et al. (1991). Figure 6.3 shows the three-dimensional geometry of the computational domain and Figure 6.4 shows a section of the computational domain taken at the center plane.

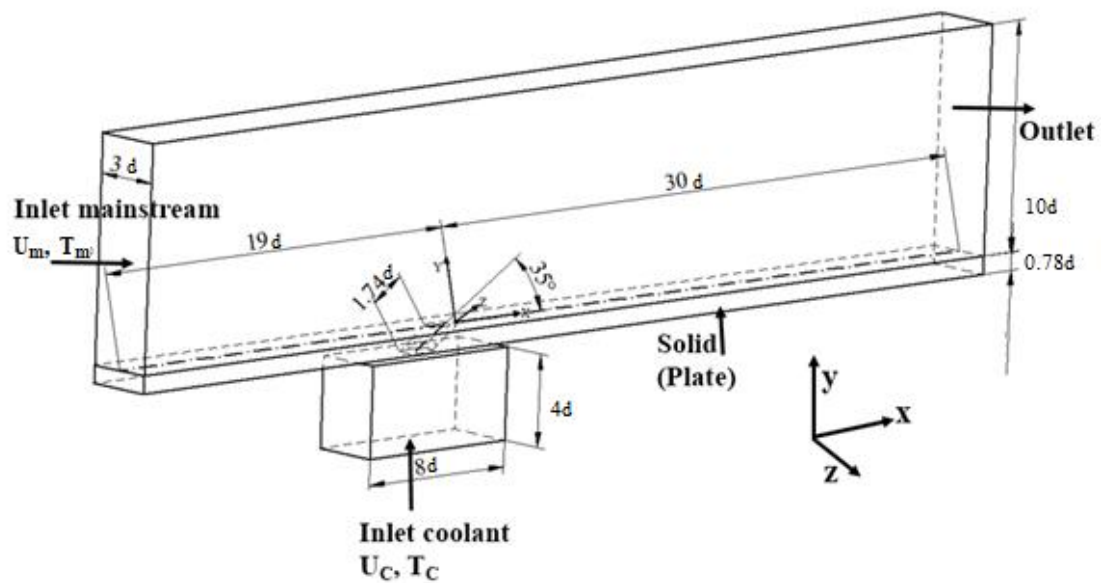


Figure 6.3. 3D Computational domain highlighting the solid-fluid interface to obtain transient surface temperature data using conjugate heat transfer solution.

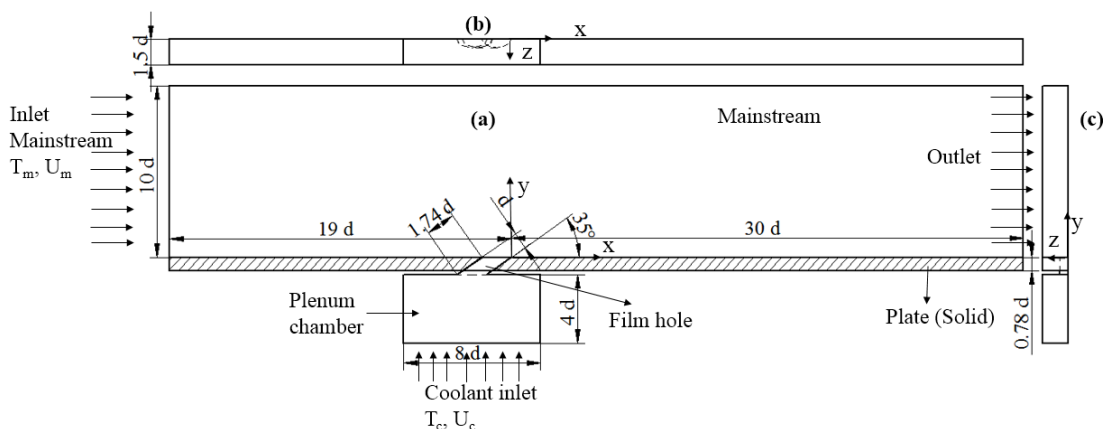


Figure 6.4. A 2D representation of the computational domain used for transient analysis film cooling over a flat surface. (a) Front sectional view at $z/d = 0$, (b) Top view, and (c) Side view.

The dimensions are normalized using the film cooling hole diameter, d . The computational domain divides into solid and fluid regions. The computational domain is divided into a solid region made up of film cooled plate with an inclined hole and a fluid region which contains a mainstream, a plenum chamber, and the fluid inside the film hole. Mainstream at higher temperatures enters and exits the domain through the inlet and outlet boundary surfaces, as shown in Figure 6.4. At the inlet of the mainstream, velocity and temperature values are specified and at the outlet, zero relative pressure boundary condition has been set. The coolant enters through the bottom surface of the plenum chamber and exits through the film hole into the mainstream. At the coolant inlet, temperature and mass fluxes are specified. The mass flux is calculated based on the blowing ratio. Symmetry boundary condition is applied on the lateral sides of the mainstream and the plenum chamber. The bottom and the lateral surfaces of the plate are insulated. Table 6.1 shows the details of the input conditions used in the present simulation.

Table 6.1. Input conditions used in the present simulation.

Parameter	Values
Diameter of the jet, d	12.7 mm
Angle of injection, α	35°
Pitch, P/d	3
Length of hole, L/d	1.74
Mainstream velocity, U_m	20 m/s
Mainstream temperature, T_m	600K
Jet Temperature, T_c	300K
No. of hole	1
Blowing Ratio (M)	0.5 and 1.0
Density Ratio ($D.R$)	2.0
Thickness of the plate	10 mm

The computational domain is discretized using unstructured tetrahedron elements. Inflation layers are generated above the film cooling surface with a y^+ value approximately equal to 15. Figure 6.5 depicts the results of a grid independence

analysis for four different mesh refinements of 1.8, 2.5, 3.9, and 6.8 million elements. It can be observed from the figure that the deviation in the computed effectiveness is minimal for all mesh configurations. About 2% variation in the effectiveness is observed for $2 < x/d < 4$, and in the rest of the locations, the deviation lies below 1%. The average deviation between 1.8 and 6.8 million elements in the computed effectiveness is around 0.7%. Hence all further simulations are conducted for mesh configuration having 2.5 million elements. This specific mesh configuration ensures better spatial distribution while maintaining a reasonable computation time.

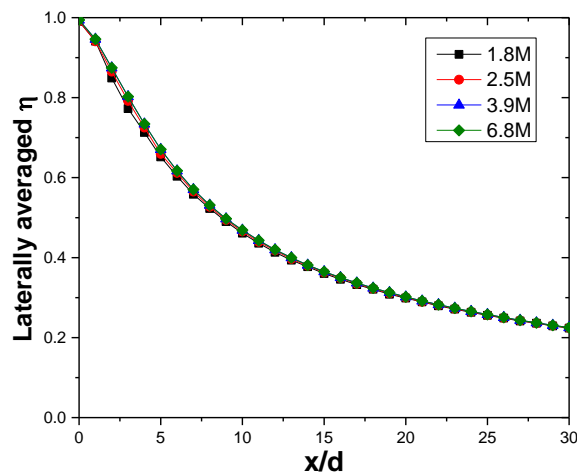


Figure 6.5. Effect of mesh refinements on computed effectiveness by numerical simulation for $M = 0.5$.

A three-dimensional Reynolds Averaged Navier-Stokes (RANS) equations are solved along with standard $k - \epsilon$ turbulence model with standard wall functions. The convective components are discretized using a second-order upwind interpolation approach, and pressure-velocity coupling is accomplished using the SIMPLE algorithm. Also, temporal discretization is achieved through a second-order implicit scheme. The transient simulation is carried out for about 200 seconds with a time step of 0.01 seconds.

The numerical simulation considers a film cooling plate with a thickness (L) of 10mm. The thermo-physical properties of the plate materials are similar to the properties of Polymethylmethacrylate (PMMA) or acrylic material. The thermal conductivity (δ) and thermal diffusivity (σ) of the plate material are 0.187 W/m-K and 1.076×10^{-7} m²/s, respectively. Due to its low thermal conductivity, the acrylic plate allows transient temperature measurements for a longer duration without

violating the semi-infinite assumption. Most of the studies on transient film cooling have also used an acrylic plate for transient surface temperature measurements (Ekkad et al. 2004). In the present work, the transient wall temperature data is stored every 0.1 seconds for $x/d = 0 - 30$. The simulation is started with an initial temperature of 300K for the solid domain such that at $t = 0$, $T = T_i$.

The plate can be assumed semi-infinite only if it satisfies the condition $T = T_i$ at $y = l$. The diffusive time constant $\left(\tau_{diff} \approx \frac{l^2}{4\sigma t}\right)$ evaluates the time taken by the thermal wave to travel from the top surface ($y = 0$) to the bottom surface ($y = l$) (Nellis and Klein 2009). For the PMMA material used in the present simulations, the τ_{diff} is obtained around 232 seconds. The present IHCP technique has used transient data of 20-100 seconds for parameter estimation. Hence the validity of the semi-infinite assumption can be justified.

The two fluid streams, mainstream and coolant, have different temperatures in the present case. Hence the variation of thermophysical parameters of the fluid corresponding to temperature is included while setting up the problem in Fluent. The density variation of air is included based on the assumption of an incompressible ideal gas. Other properties such as thermal conductivity, dynamic viscosity, and specific heat are given as a function of temperature (Incropera et al. 2006). A third-order polynomial curve is fitted for these three parameters with temperature and the coefficients of the curve fit equation are given as input to the fluent while defining the material properties of the fluid. The third-order polynomial equation used for the curve fit in the present study is written as,

$$f(T) = a_0 + a_1T + a_2T^2 + a_3T^3 \quad (6.18)$$

The coefficients of the polynomial equation are given in Table 6.2.

Table 6.2. Coefficients of the curve fit equation for the variation of fluid properties with respect to temperature.

$f(T)$	a_0	a_1	a_2	a_3
$\delta_a(T)$	3.6404×10^{-4}	9.8947×10^{-5}	-4.5763×10^{-8}	1.3974×10^{-11}
$\mu(T)$	1.8115×10^{-6}	6.4977×10^{-8}	-3.5017×10^{-11}	9.7110×10^{-15}
$C_p(T)$	961.29	9.5836×10^{-2}	1.3649×10^{-4}	-5.7898×10^{-8}

6.5 RESULTS FROM THE TRANSIENT ANALYSIS

6.5.1 Validation of the numerical setup and the present IHCP method

At first, the numerical solution results are validated against the experimental results of Sinha et al. (1991). A steady-state simulation is carried out for blowing ratios of 0.5 and 1.0. Figure 6.6 compares the centerline effectiveness obtained from the steady-state simulation with the experimental results of Sinha et al. (1991) for $M = 0.5$ and 1.0. There is a close agreement with the experimental results that exists up to $x/d = 15$ with an average error of around 5%. However, the deviation gradually increases further downstream ($x/d > 15$), resulting in an average error of 19%. At $M = 1.0$ the deviation is observed to be around 8% up to $x/d = 30$.

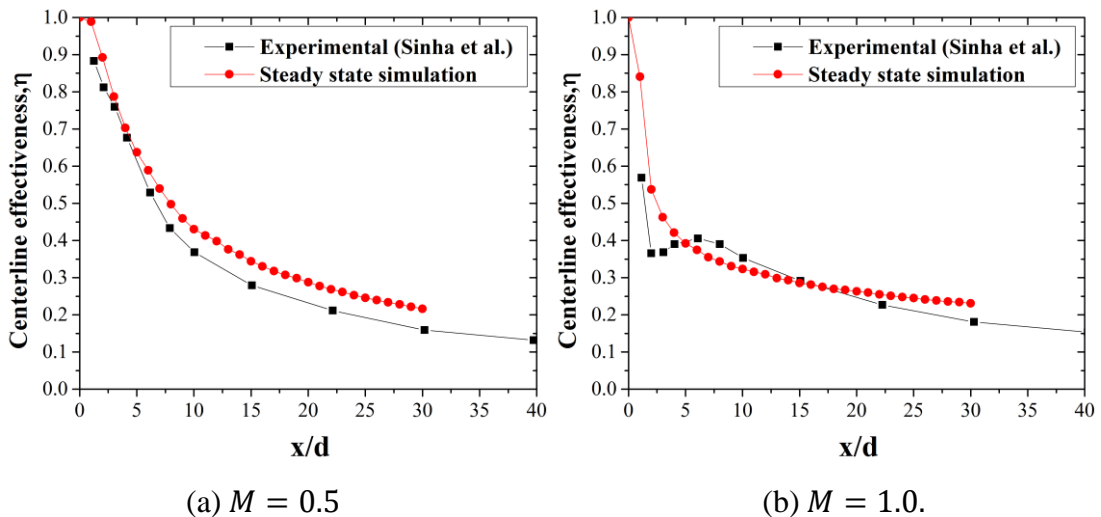


Figure 6.6. Validation of the present numerical results with the literature.

The experimental result for $M = 1.0$ shows a sudden drop in the effectiveness values at $x/d = 2.5$ and increases slightly till $x/d = 7$, and then decreases further downstream. This is due to jet separation and reattachment, which occurs at a blowing ratio of 1. In film cooling, the jet-mainstream interaction creates a distinctive flow feature known as counter-rotating vortex pair (CRVP). The lift-off of the coolant jet is mostly caused by the presence of CRVP, whose strength rises as the blowing ratio increases. Hence, exact prediction of film cooling behavior in numerical simulation becomes extremely difficult. It appears in the present simulation the jet separation and

the reattachment phenomena are not captured precisely. However, an overall film cooling behavior is roughly apprehended.

Previous numerical works have also observed the downstream deviation of numerical results from the experimental results. One primary reason is attributed to the isotropic turbulence viscosity assumption causing an overprediction in the computed centerline effectiveness (Harrison and Bogard 2008b). Also, it was reported that the sources of errors could be the possibility of jet skewness (Walters and Leylek 1996), lateral conduction errors during the experiments (Kapadia et al. 2003), use of tetrahedral meshes and inappropriate wall functions (Zhang and Hassan 2006).

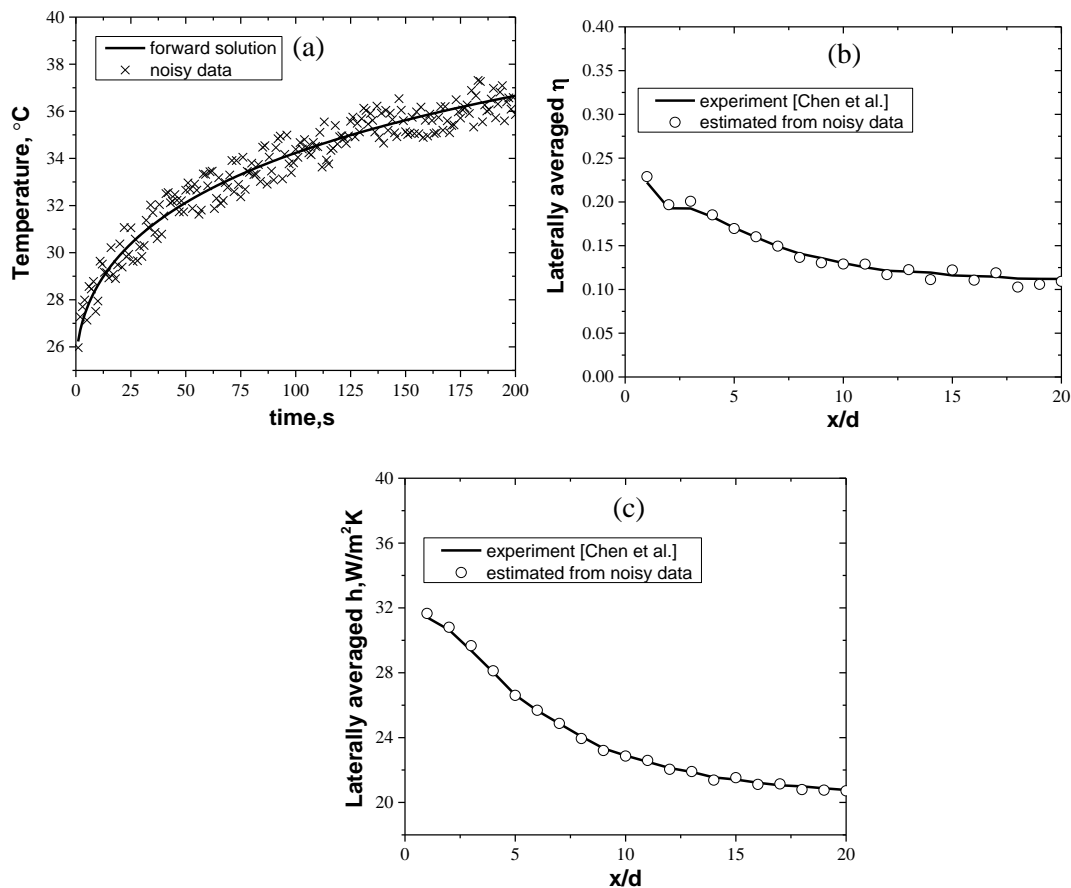


Figure 6.7. (a) Transient temperature data generated from the forward solution with additional random noise of $\pm 1K$, comparison of estimated parameters using noisy data, (b) effectiveness, (c) heat transfer coefficient.

A validation of the present IHCP method is performed using the experimentally obtained h and T_{ref} values from Chen et al. (2001) for $M = 0.5$. The values of h and T_{ref} from Chen et al. (2001) are used to generate transient

temperature from one-dimensional semi-infinite solution given in Equation (6.5). A random noise of ± 1 K is introduced to the transient wall temperature generated using Equation (6.5) to obtain noisy data. Then from the present IHCP technique, the effectiveness and heat transfer coefficients were estimated using the noisy data. Figure 6.7(a) shows the transient temperature generated from the solution of direct problem at $x/d = 10$ along with externally added random noise of ± 1 K. Figure 6.7(b) and Figure 6.7(c) shows the comparison of estimated parameter values with corresponding experimental values. It was found that the present IHCP technique has estimated the parameters accurately with an average error of less than 1% from the noisy data. It is observed that higher noise levels increase the deviation in the estimated parameters. When a noise of ± 5 K is introduced to the input data, the estimated parameters have deviated with more than 10% error.

6.5.2 Linear fit method

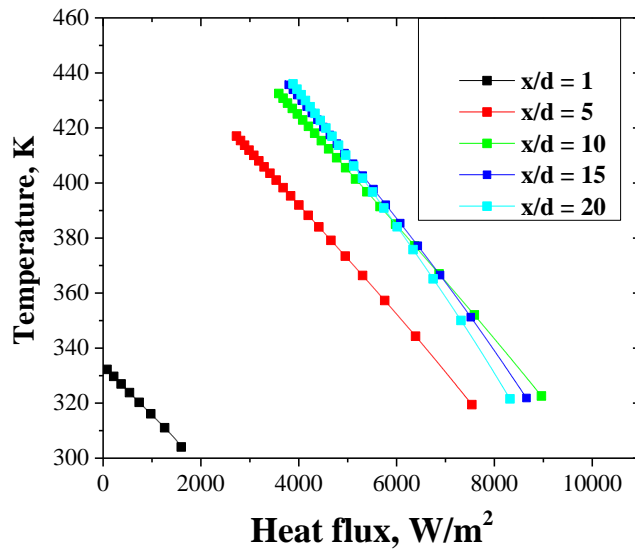


Figure 6.8. Linearity between wall temperature and heat flux.

When the transient surface heat flux data is available, it is possible to estimate the unknown film cooling parameters using the linear relation between the wall temperature and the surface heat flux data. The linear relation can be obtained using Newton's law of cooling as (Kadam et al. 2020),

$$q''(t) = h(T_w(t) - T_{ref}) \quad (6.19)$$

This equation can be rewritten as,

$$T_w(t) = \frac{q''(t)}{h} + T_{ref} \quad (6.20)$$

The Equation (6.20) is in the form of $y = mx + c$, where the slope, $m = 1/h$ and the y-intercept is T_{ref} . By plotting transient heat flux vs wall temperature, both the heat transfer coefficient and the reference temperature can be obtained by finding the slope and the y-intercept respectively. Figure 6.8 shows the linear relation between wall temperature and heat flux at different x/d by plotting $q''(t)$ vs $T_{wall}(t)$.

6.5.3 Effectiveness

Laterally averaged effectiveness estimated from the present IHCP technique for blowing ratios of 0.5, 0.8 and 1.0 are shown in Figure 6.9. The blowing ratio determines the jet direction, which influences the coolant distribution and affects the effectiveness. At low blowing ratio ($M = 0.5$), the $\bar{\eta}$ reduces gradually along the length. As M increases, the coolant jet issues out with more momentum, causing low values of $\bar{\eta}$. It can be noted from the figure that the rate of reduction of $\bar{\eta}$ is less for $M = 1$ than that of $M = 0.5$. At $M = 1$, $\bar{\eta}$ drastically reduces for $x/d < 5$ and thereafter appears to have a negligible variation along x/d .

The estimated $\bar{\eta}$ values are compared with the steady-state simulation results for corresponding blowing ratios. The film cooling surface is insulated in steady-state analysis to evaluate its effectiveness. The adiabatic wall temperature yields the local fluid temperature at steady-state. Figure 6.9 also presents the $\bar{\eta}$ obtained using the method of linear fit as discussed in the previous section. It is observed that $\bar{\eta}$ values estimated using the present IHCP technique are in good agreement with steady-state simulation results as well as using the method of linear fit. The average deviation between the steady-state and the present IHCP solution is around 6% - 7% for all blowing ratios. The estimated values are in close agreement till $x/d \approx 7$ with an error less than 5% and slightly increase there after. Results from the IHCP solution almost coincide with the output of the linear fit method. The deviation between the linear fit method and steady-state analysis is around 8% for $M = 0.5$ and 0.8, whereas for $M = 1.0$, the error is more than 12%. A major disadvantage of the linear fit method is that it requires transient heat flux values along with wall temperature to compute the

parameters. The accurate measurement of surface heat flux is very challenging; hence, the linear fit method might produce results with higher uncertainty.

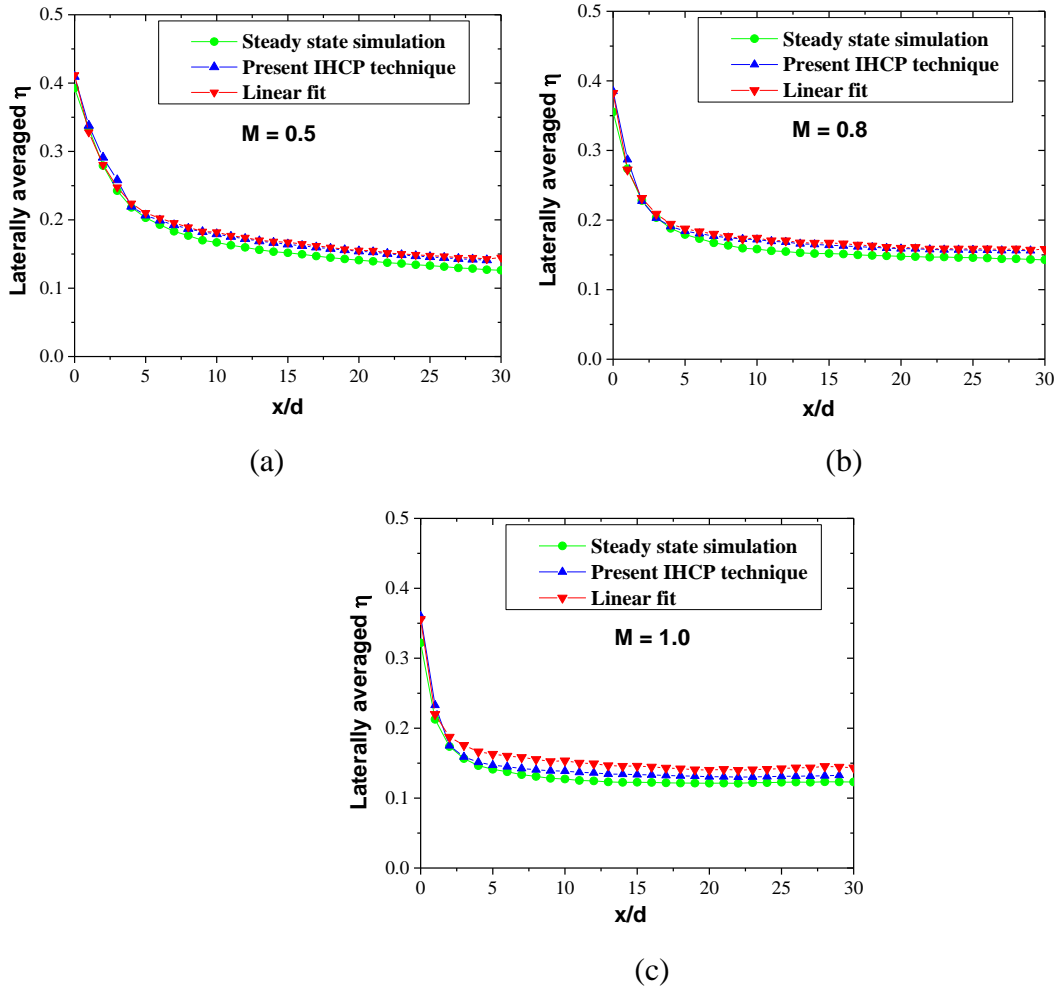


Figure 6.9. Comparison of laterally averaged effectiveness obtained using different techniques for (a) $M = 0.5$, (b) $M = 0.8$ and (c) $M = 1.0$.

6.5.4 Sensitivity analysis

To avoid the ill-conditioned problem, the values of sensitivity coefficients must have large magnitudes (Ozisik 2018). Figure 6.10 shows the sensitivity coefficient values for reference temperature and heat transfer coefficient with time. The sensitivity coefficients can be calculated either by direct differentiation or numerical differentiation. If the forward solution is simple, then direct differentiation is possible. In the present work analytical solution to the one-dimensional heat conduction equation is used as a forward model. Instead, the sensitivity coefficients may have to be evaluated using numerical differentiation if a three-dimensional

governing equation is considered. However, numerical differentiation is computationally expensive and less accurate than direct differentiation. In such situations, the use of other optimization techniques which are independent of Jacobian evaluation can be implemented.

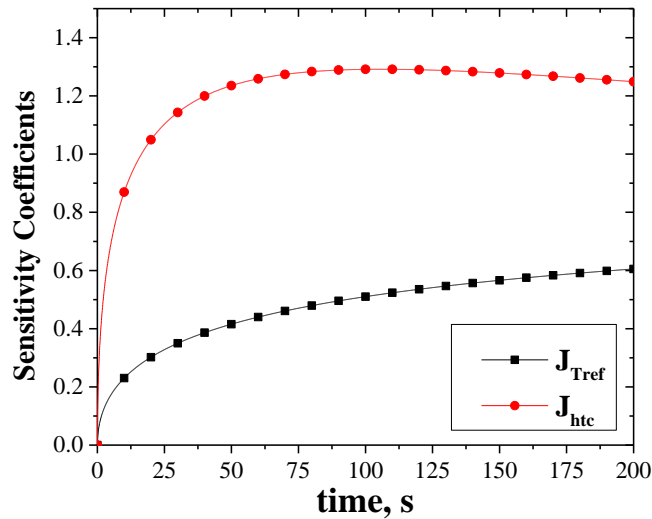


Figure 6.10. Sensitivity coefficients for T_{ref} and h with time at $x/d = 10$ for $M = 1.0$.

In the present case, the values of $J_{T_{ref}}$ and J_h are calculated using Equations (6.10) and (6.11), respectively. Both $J_{T_{ref}}$ and J_h values are increasing with time, but $J_{T_{ref}}$ values are lower than J_h values. This indicates that the estimated temperature is less sensitive to change in reference temperature than the heat transfer coefficient, which makes the estimation of effectiveness more difficult than h . An immediate conclusion is that the least square error between the exact and estimated values for heat transfer coefficient would be less than the effectiveness. Also, from Figure 6.10 it is noted that the magnitudes of sensitivity coefficients are very small during the initial time. Hence considering transient data for a concise duration may lead to inaccurate parameter estimation. It can be observed from the Equation (6.10) and (6.11) that $J_{T_{ref}}$ is dependent only on estimated h , but J_h is a function of both T_{ref} and h values indicating both the parameters are linearly dependent.

The determinant of $J^T J$ is plotted with time in Figure 6.11 to compare the effect of sampling rate. The transient data is sampled with a time interval of 0.1, 1, 5 and 10 seconds. The figure indicates a steep rise in the magnitude of $|J^T J|$ up to

around 20 seconds and gradually increases further. Hence the transient data considered below this point would increase the uncertainty in the parameter estimation. One of the significant observations from the figure is that higher values of $|J^T J|$ can be obtained by increasing the rate of sampling. Hence it can be concluded that, even with a short duration of the transient experiment, the parameter estimation uncertainty can be reduced using a higher sampling rate.

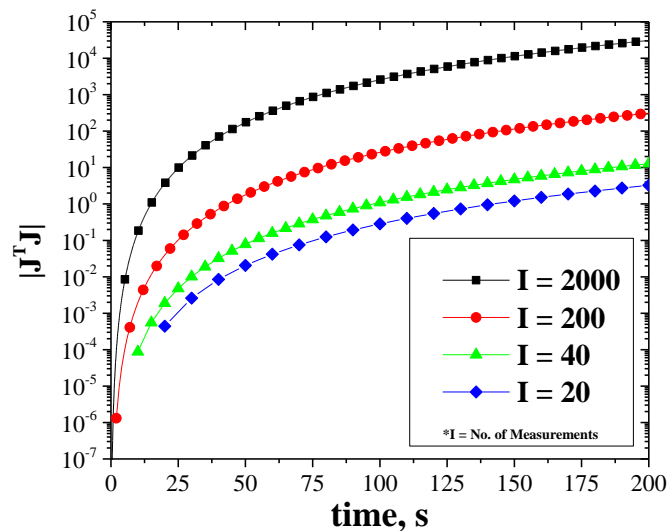


Figure 6.11. Determinant of sensitivity coefficients with time at $x/d = 10$ for $M = 1.0$.

The optimization algorithm can be successful only if it is able to find the global maximum or minimum. There could be a possibility of multiple minimums existing in the variables domain. Plotting the objective function inside the parameter space will provide information on the existence of such conditions. The objective function (Equation (6.7)) is evaluated at multiple locations on the parameter space of h and T_{ref} . The distribution of the objective function in terms of a three-dimensional contour is presented in Figure 6.12 for the case of $M = 1.0$ at $x/d = 10$. It can be seen from the figure that, if the initial guess lies far away from the optimum value, the objective function reduces exponentially. When the algorithm reaches near the optimum value, the rate minimization of the objective function diminishes. It is observed that the objective function distribution did not result in multiple peaks and valleys. Instead, the global minimum appears to exist inside a banded valley, and the present method proves to be very efficient in finding the global minimum.

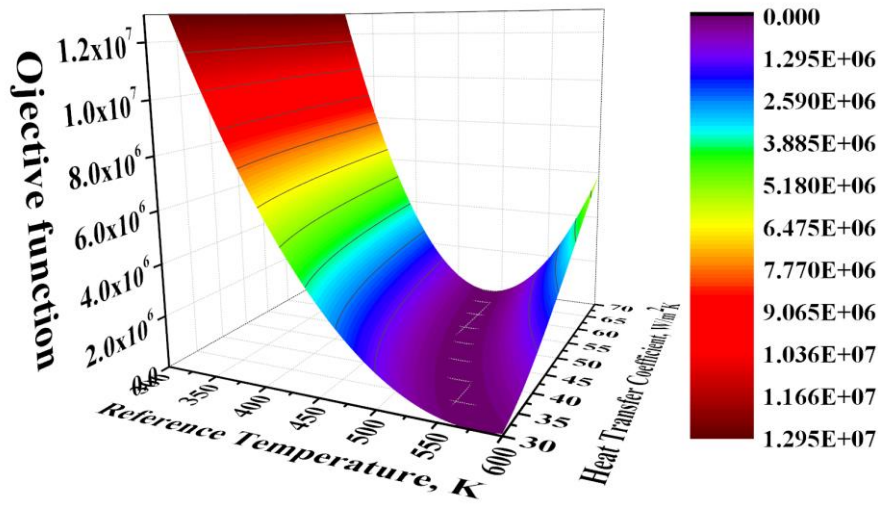


Figure 6.12. Three-dimensional distribution of objective function.

6.5.5 Heat transfer coefficient

The film cooling heat transfer coefficient is represented by normalizing it using the HTC values obtained for flat plate with no coolant injection (h_0). Therefore, it is essential to calculate the heat transfer coefficient for a non-film cooling flat plate case. A steady-state numerical simulation is performed for this particular case by specifying a surface heat flux (q'') of 1000 W/m^2 throughout the plate. The plate dimensions are kept as that of the solid domain, as shown in Figure 6.4. In addition, h_0 is calculated using the Nusselt number correlation for a turbulent boundary layer over a flat plate with constant heat flux boundary condition (Incropera et al. 2006) as,

$$Nu = \frac{h_0 x}{\delta_a} = 0.0308 Re_x^{(4/5)} Pr^{(1/3)} \quad (6.21)$$

The fluid properties such as ρ , μ , and Pr in the case of correlation are evaluated at an average temperature using the property table available in Incropera et al. (2006). The average fluid temperature is calculated using free-stream temperature, and the average temperature of the wall subjected to a constant heat flux boundary condition obtained from steady-state simulation.

Now, heat transfer coefficient values for non-film cooling flat plate case are estimated from the present IHCP technique and validated with the steady-state numerical simulation results and the values obtained from the correlation given in

Equation (6.21). Therefore a conjugate transient numerical simulation is conducted and using the transient wall temperature data, h_0 values are estimated by employing the present IHCP approach. The linear fit method is also used to determine the h_0 . Figure 6.13 compares the heat transfer coefficient values obtained using the above-mentioned methods. The results of the various methodologies demonstrate an excellent agreement with each other, with an average deviation of less than 5%.

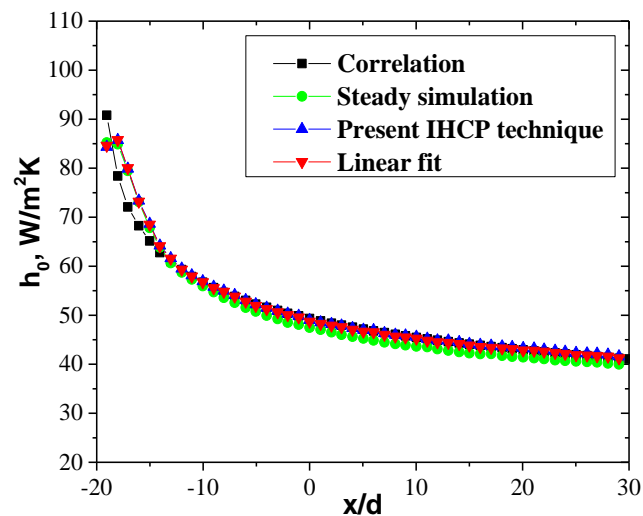


Figure 6.13. Heat transfer coefficient for a flat surface with no coolant injection.

Figure 6.14 shows the normalized values of laterally averaged film cooling heat transfer coefficient estimated using present IHCP algorithm at $M = 0.5, 0.8,$ and 1.0 . The figure also includes \bar{h} values obtained from the steady-state simulation and the linear fit method for comparison. A general trend of heat transfer coefficient in film cooling is that it increases with blowing ratio due to higher turbulence generated with an increase in injected coolant mass flux. Also, injection of coolant into the mainstream augments local turbulence levels. Hence, the steady-state simulation exhibits a higher heat transfer rate near the film hole exit and gradually reduces to a more or less constant value along the downstream. The estimated \bar{h} from the IHCP algorithm follows the steady-state simulation results, but it appears to have slightly deviated in the immediate downstream of the jet exit ($x/d < 5$). Further downstream (for $x/d > 5$), the laterally averaged heat transfer coefficient values from all the methods closely agree with each other. The average deviation between the estimated heat transfer coefficient using IHCP and steady-state simulation is observed to be

around 4% for all the blowing ratios studied. Results from the linear fit method also followed a similar trend as the IHCP solution with an error of around 3%.

In the region immediately downstream of injection, a maximum deviation of around 9% is observed between the IHCP results and steady-state simulation output. One primary cause of such an anomaly in the current transient approach might be the conjugate heat transfer solution employed in the present simulation. As the coolant passes through the film hole, the plate temperature surrounding the hole might reduce, causing less heat transfer coefficient values near the film hole exit. As a result, it can be concluded that the current method may be more realistic than a steady-state analysis since it includes the effect of heat transfer across the film hole and the plate.

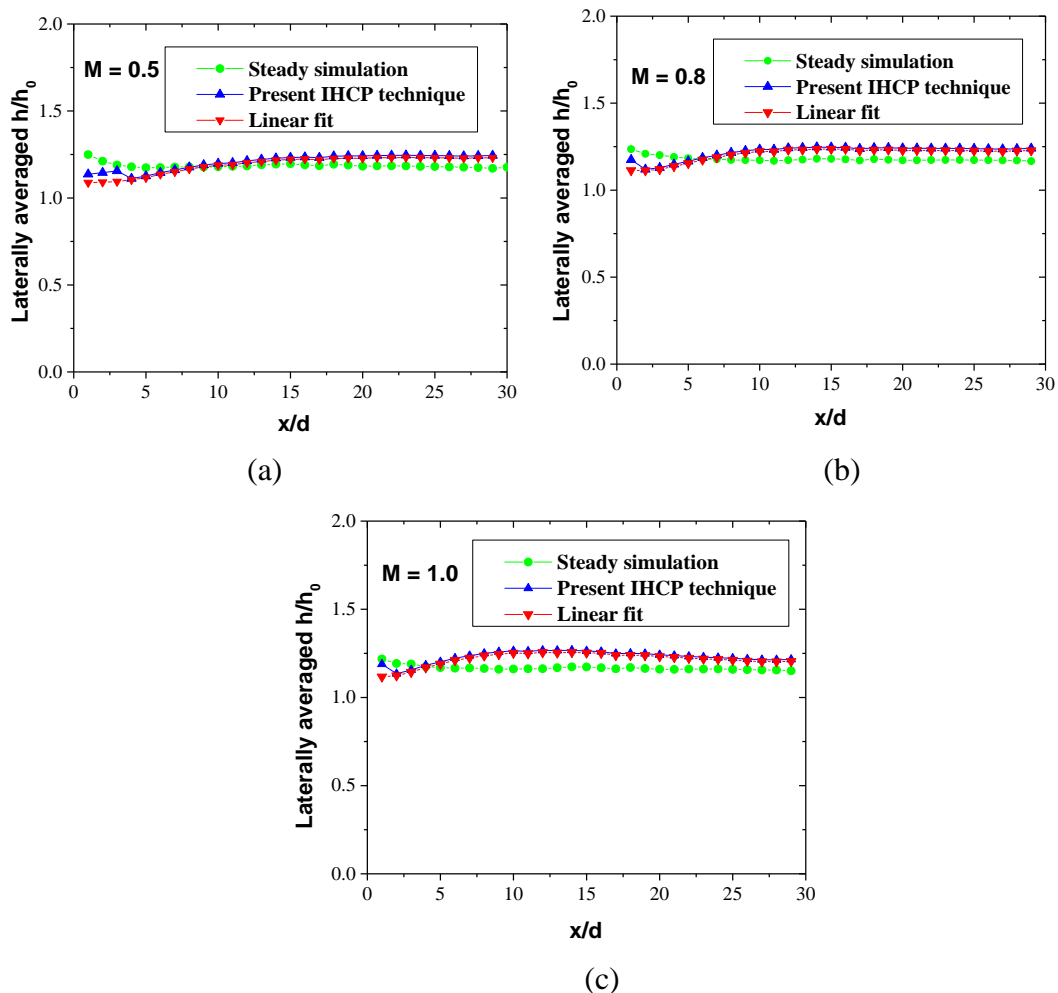


Figure 6.14. Comparison of normalized laterally averaged heat transfer coefficient obtained using different techniques for (a) $M = 0.5$, (b) $M = 0.8$ and (c) $M = 1.0$.

6.6 CLOSURE

The present chapter demonstrated a novel approach to simultaneously estimating the thermal boundary parameters of film cooling based on an inverse heat conduction technique. The solution methodology adopted in the present work employs an optimization technique to evaluate unknown film cooling parameters such as effectiveness and heat transfer coefficient appearing in the analytical solution of transient one-dimensional semi-infinite model. The transient wall temperature data at the film cooling surface is the only input required for this method and is generated through a three-dimensional numerical simulation for a cylindrical hole film cooling arrangement. The estimated values from the present IHCP method showed good agreement having a slight deviation of around 7% for the effectiveness and 4% for the heat transfer coefficient. The estimated h values from the present IHCP solution were underpredicted by about 6% for x/d less than 5, where the effect of coolant flow through the film hole prevails. Overall, this method has the potential to replace the existing steady state technique while offering more realistic solution in evaluating film cooling parameters.

Equation Chapter (Next) Section 1

CHAPTER 7

SUMMARY AND CONCLUSIONS

The present thesis investigated a new film cooling hole concept to enhance the existing cooling capability of a cylindrical hole using RANS based numerical simulations. The existence of a swirl inside the turbine blade components and its effect on film cooling performance was noticed. Hence, the effect of coolant swirl on film cooling characteristics was examined in the present work. The swirl generation method employed here attempted to insert a twisted tape inside the cylindrical film hole. Coolant passing through the hole with a twisted tape insert experiences an additional angular velocity and exits with a certain amount of swirl. Twisted tape allows a convenient way to achieve desired swirl intensity at the hole exit just by changing its pitch.

Initially, a cylindrical hole flat plate film cooling model was numerically simulated and the effectiveness values were validated with experimental results from previous studies. Later, simulations were carried out for three swirl numbers of 0.0289, 0.116 and 0.168 at blowing ratios of 0.5, 1.0, 1.5 and 2.0 and compared the results with the base case of a circular hole having zero swirl. Upon observing its usefulness, the swirl number was studied as a parameter by increasing it from 0.2 to 0.7.

In the next step, the effect of the coolant swirl was further analyzed by varying additional parameters, such as the injection angle of the coolant hole and the length-to-diameter ratio of the film hole. This particular parametric study was conducted at a blowing ratio of 1.0. For all the cases, the film cooling performance was investigated in terms of effectiveness, heat transfer coefficient and reduction in heat flux ratio.

The combined effect of swirl, injection angle and hole length to diameter ratio is examined to obtain an optimum value of these three geometric variables. This was achieved with the help of a surrogate model known as Radial Basis Function Neural Network. High fidelity CFD solutions are used to train the network, which resulted in a model representing the interconnection between inputs S , α and L/d with spatially

averaged η as output. An evolution-based global search optimization method known as the Genetic algorithm is used to find the optimum geometric configuration.

The last part of the thesis has discussed a simple data reduction approach for the simultaneous estimation of film cooling effectiveness and heat transfer coefficient. This technique is based on the solution of inverse heat conduction approach in which the transient wall temperature data is utilized to obtain film cooling thermal boundary parameters. The inverse heat transfer solution iteratively optimizes the unknown parameters appearing in the transient one-dimensional semi-infinite solution while minimizing the least squared error.

It can be concluded from the preset work that the film cooling with a twisted tape insert is able to enhance the cooling performance by up to 250% for a blowing ratio of 1, at $S = 0.168$. Even though an improvement in $\bar{\eta}$ of around 380% is observed for $M = 2.0$ at $S = 0.168$, a higher heat transfer rate limits the applicability of swirl at high blowing ratios. Analyzing the flow structure has demonstrated that the induced swirl mainly creates an asymmetry in the flow resulting in a better lateral spreading of the coolant. It is also noted that the jet penetration height is reduced by around 48% due to the influence of swirl. The twisted tape thickness does not appear to affect the coolant distribution drastically. The discharge coefficient for the case of twisted tape insert is obtained to be lower than a simple cylindrical hole film cooling indicating the requirement of additional pumping power.

However, the relation between swirl number and effectiveness is not always proportional. Instead, effectiveness varies nonlinearly with swirl number and blowing ratios. At low blowing ratios of $M < 1$, a highest $\bar{\eta}$ is observed at $S \approx 0.4$ while, for $M > 1$, it occurred at $S = 0.6$ along the downstream. Meanwhile, HTC was affected mildly with swirl number at low blowing ratios but had a considerable effect when M increased beyond 1. Hence the net effect in terms of NHFR was found to improve significantly at high blowing ratios when $S > 0.6$. Effectiveness between $S = 0.6$ and 0.7 shows completely different behavior from one another. Coolant jet separation disappears at $S = 0.7$, but a maximum coolant concentration is utilized immediately downstream of injection. The swirl mainly affected the CRVP by changing its symmetrical structure into asymmetric. However, this feature also depends on the

blowing ratio. The swirl effect becomes noticeable only when it overcomes a critical blowing ratio. With the increase in blowing ratio, an increase in swirl keeps reducing the coolant separation length and at a certain point, complete jet attachment occurs. With an increase in injection angle, a non-swirl case deteriorates the cooling effect, while an opposite behavior is observed at a swirl number of 0.7. The effect of hole length on swirled film cooling is observed to be minimal for $L/d > 8$.

The surrogate model based geometric optimization resulted in an optimum geometry having S , α and L/d of 0.32, 19.3° and 4, respectively, for $M = 1.0$. There is more than 110% improvement in effectiveness from the optimized geometry than the reference case of $S = 0.168$, $\alpha = 30^\circ$ and $L/d = 8$.

The transient film cooling analysis using IHCP method was found promising in estimating the effectiveness and the heat transfer coefficient. The estimated quantities were deviated slightly with an average error of up to 7% and 4% when compared with steady-state results of η and h respectively. The underprediction in h values occurred majorly for x/d less than 5 which is likely to occur due to heat transfer through film hole prior to exit. A significant advantage of this technique is that only up to 100 seconds of transient temperature data is sufficient to evaluate both η and h using a single test. A major limitation of the current technique is accurately calculating the sensitivity coefficients. Also, it can be concluded from the sensitivity analysis that a higher sampling rate while measuring the transient temperature data would reduce the estimation uncertainty. Overall, it can be ascertained from the present work that the IHCP technique can be successfully implemented to simultaneously estimate the effectiveness and heat transfer coefficient for transient film cooling analysis.

7.1 Contribution of the present work

In this work a way of controlling the coolant swirl is presented to enhance the existing capability of cylindrical hole film cooling performance. A wide range of parameters variation is considered to explore the possibility of improving the heat transfer characteristics. Hence, this study can be used as a ground work to implement and study the swirl effects on film cooling over a turbine blade.

The study also presented a method which can be used to optimize the configuration of film cooling geometrical parameters for any novel shapes of film cooling holes. Since an optimized variable combination is already found in the present study, one can implement this configuration directly for experimental evaluation, subjected to the validation of the swirled film cooling performance.

The work presented in the last part of the thesis based on transient analysis, can be very much helpful for the researchers to evaluate the unknown boundary parameters of film cooling using a single set of experiment. It can avoid the necessity of running wind tunnel experiments for longer duration to obtain steady state results and hence reduce the experimental uncertainty.

7.2 Scope for future work

Though the present work emphasizes having a twisted tape insert inside a film cooling hole, the foremost requirement is to verify the present findings with the help of experiments. The manufacturability is another challenge with the present design. Effects of other film cooling parameters, such as curvature effects, pressure gradients, free stream turbulence intensity, and surface roughness, need to be explored further. The optimization study was conducted for a single blowing ratio in this work. Hence, the study needs further evaluation for other blowing ratio cases. Also, the optimum geometry obtained in the present work may have to be revised when other parameters, such as curvature or rotational effects, are involved. Additionally, the twisted tape inserts can be used in conjunction with other hole shapes to obtain the benefits of both configurations.

The proposed IHCP method needs further improvement in terms of the forward solution. The one-dimensional semi-infinite solution is rather approximate and might fail when applied to actual turbine blade materials. A three-dimensional heat conduction solution might yield more realistic results at the expense of increased mathematical complexity.

REFERENCES

Acharya, S., Tyagi, M., and Hoda, A. (2001). "Flow and heat transfer predictions for film cooling." *Ann. Y. Acad. Sci.*, 934, 110–125.

Ammari, H. D., Hay, N., and Lampard, D. (1989). "The effect of density ratio on the heat transfer coefficient from a film cooled flat plate." *Proc. ASME Turbo Expo*, 4(July 1990).

Andreopoulos, J., and Rodi, W. (1984). "Experimental investigation of jets in a crossflow." *J. Fluid Mech.*, 138, 93–127.

Andrews, G. E., Alikhanizadeh, M., Tehrani, F. B., Hussain, C. I., and Azari, M. S. K. (1988). "Small Diameter Film Cooling Holes: The Influence of Hole Size and Pitch." *Int. J. Turbo Jet Engines*, 5(1–4), 61–72.

ANSYS Inc. (2014). *ANSYS FLUENT Theory Guide*. Cononsburg, PA, USA: ANSYS FLUENT 16.0.0.

Azzi, A., and Jubran, B. A. (2007). "Numerical modelling of film cooling from converging slot-hole." *Heat Mass Transf.*, 43(4), 381–388.

Barlow, D. N., and Kim, Y. W. (1995). "Effect of surface roughness on local heat transfer and film cooling effectiveness." *Proc. ASME Turbo Expo*, 4.

Beck, J. V, and Arnold, K. J. (1977). *Parameter Estimation in Engineering and Science*. Wiley.

Beck, J. V, Blackwell, B., and Clair Jr, C. R. S. (1985). *Inverse heat conduction: Ill-posed problems*. James Beck.

Bergeles, G., Gosman, A. D., and Launder, B. E. (1975). "The near-field character of a jet discharged through a wall at 90 deg to a main stream." *ASME*, 373–378.

Bergeles, G., Gosman, A. D., and Launder, B. E. (1977). "Near-field character of a jet discharged through a wall at 30 deg to a mainstream." *AIAA J.*, 15(4), 499–504.

Blair, M. F. (1983). "Influence of free-stream turbulence on turbulent boundary layer heat transfer and mean profile development, part II—analysis of results." *J. Heat Transfer*, 105(1), 41–47.

Bohn, D., Ren, J., and Kusterer, K. (2003). “Conjugate heat transfer analysis for film cooling configurations with different hole geometries.” *Turbo Expo Power Land, Sea, Air*, 247–256.

Bons, J. P., MacArthur, C. D., and Rivir, R. B. (1996). “The effect of high freestream turbulence on film cooling effectiveness.” *ASME. J. Turbomach.*, 118(4).

Broadwell, J. E., and Breidenthal, R. E. (1984). “Structure and mixing of a transverse jet in incompressible flow.” *J. Fluid Mech.*, 148, 405–412.

Brown, A., and Saluja, C. L. (1979). “Film cooling from a single hole and a row of holes of variable pitch to diameter ratio.” *Int. J. Heat Mass Transf.*, 22(4), 525–534.

Bunker, R. S. (2002). “Film cooling effectiveness due to discrete holes within a transverse surface slot.” *Am. Soc. Mech. Eng. Int. Gas Turbine Institute, Turbo Expo IGTI*, 3 A, 129–138.

Bunker, R. S. (2005). “A review of shaped hole turbine film-cooling technology.” *J. Heat Transfer*, 127(4), 441–453.

Bunyajitradulya, A., and Sathapornnanon, S. (2005). “Sensitivity to tab disturbance of the mean flow structure of nonswirling jet and swirling jet in crossflow.” *Phys. Fluids*, 17(4), 1–10.

Burd, S. W., Kaszeta, R. W., and Simon, T. W. (1998). “Measurements in film cooling flows: Hole lid and turbulence intensity effects.” *J. Turbomach.*, 120(4), 791–798.

Chen, P. H., Ding, P. P., and Ai, D. (2001). “Improved data reduction method for transient liquid crystal thermography on film cooling measurements.” *Int. J. Heat Mass Transf.*, 44(7).

Cho, G., Tang, H., Owen, J. M., and Lock, G. D. (2016). “On the measurement and analysis of data from transient heat transfer experiments.” *Int. J. Heat Mass Transf.*, 98, 268–276.

Choi, D. W., Lee, K. D., and Kim, K. Y. (2013). “Analysis and optimization of double-jet film-cooling holes.” *J. Thermophys. Heat Transf.*, 27(2), 246–254.

Colaço, M. J., Orlande, H. R. B., and Dulikravich, G. S. (2006). “Inverse and optimization problems in heat transfer.” *J. Brazilian Soc. Mech. Sci. Eng.*, 28(1), 1–24.

Coletti, F., Benson, M. J., Ling, J., Elkins, C. J., and Eaton, J. K. (2013). "Turbulent transport in an inclined jet in crossflow." *Int. J. Heat Fluid Flow*, 43, 149–160.

Crabb, D., Durao, D. F. G., and Whitelaw, J. H. (1980). "Round Jet Normal To a Cross-Flow." *Am. Soc. Mech. Eng.*, 103(80-WA/FE-10).

Crawford, M. E., Kays, W. M., and Moffat, R. J. (1980a). "Full-coverage film cooling: Part I: Comparison of heat transfer data for three injection angles." *J. Eng. Gas Turbines Power*, 102(4), 1000–1005.

Crawford, M. E., Kays, W. M., and Moffat, R. J. (1980b). "Full-Coverage Film Cooling - 2. Heat Transfer Data and Numerical Simulation." *Am. Soc. Mech. Eng.*, 102(80-GT-44), 1006–1012.

Dai, C., Jia, L., Zhang, J., Shu, Z., and Mi, J. (2016). "On the flow structure of an inclined jet in crossflow at low velocity ratios." *Int. J. Heat Fluid Flow*, 58, 11–18.

Demuren, A. O., Rodi, W., and Schönung, B. (1985). "Systematic study of film cooling with a three-dimensional calculation procedure." *Proc. ASME Turbo Expo*, 3.

Denev, J. A., Fröhlich, J., and Bockhorn, H. (2005). "Structure and mixing of a swirling transverse jet into a crossflow." *Fourth Int. Symp. Turbul. Shear Flow Phenom.*, Begel House Inc., 1255–1260.

Denev, J. A., Fröhlich, J., and Bockhorn, H. (2009). "Large eddy simulation of a swirling transverse jet into a crossflow with investigation of scalar transport." *Phys. Fluids*, 21(1), 1–21.

Deveci, K., Maral, H., Senel, C. B., Alpman, E., Kavurmacioglu, L., and Camci, C. (2018). "Aerothermal optimization of squealer geometry in axial flow turbines using genetic algorithm." *J. Therm. Eng.*, 4(3), 1896–1911.

Dhungel, A., Lu, Y., Phillips, W., Ekkad, S. V., and Heidmann, J. (2009). "Film cooling from a row of holes supplemented with antivortex holes." *J. Turbomach.*, 131(2), 1–10.

Drost, U., Bölcs, A., and Hoffs, A. (1997). "Utilization of the transient liquid crystal technique for film cooling effectiveness and heat transfer investigations on a flat plate and a turbine airfoil." *ASME 1997 Int. Gas Turbine Aeroengine Congr. Exhib.*, V003T09A006.

Duda, P., and Konieczny, M. (2022). “An Iterative Algorithm for the Estimation of Thermal Boundary Conditions Varying in Both Time and Space.” *Energies*, 15(7), 2686.

Ekkad, S., and Han, J. C. (2015). “A review of hole geometry and coolant density effect on film cooling.” *Front. Heat Mass Transf.*, 6(1).

Ekkad, S. V., and Han, J. C. (2000). “A transient liquid crystal thermography technique for gas turbine heat transfer measurements.” *Meas. Sci. Technol.*, 11(7), 957–968.

Ekkad, S. V., Zapata, D., and Han, J. C. (1995a). “Film effectiveness over a flat surface with air and CO₂ injection through compound angle holes using a transient liquid crystal image method.” *Proc. ASME Turbo Expo*, 4(July 1997), 580–586.

Ekkad, S. V., Zapata, D., and Han, J. C. (1995b). “Film effectiveness over a flat surface with air and CO₂ injection through compound angle holes using a transient liquid crystal image method.” *Proc. ASME Turbo Expo*, 4(July 1997).

Ekkad, S. V., Ou, S., and Rivir, R. B. (2004). “A transient infrared thermography method for simultaneous film cooling effectiveness and heat transfer coefficient measurements from a single test.” *J. Turbomach.*, 126(4), 597–603.

Ekkad, S. V., and Singh, P. (2021). “Liquid Crystal Thermography in Gas Turbine Heat Transfer: A Review on Measurement Techniques and Recent Investigations.” *Crystals*, 11(11), 1332.

Ekkad, S. V., Zapata, D., and Han, J. C. (1997). “Heat transfer coefficient over a flat surface with air and CO₂ injection through compound angle holes using a transient liquid crystal image method.” *J. Turbomach.*, 119, 580–586.

Eriksen, V. L., and Goldstein, R. J. (1974). “Heat transfer and film cooling following injection through inclined circular tubes.” *J. Heat Transf.*, 96(2), 239–245.

Ferguson, J. D., Walters, D. K., and Lylek, J. H. (1998). “Performance of turbulence models and near-wall treatments in discrete jet film cooling simulations.” *Proc. ASME Turbo Expo*, 4, 1–12.

Fric, T., and Roshko, A. (1994). “Vortical structure in the wake of a transverse jet.” *J. Fluid Mech.*, 279, 1–47.

Galeana, D., and Beyene, A. (2021). “Gas turbine blade heat transfer and

internal swirl cooling flow experimental study using liquid crystals and three-dimensional stereo-particle imaging velocimetry.” *J. Energy Resour. Technol. Trans. ASME*, 143(10), 1–9.

Ghorab, M. G. (2011). “Film cooling effectiveness and net heat flux reduction of advanced cooling schemes using thermochromic liquid crystal.” *Appl. Therm. Eng.*, 31(1), 77–92.

Glezer, B., Moon, H. K., Kerrebrock, J., Bons, J., and Guenette, G. (1998). “Heat transfer in a rotating radial channel with swirling internal flow.” *Proc. ASME Turbo Expo*, 4, 1–7.

Goldstein, R. J. (1971). “Film Cooling.” *Adv. Heat Transf.*, 7(C), 321–379.

Goldstein, R. J., Eckert, E. R. G., and Burggraf, F. (1974). “Effects of hole geometry and density on three-dimensional film cooling.” *Int. J. Heat Mass Transf.*, 17(5), 595–607.

Goldstein, R. J., Eckert, E. R. G., Chiang, H. D., and Elovic, E. (1985). “Effect of surface roughness on film cooling performance.” *J. Eng. Gas Turbines Power*, 107(1), 111–116.

Goldstein, R. J., Eckert, E. R. G., and Ramsey, J. W. (1968a). “Film cooling with injection through holes: adiabatic wall temperatures downstream of a circular hole.” *J. Eng. Power*, 90(4), 384–393.

Goldstein, R. J., Eckert, E. R. G., and Ramsey, J. W. (1968b). “Film cooling with injection through holes: Adiabatic wall temperatures downstream of a circular hole.” *J. Eng. Gas Turbines Power*, 90(4), 384–393.

Gritsch, M., Schulz, A., and Wittig, S. (2000). “Film-cooling holes with expanded exits: Near-hole heat transfer coefficients.” *Int. J. Heat Fluid Flow*, 21(2), 146–155.

Guo, X., Schröder, W., and Meinke, M. (2006). “Large-eddy simulations of film cooling flows.” *Comput. Fluids*, 35(6), 587–606.

Gupta, A. K., Lilley, D. G., and Syred, N. (1984). *Swirl Flows*. Abacus Press.

Hahn, D. W., and Özisik, M. N. (2012). *Heat Conduction*. John Wiley & Sons.

Han, J.-C., Dutta, S., and Ekkad, S. (2012). *Gas Turbine Heat Transfer and Cooling Technology. 2nd Ed. CRC Press*, 2nd edition, CRC Press.

Han, J. C., Park, J. S., and Lei, C. K. (1984). “Heat Transfer and Pressure

Drop in Blade Cooling Channels With Turbulence Promoters.” *NASA Contract Reports*.

Harrison, K. L., and Bogard, D. G. (2007). “CFD predictions of film cooling adiabatic effectiveness for cylindrical holes embedded in narrow and wide transverse trenches.” *Proc. ASME Turbo Expo*, 4 PART B, 811–820.

Harrison, K. L., and Bogard, D. G. (2008a). “Comparison of RANS turbulence models for prediction of film cooling performance.” *Proc. ASME Turbo Expo*, 4(PART B), 1187–1196.

Harrison, K. L., and Bogard, D. G. (2008b). “Comparison of {RANS} turbulence models for prediction of film cooling performance.” *ASME Turbo Expo 2008 Power Land, Sea, Air*, 1187–1196.

Haven, B. A., and Kurosaka, M. (1996). “Improved jet coverage through vortex cancellation.” *AIAA J.*, 34(11), 2443–2444.

Haven, B. A., Yamagata, D. K., Kurosaka, M., Yamawaki, S., and Maya, T. (1997). “Anti-Kidney Pair of Vortices in Shaped Holes and Their Influence on Film Cooling Effectiveness.” *ASME Int. Gas Turbine Aeroengine Congr. Exhib.*, V003T09A007-V003T09A007.

Hay, N., Lampard, D., and Saluja, C. L. (1985). “Effects of cooling films on the heat transfer coefficient on a flat plate with zero mainstream pressure gradient.” *J. Eng. Gas Turbines Power*, 107(1), 105–110.

Hedlund, C. R., Ligrani, P. M., Moon, H. K., and Glezer, B. (1999). “Heat transfer and flow phenomena in a swirl chamber simulating turbine blade internal cooling.” *Proc. ASME Turbo Expo*, 121(4), 804–8013.

Heidmann, J. D., and Ekkad, S. (2008). “A novel antivortex turbine film-cooling hole concept.” *J. Turbomach.*, 130(3), 1–9.

Hoda, A., and Acharya, S. (1999). “Predictions of a film coolant jet in crossflow with different turbulence models.” *Proc. ASME Turbo Expo*, 3.

Incropera, F. P., DeWitt, D. P., Bergman, T. L., and Adrienne, L. S. (2006). *Fundamentals of Heat and Mass Transfer*. New York: John Wiley & Sons.

Jabbari, M. Y., and Goldstein, R. J. (1977). “Adiabatic Wall Temperature and Heat Transfer Downstream of Injection Through Two Rows of Holes.” *Am. Soc. Mech. Eng.*, 100(77-GT-50), 303–307.

Jiang, Y., Yue, G., Dong, P., Gao, J., and Zheng, Q. (2017). "Investigation on film cooling with swirling coolant flow by optimizing the inflow chamber." *Int. Commun. Heat Mass Transf.*, 88, 99–107.

Junkhan, G. H., and Serovy, G. K. (1967). "Effects of free-stream turbulence and pressure gradient on flat-plate boundary-layer velocity profiles and on heat transfer." *J. Heat Transfer*, 89(2), 169–175.

Kadam, A. R., Hindasageri, V., and Kumar, G. N. (2020). "Inverse estimation of heat transfer coefficient and reference temperature in jet impingement." *J. Heat Transfer*, 142(9).

Kadotani, K., and Goldstein, R. J. (1979). "Effect of mainstream variables on jets issuing from a row of inclined round holes." *J. Eng. Power*, 101(2), 298–304.

Kalghatgi, P., and Acharya, S. (2015). "Improved film cooling effectiveness with a round film cooling hole embedded in a contoured crater." *J. Turbomach.*, 137(10), 1–10.

Kamotani, Y., and Greber, I. (1972). "Experiments on a Turbulent Jet in a Cross Flow." *AIAA J.*, 10(11), 1425–1429.

Kang, M. B., Kohli, A., and Thole, K. A. (1999). "Heat transfer and flowfield measurements in the leading edge region of a stator vane endwall." *J. Turbomach.*, 121(3), 558–568.

Kapadia, S., Roy, S., and Heidmann, J. (2003). "Detached eddy simulation of turbine blade cooling." *36th AIAA Thermophys. Conf.*

Kavsoglu, M. S., and Schetz, J. A. (1989). "Effects of swirl and high turbulence on a jet in a crossflow." *J. Aircr.*, 26(6), 539–546.

Kercher, D. M. (1998). "A Film-Cooling CFD Bibliography: 1971–1996." *Int. J. Rotating Mach.*, 4(1), 61–72.

Khalatov, A. A., Panchenko, N. A., and Severin, S. D. (2017). "Numerical simulation of a flat plate film cooling with a coolant supply into different shape indentations." *Thermophys. Aeromechanics*, 24(5), 731–737.

Ko, S.-Y., Yao, Y.-Q., Xia, B., and Tsou, F.-K. (1986). "Discrete-hole film cooling characteristics over concave and convex surfaces." *Heat Transf. 1986; Proc. Eighth Int. Conf.*, 1297–1301.

Kumar, S. S., Hindasageri, V., and Prabhu, S. V. (2017). "Local heat transfer

distribution on a flat plate impinged by a swirling jet generated by a twisted tape.” *Int. J. Therm. Sci.*, 111, 351–368.

Lakshminarayana, B. (1995). *Fluid dynamics and heat transfer of turbomachinery*. John Wiley & Sons.

LeBlanc, C., Narzary, D. P., and Ekkad, S. (2013). “Film-cooling performance of antivortex hole on a flat plate.” *J. Turbomach.*, 135(3), 1–11.

Lee, K.-D., Husain, A., and Kim, K.-Y. (2010). “Multi-objective Optimization of a Laidback Fan Shaped Film-Cooling Hole Using Evolutionary Algorithm.” *Int. J. Fluid Mach. Syst.*, 3(2), 150–159.

Lee, K. D., and Kim, K. Y. (2009). “Optimization of a cylindrical film cooling hole using surrogate modeling.” *Numer. Heat Transf. Part A Appl.*, 55(4), 362–380.

Lee, K. D., and Kim, K. Y. (2010). “Shape optimization of a fan-shaped hole to enhance film-cooling effectiveness.” *Int. J. Heat Mass Transf.*, 53(15–16), 2996–3005.

Lee, K. D., and Kim, K. Y. (2011). “Surrogate based optimization of a laidback fan-shaped hole for film-cooling.” *Int. J. Heat Fluid Flow*, 32(1), 226–238.

Lee, S., Hwang, W., and Yee, K. (2018). “Robust design optimization of a turbine blade film cooling hole affected by roughness and blockage.” *Int. J. Therm. Sci.*, 133(May), 216–229.

Lee, S. W., Lee, J. S., and Ro, S. T. (1994). “Experimental Study on the Flow Characteristics of Streamwise Inclined Jets in Crossflow on Flat Plate.” *J. Turbomach.*, 116(1), 97–105.

Levenberg, K. (1944). “A method for the solution of certain non-linear problems in least squares.” *Q. Appl. Math.*, 2(2), 164–168.

Leylek, J. H., and Zerkle, R. D. (1993). “Discrete-jet film cooling: A comparison of computational results with experiments.” *ASME 1993 Int. Gas Turbine Aeroengine Congr. Expo. GT 1993*, 3A.

Li, G. chao, Yang, P., Zhang, W., Wu, Z., and Kou, Z. hai. (2019). “Enhanced film cooling performance of a row of cylindrical holes embedded in the saw tooth slot.” *Int. J. Heat Mass Transf.*, 132, 1137–1151.

Li, H. M., Ghaly, W., and Hassan, I. (2016). “The formation of counter-rotating vortex pair and the nature of liftoff-reattachment in film-cooling flow.”

Fluids, 1(4), 1–21.

Li, W., Li, X., Ren, J., and Jiang, H. (2018). “Length to diameter ratio effect on heat transfer performance of simple and compound angle holes in thin-wall airfoil cooling.” *Int. J. Heat Mass Transf.*, 127, 867–879.

Liu, C. L., Zhu, H. R., Bai, J. T., and Xu, D. C. (2010). “Film cooling performance of converging slot-hole rows on a gas turbine blade.” *Int. J. Heat Mass Transf.*, 53(23–24), 5232–5241.

Liu, Z., Li, J., and Feng, Z. (2015). “Numerical study of swirl cooling in a turbine blade leading-edge model.” *J. Thermophys. Heat Transf.*, 29(1), 166–178.

Lu, Y., Dhungel, A., Ekkad, S. V., and Bunker, R. S. (2009). “Effect of trench width and depth on film cooling from cylindrical holes embedded in trenches.” *J. Turbomach.*, 131(1), 1–13.

Luo, J., Liu, C., and Zhu, H. (2014). “Numerical investigation of film cooling performance with different internal flow structures.” *Turbo Expo Power Land, Sea, Air*, American Society of Mechanical Engineers, V05BT13A008.

Lutum, E., and Johnson, B. V. (1998). “Influence of the hole length-to-diameter ratio on film cooling with cylindrical holes.” *Proc. ASME Turbo Expo*, 121(2), 209–216.

Mahesh, K. (2013). “The interaction of jets with crossflow.” *Annu. Rev. Fluid Mech.*, 45, 379–407.

Makki, Y. H., and Jakubowski, G. S. (1986). “Experimental Study of Film Cooling From Diffused Trapezoidal Shaped Holes.” *AIAA Pap.*

Marek, C. J., Tacina, R. R. (1975). “Effect of free-stream turbulence on film cooling.” (No. NASA-TN-D-7958).

Marquardt, D. W. (1963). “An Algorithm for Least-Squares Estimation of Nonlinear Parameters.” *J. Soc. Ind. Appl. Math.*, 11(2), 431–441.

Mayle, R. E., and Camarata, F. J. (1974). “Multihole Cooling Film Effectiveness and Heat Transfer.” *Am. Soc. Mech. Eng.*, (74-HT-9), 534–538.

Mazzei, L., Andreini, A., and Facchini, B. (2017). “Assessment of modelling strategies for film cooling.” *Int. J. Numer. Methods Heat Fluid Flow*, 27(5), 1118–1127.

McClintic, J. W., Fox, D. W., Jones, F. B., Bogard, D. G., Dyson, T. E., and

Webster, Z. D. (2019). “Flow physics of diffused-exit film cooling holes fed by internal crossflow.” *J. Turbomach.*, 141(3), 1–9.

Metzger, D. E., Takeuchi, D. I., and Keunstler, P. A. (1973). “Effectiveness and Heat Transfer With Full-Coverage Film Cooling.” *ASME Pap*, (73-GT-18).

Miller, K. L., and Crawford, M. E. (1984). “Numerical simulation of single, double, and multiple row film cooling effectiveness and heat transfer.” *Turbo Expo Power Land, Sea, Air*, American Society of Mechanical Engineers, V004T09A008.

Moeini, A., and Rajabi Zargarabadi, M. (2018). “Genetic algorithm optimization of film cooling effectiveness over a rotating blade.” *Int. J. Therm. Sci.*, 125(December 2017), 248–255.

Montazeri, M., Mohammadiun, H., Mohammadiun, M., Dibae Bonab, M. H., and Vahedi, M. (2021). “Inverse analysis of the time-dependent heat flux in stagnation point flow of incompressible fluid impinging on a cylinder with uniform surface suction-blowing using Levenberg–Marquardt method.” *Inverse Probl. Sci. Eng.*, 29(9), 1219–1259.

Narzary, D. P., LeBlanc, C., and Ekkad, S. (2011). “Film-Cooling Performance of Anti-Vortex Hole on a Flat Plate.” *ASME/JSME Therm. Eng. Jt. Conf.*, T10077.

Nellis, G., and Klein, S. A. (2009). *Heat Transfer*. Cambridge University Press.

Niederhaus, C. E., Champagne, F. H., and Jacobs, J. W. (1997). “Scalar transport in a swirling transverse jet.” *AIAA J.*, 35(11), 1697–1704.

Oda, Y., Takeishi, K., and Shimizu, D. (2011). “Large Eddy Simulation of Film Cooling With Swirling Coolant Flow.” *ASME/JSME Therm. Eng. Jt. Conf.*, 38921, T10102.

Ou, S., and Rivir, R. B. (2001). “Leading edge film cooling heat transfer with high free stream turbulence using a transient liquid crystal image method.” *Int. J. Heat Fluid Flow*, 22(6), 614–623.

Ozisik, M. N. (2018). *Inverse Heat Transfer: Fundamentals and Applications*. Routledge.

Ozisik, M. N., Orlande, H. R. B., and Kassab, A. J. (2002). “Inverse heat transfer: fundamentals and applications.” *Appl. Mech. Rev.*, 55(1), B18–B19.

Park, S., Jung, E. Y., Kim, S. H., Sohn, H. S., and Cho, H. H. (2016). “Enhancement of film cooling effectiveness using backward injection holes.” *Int. J. Therm. Sci.*, 110, 314–324.

Pedersen, D. R., Eckert, E. R. G., and Goldstein, R. J. (1977). “Film cooling with large density differences between the mainstream and the secondary fluid measured by the heat-mass transfer analogy.” *J. Heat Transfer*, 99(4), 620–627.

Peet, Y. V., and Lele, S. K. (2008). “Near field of film cooling jet issued into a flat plate boundary layer: LES study.” *Proc. ASME Turbo Expo*, GT2008-504, 409–418.

Peterson, S. D., and Plesniak, M. W. (2002). “Short-hole jet-in-crossflow velocity field and its relationship to film-cooling performance.” *Exp. Fluids*, 33(6), 889–898.

Peterson, S. D., and Plesniak, M. W. (2004). “Evolution of jets emanating from short holes into crossflow.” *J. Fluid Mech.*, 503, 57–91.

Peterson, S. D., and Plesniak, M. W. (2007). “Flow structure and skin friction in the vicinity of a streamwise-angled injection hole fed by a short pipe.” *Exp. Fluids*, 43(4), 627–638.

Pietrzyk, J. R., Bogard, D. G., and Crawford, M. E. (1989a). “Effects of density ratio on the hydrodynamics of film cooling.” *Proc. ASME Turbo Expo*, 4.

Pietrzyk, J. R., Bogard, D. G., and Crawford, M. E. (1989b). “Hydrodynamic measurements of jets in crossflow for gas turbine film cooling applications.” *J. Turbomach.*, 111(2), 139–145.

Pujol, J. (2007). “The solution of nonlinear inverse problems and the Levenberg-Marquardt method.” *Geophysics*, 72(4), W1–W16.

Queipo, N. V., Haftka, R. T., Shyy, W., Goel, T., Vaidyanathan, R., and Kevin Tucker, P. (2005). “Surrogate-based analysis and optimization.” *Prog. Aerosp. Sci.*, 41(1), 1–28.

Sargison, J. E., Guo, S. M., Oldfield, M. L. G., Lock, G. D., and Rawlinson, A. J. (2002). “A converging slot-hole film-cooling geometry-Part 1: Low-speed flat-plate heat transfer and loss.” *J. Turbomach.*, 124(3), 453–460.

Sargison, J. E., Oldfield, M. L. G., Guo, S. M., Lock, G. D., and Rawlinson, A. J. (2005). “Flow visualisation of the external flow from a converging slot-hole

film-cooling geometry.” *Exp. Fluids*, 38(3), 304–318.

Sarkar, S., and Bose, T. K. (1995). “Comparison of different turbulence models for prediction of slot-film cooling: Flow and temperature field.” *Numer. Heat Transf. Part B Fundam.*, 28(2), 217–238.

Saumweber, C., and Schulz, A. (2012). “Effect of geometry variations on the cooling performance of fan-shaped cooling holes.” *J. Turbomach.*, 134(6), 1–16.

Schmidt, D. L., and Bogard, D. G. (1996). “Effects of free-stream turbulence and surface roughness on film cooling.” *Turbo Expo Power Land, Sea, Air*, American Society of Mechanical Engineers, V004T09A049.

Schmidt, D. L., Sen, B., and Bogard, D. G. (1994). “Film cooling with compound angle holes: Adiabatic effectiveness.” *Proc. ASME Turbo Expo*, 4.

Schmidt, D. L., Sen, B., and Bogard, D. G. (1996). “Effects of surface roughness on film cooling.” *ASME 1996 Int. Gas Turbine Aeroengine Congr. Exhib. GT 1996*, 4.

Schoeiri, M. T. (2017). “Gas turbine design, components and system design integration.” *Gas Turbine Des. Components Syst. Des. Integr.*, 1–510.

Schulz, S., Maier, S., and Bons, J. P. (2012). “An experimental investigation of an anti-vortex film cooling geometry under low and high turbulence conditions.” *Proc. ASME Turbo Expo*, 4(Parts A and B), 1581–1593.

Schwarz, S. G., Goldstein, R. J., and Eckert, E. R. G. (1991). “The influence of curvature on film cooling performance.” *J. Turbomach.*, 113(3), 472–478.

Sen, B., Schmidt, D. L., and Bogard, D. G. (1996). “Film cooling with compound angle holes: Heat transfer.” *J. Turbomach.*, 118(4), 800–806.

Sinha, A. K., Bogard, D. G., and Crawford, M. E. (1991). “Film-cooling effectiveness downstream of a single row of holes with variable density ratio.” *J. Turbomach.*, 113(3), 442–449.

Smith, S. H., and Mungal, M. G. (1998). “Mixing, structure and scaling of the jet in crossflow.” *J. Fluid Mech.*, 357, 83–122.

Tahmasbi, V., and Noori, S. (2020). “Application of Levenberg--Marquardt Method for Estimation of the Thermophysical Properties and Thermal Boundary Conditions of Decomposing Materials.” *Heat Transf. Eng.*, 41(5), 449–475.

Takeishi, K., Komiyama, M., Oda, Y., Egawa, Y., and Egawayuta, Y. (2013).

“Aerothermal Investigations on Mixing Flow Field of Film Cooling With Swirling Coolant Flow.” *J. Turbomach.*, 136(5), 1–9.

Takeishi, K., Oda, Y., Egawa, Y., and Kitamura, T. (2010). “Film cooling with swirling coolant flow.” *WIT Trans. Eng. Sci.*, 68, 189–200.

Takeishi, K., Oda, Y., and Kondo, S. (2014). “Film Cooling With Swirling Coolant Flow on a Flat Plate and the Endwall of High-Loaded First Nozzle.” *Proc. ASME Turbo Expo 2014 Turbine Tech. Conf. Expo.*, Düsseldorf, Germany: ASME, 1–13.

Terzis, A., Kazakos, C., Zachos, P., Kalfas, A., and Ott, P. (2011). “Swirl jet and crossflow interaction at low velocity ratios and incompressible flows.” *9th Eur. Conf. Turbomach. Fluid Dyn. Thermodyn.*, 133–144.

Thole, K., Gritsch, M., Schulz, A., and Wittig, S. (1996). “Flowfield measurements for film-cooling holes with expanded exits.” *ASME 1996 Int. Gas Turbine Aeroengine Congr. Exhib. GT 1996*, 4, 1–10.

Thole, K., Gritsch, M., Schulz, A., and Wittig, S. (1998). “Flowfield measurements for film-cooling holes with expanded exits.” *J. Turbomach.*, 120(2), 327–336.

Tholel, K. A., Gritsch, M., Schulz, A., and Wittig, S. (1997). “Effect of a crossflow at the entrance to a film-cooling hole.” *J. Fluids Eng. Trans. ASME*, 119(3), 533–540.

Vedula, R. J., and Metzger, D. E. (1991). “A method for the simultaneous determination of local effectiveness and heat transfer distributions in three-temperature convection situations.” *36th ASME, Int. Gas Turbine Aeroengine Congr. Expo.*

Vogel, G., Graf, A., and Weigand, B. (2002). “Film cooling: A comparative study of different heater-foil configurations for liquid crystals experiments.” *Am. Soc. Mech. Eng. Int. Gas Turbine Institute, Turbo Expo IGTI*, 3 B(June), 1043–1050.

Vogel, G., Grat, A. B. A., Wolfersdorf, J. Von, and Weigand, B. (2003). “A novel transient heater-foil technique for liquid crystal experiments on film-cooled surfaces.” *J. Turbomach.*, 125(3), 529–537.

Walters, D. K., and Leylek, J. H. (1996). “A systematic computational methodology applied to a three-dimensional film-cooling flowfield.” *ASME 1996 Int.*

Gas Turbine Aeroengine Congr. Exhib., V004T09A040.

Walters, D. K., and Leylek, J. H. (1997). "A Detailed Analysis of Film-Cooling Physics: Part I—Streamwise Injection With Cylindrical Holes ." *J. Turbomach.*, 122(1), 102–112.

Wang, C., Zhang, J., and Zhou, J. (2016). "Optimization of a fan-shaped hole to improve film cooling performance by RBF neural network and genetic algorithm." *Aerosp. Sci. Technol.*, 58, 18–25.

Wang, J., Liu, C., Zhao, Z., Baleta, J., and Sundén, B. (2020). "Effect and optimization of backward hole parameters on film cooling performance by Taguchi method." *Energy Convers. Manag.*, 214, 112809.

Waye, S. K., and Bogard, D. G. (2007). "High-resolution film cooling effectiveness measurements of axial holes embedded in a transverse trench with various trench configurations." *J. Turbomach.*, 129(2), 294–302.

Xue, S., Roy, A., Ng, W. F., and Ekkad, S. V. (2015). "A novel transient technique to determine recovery temperature, heat transfer coefficient, and film cooling effectiveness simultaneously in a transonic turbine cascade." *J. Therm. Sci. Eng. Appl.*, 7(1).

Yang, W., Pu, J., and Wang, J. (2016). "The combined effects of an upstream ramp and swirling coolant flow on film cooling characteristics." *J. Turbomach.*, 138(11), 1–10.

Yang, W., Shi, X., and Zhang, J. (2017). "Experimental investigation on film cooling characteristics of ellipse-shaped tab." *Exp. Therm. Fluid Sci.*, 81, 277–290.

Yang, X., Liu, Z., Liu, Z., and Feng, Z. (2015). "Numerical analysis on effects of coolant swirling motion on film cooling performance." *Int. J. Heat Mass Transf.*, 90, 1082–1089.

Yao, Y., and Zhang, J. (2011). "Investigation on film cooling characteristics from a row of converging slot-holes on flat plate." *Sci. China Technol. Sci.*, 54(7), 1793–1800.

Yao, Y., Zhang, J., and Yang, Y. (2013). "Numerical study on film cooling mechanism and characteristics of cylindrical holes with branched jet injections." *Propuls. Power Res.*, 2(1), 30–37.

Yingjaroen, T., Pimpin, A., and Bunyajitradulya, A. (2006). "Evolution of

Mixing Regions in Jet and Swirling Jet in Crossflow: An Experimental Study.” *20th Conf. Mech. Eng. Netw. Thail.*, (October), 1–6.

Yoshida, T., and Goldstein, R. J. (1984). “On the nature of jets issuing from a row of holes into a low Reynolds number mainstream flow.” *J. Eng. Gas Turbines Power*, 106(3), 612–618.

Yu, Y., Yen, C. H., Shih, T. I. P., Chyu, M. K., and Gogineni, S. (2002). “Film cooling effectiveness and heat transfer coefficient distributions around diffusion shaped holes.” *J. Heat Transfer*, 124(5), 820–827.

Yuen, C. H. N., and Martinez-Botas, R. F. (2003). “Film cooling characteristics of a single round hole at various streamwise angles in a crossflow: Part I effectiveness.” *Int. J. Heat Mass Transf.*, 46(2), 221–235.

Yuen, C. H. N., and Martinez-Botas, R. F. (2005). “Film cooling characteristics of rows of round holes at various streamwise angles in a crossflow: Part II. Heat transfer coefficients.” *Int. J. Heat Mass Transf.*, 48(23–24), 5017–5035.

Zamiri, A., You, S. J., and Chung, J. T. (2020). “Large Eddy Simulation in the Optimization of Laidback Fan-Shaped Hole Geometry to Enhance Film-Cooling Performance.” *Int. J. Heat Mass Transf.*, 158, 120014.

Zhang, H., Li, Y., Chen, Z., Su, X., and Yuan, X. (2019). “Multi-fidelity model based optimization of shaped film cooling hole and experimental validation.” *Int. J. Heat Mass Transf.*, 132, 118–129.

Zhang, X. Z., and Hassan, I. (2006). “Film cooling effectiveness of an advanced-louver cooling scheme for gas turbines.” *J. Thermophys. Heat Transf.*, 20(4), 754–763.

Zhou, W., and Hu, H. (2016). “Improvements of film cooling effectiveness by using Barchan dune shaped ramps.” *Int. J. Heat Mass Transf.*, 103, 443–456.

Zhu, R., Terrence, S., Li, S., and Xie, G. (2022a). “Film cooling performance and flow structure of single-hole and double-holes with swirling jet.” *Chinese J. Aeronaut.*, 35(3), 201–213.

Zhu, R., Xie, G., Li, S., and Lei, J. (2022b). “Experimental investigation and numerical analysis on effects of swirling coolant on flow characteristics and film cooling performance.” *Int. Commun. Heat Mass Transf.*, 135, 106112.

Zuniga, H. A., and Kapat, J. S. (2009). “Effect of increasing pitch-to-diameter

ratio on the film cooling effectiveness of shaped and cylindrical holes embedded in trenches.” *Proc. ASME Turbo Expo 2009 Power Land, Sea, Air*, 3, 863–872.

BIODATA

NAME : VASHISTA G A

DATE OF BIRTH : 30 JULY 1988

ADDRESS : GEEJAGARU, E. J. MANE POST
SAGAR (TQ), SHIMOGA (DT)
KARNATAKA – 577401

QUALIFICATION: B. E. – Mechanical Engineering
(GM Institute of Technology, Davangere)
M. TECH. – Thermal Power Engineering
(Nitte Meenakshi Institute of Technology,
Bangalore)

Email address : v.ademane@gmail.com

Contact number : +91-9880743287

PUBLICATION DETAILS

1. Ademane, V., Kadoli, R., and Hindasageri, V. (2022). “Influence of twisted tape insert on the coolant flow characteristics in swirled film cooling.” *Therm. Sci.*, 26 (4 Part B), 3387–3398.
2. Ademane, V., Kadoli, R., and Hindasageri, V. (2023). “Simultaneous estimation of reference temperature and heat transfer coefficient in transient film cooling problems.” *J. Therm. Eng.*, 9(3), 702–717.
3. Ademane, V. G., Hindasageri, V., and Kadoli, R. (2019). “A Numerical Study on Heat Transfer Characteristics of Two-Dimensional Film Cooling BT - Numerical Heat Transfer and Fluid Flow.” D. Srinivasacharya and K. S. Reddy, eds., Singapore: Springer Singapore, 613–619.

List of Publications based on Ph.D. Research Work

Sl. No.	Title of the paper	Name of the Authors as it is in the paper	Name of the Journal/Conference/Symposium, Vol., No., Pages	Month, Year of Publication	Category *
1.	Influence of Twisted Tape Insert on the Coolant Flow Characteristics in Swirled Film Cooling	<u>Vashista Ademane,</u> Ravikiran Kadoli and Vijaykumar Hinasageri	Thermal Science, Vol. 26, No. 4B, pp. 3387-3398	2022	1
2.	Simultaneous Estimation of Reference Temperature and Heat Transfer Coefficient in Transient Film Cooling Problems	<u>Vashista Ademane,</u> Ravikiran Kadoli and Vijaykumar Hinasageri	Journal of Thermal Engineering, Vol. 9, No. 3, pp. 702–717,	May, 2023	1
3.	A Numerical Study on Heat Transfer Characteristics of Two-Dimensional Film Cooling	<u>Vashista G Ademane,</u> Vijaykumar Hinasageri and Ravikiran Kadoli	Numerical Heat Transfer and Fluid Flow at NIT Warangal	January 19-21, 2018	3
4.	Numerical Simulation Using Standard $k - \epsilon$ and RNG $k - \epsilon$ Turbulence Models for Film Cooling Studies	<u>Vashista Ademane,</u> Vijaykumar Hinasageri and Ravikiran Kadoli	Fluid Mechanics and Fluid Power at IIT Bombay	December 10-12, 2018	3

***Category:**

1: Journal paper, full paper reviewed

2: Journal paper, Abstract reviews

3: Conference/Symposium paper, full paper reviewed

4: Conference/Symposium paper, abstract reviewed

5: others (including papers in Workshops, NITK Research Bulletins, Short notes etc.)